Commented [ss1]:

Commented [AMD2R1]:

Paper 51

Structural Influence of Serine on ZnO Nanostructures

Shraddha Mahakal

Assistant Professor, Department of Physics,

Annasaheb Awate College, Manchar, Pune India

Abstract:

A simple representative bio-composite, in which serine integrated ZnO nanostructures has synthesized by chemical method. In this study, the impact of serine on ZnO nanomaterial has been investigated in terms of structural, morphological, optical and bacterial properties. The X-ray diffraction of these bio-composites with pristine ZnO has indicated the induced strain in the ZnO matrix. The details of the structural study revealed modification in morphology of bio-composite along with variation in interplanar distance.

The different properties of serine studies for different concentration in the surrounding climate of ZnO nanomaterial. It has been observed that serine has strong impression on ZnO as calculated strain increased from $1.11X10^{-3}$ to $3.28X10^{-3}$.The morphology changes from hexagonal disc to hexagonal cross-sectional tubes grown in a particular direction with enhancement in visible luminescence compared to pristine ZnO. The biocompatibility of serine incorporated ZnO was noticed to enhance compared to ZnO in all the concentrations of serine.

Keywords: Nanomaterial, Serine, XRD, XPS & Bacterial properties

Introduction:

A simple marriage of organic compound and inorganic semiconductor has now become energetic material owing to its dynamic properties and environmental point of view. The interface of these biomolecules with inorganic crystal has been a great significance in different aspects**.** There are many exquisite and fascinating examples of naturally occurring crystals, which are form in the environment of biomolecules. They are biologically controlled and adapted crystal system. Most of the properties of these materials are attributes to the presence of organic

biomolecules such as at ntracrystalline and intercrystalline site of the crystal. The natural examples of the interaction of biomolecules with inorganic crystal are bone/teeth; configuration of DNA binding protein [1], mollusk seashell, zinc finger, guanine crystals found in the skin of many fish [2].The interaction is keenly taking place in different way as per the type of amino acid and crystal. The proper selection of amino acid with particular concentration in synthetic crystal is the key factor for controlling its various properties.

ZnO is non-toxic, biosafe and biocompatible nanostructures. It is one of the special material with ample applications in optoelectronics [3], UV light emitters, transparent conducting electrode for solar cell flat panel display, UV lasers and sensors. ZnO is accessible in high quality bulk single crystal, with variety of morphologies. The requirement of simple synthesis technique and low cost with low temperature processing makes it unique material for employing it into device making. Thin films by doping of Mg in ZnO leads to change in band gap from 3.20 to 3.43eV whereas doping of Cd in ZnO changes band gap from 3.20 to 3.06 eV. ZnO is used in photo catalysis, varistor, and low-voltage phosphor materials.

Amino acids comprise of 1) Amine group 2) Carboxylic group and 3) Side chain group. These groups are making to amino acid to interact, incorporate, adsorb, adapt, modify, integrate, adhere and capping with inorganic crystal in a variety of way. The side chain of serine ($C_3H_7NO_3$) bears alcohol (-OH) group. Serine is non-essential amino acid for human being and has one of the simpler structures as compared to other amino acid. Many research groups have investigated the respond of amino acid on gold nanoparticles [4].The carboxyl group in glutamine are active functional group for driving anisotropic growth for Ag nanoparticles [5,6].The detail study of various amino acid interaction with ZnO has been systematically analysed and band gap alteration has reported [7].They have observed the linear relationship between strain induced with modification in band gap of ZnO. In the review of Limo et al [8] the interfacing between metal oxide and biomolecules and their applications has elaborated. ZnO quantum dots functionalized with amino acids are utilized for detection of proteinase activity [9].The band gap of ZnO can be finely and accurately tailored by amino acid [10].From zinc acetate Schiff base complex can be obtained which when heated then ZnO nanoparticles having 50 to 110 nm size [11]. ZnO synthesized by the solvo-thermal reaction of zinc acetate with lysine, arginine and cysteine proved as a non-enzymatic glucose biosensor [12].It has been

reported that ZnO nanotraingles with ~160-400nm height and ~170-420nm edge were synthesized by microwave irradiation method using arginine as a capping agent are investigated as a water pollutant agent under solar irradiation[13].The amino acid in ZnO matrix favors the radiative recombination resulting into strong confinement effect and efficient chirality transfer from amino acid to inter-band excitations in ZnO ;which can be arised by increase in the band gap[14].

The behavior of inorganic compound with the environment of biomolecules is tedius due to complex nature of biomolecules.By taking motivation from nature; our approach is to create biocompatible composite material consisting of ZnO nanostructures modified by amino acid. Moreover, serine has employed in this work to tune the properties of nanostructures of ZnO.

Material & Methods:

a) To carry out this study, Sigma-Aldrich procured $Zn(NO_3)_2,6H_2O$ with 99.9% purity, Serine powder having 99.9% purity and NH_4OH(28.0-30.0% NH_3 basis)were used.

b) Synthesis of serine integrated ZnO nanoparticles:

For typical synthesis of serine integrated ZnO nanoparticles the solution of 0.25M Zn $(NO_3)_2$with pH 6was prepared in distilled water simultaneously 0.025mg of serine powder mixed. In the prepared solution drop-wise 1mlof NH_4OH was added, which thereafter, turns the solution to appear as white in colour. The obtained white colour solution has kept for homogeneous mixing and heating using magnetic stirrer in a silicon oil bath at 95^{o}C for 90 min. After stirring the mixed solution allowed to cool naturally. The obtained white precipitates was then collected and centrifuge at 10,000 rpm of speed for 15 min and the washed repeatedly by distilled water and ethanol. Finally, the washed precipitate was dried at 140^0C in a vacuum oven. The collected powder was treated as serine-integrated ZnO and referred as ZnO-S1 and further used for the characterization. In parallel to this we have synthesized other samples by taking serine powder in the concentration of 0.05, 0.075 and 1.0 mg and treated them as ZnO-S2, ZnO-S3 and ZnO-S4 respectively. Similarly, the above-mentioned synthesized powder without serine was referred as pristine ZnO.

Microtitre Plate Assay:

For the evaluation of antibacterial activity of the pristine ZnO and serine integrated ZnO, we have used microtiter-plate assay on *Escherichia coli(E.coli)*NCIM 2065 bacteria. These bacteriawere obtained from the National Collection of Industrial Microorganisms (NCIM), National Chemical Laboratory (NCL), Pune, Maharashtra, India.The fresh culture was grown and maintained in nutrient broth (NB) (Himedia) at 37°C under shaking conditions (150 rpm).The stock solutions of synthesized powder samples were prepared with a concentration of 200µg/ml in sterile distilled water. These solutions were then subjected to ultra-sonicated for mixing of powders with water.Round bottomed 96 well microtiter polystyrene plates (Tarson, India) were used for this experiment.

Initially for the preparation of 96 well plates first row was assigned to serine, second assigned to ZnO, third assigned to ZnO-S1, fourth assigned to ZnO-S2, fifth assigned to ZnO-S3 and sixth assigned to ZnO-S4. Then 100 µl solution of sterile distilled water was added in column 2 to 12 wells. Now 200 µl of ZnO stack solution was added in second row of first column and then this solution is serially diluted till column 10 of first row by picking up 100 solution every time. The successive two fold dilution obtained were 100, 50, 25, 12.5, 6.25 and 3.12 µg/ml. Same steps were repeated for ZnO-S1, ZnO-S2, ZnO-S3 and ZnO-S4.For the standard negative control reading 50µl of sterile MHB solution was added in 11^{th} well. Now 50 µl of McFarland adjusted culture was added in well of 1 to 10. For the standard positive control reading 50 µlMcFarland adjusted culture was added in 12^{th} well.

The above-mentioned preparation of 96 well plates was done in three sets. These prepared three sets of plates were incubated overnight at 37ºC and ELISA microtire plate reader (Spectramax M2, USA) was used to measure the optical density (OD) at wavelength = 540 nm. The growth inhibition percentages of *E. coli* at different concentrations were calculated using following relation

$$\text{Percentage cell inhibition} = \frac{(At-Ab)}{(Ac-Ab)} \times 100$$

where, *At* is OD of test compound, *Ab* is OD of blank (negative control) and *Ac* is a OD of control (positive control).

Characterization:

The structural analyses of the samples were taken by X-Ray Diffraction (XRD). It was performed using Bruker AXS D8 Advance Diffractometer. FESEM images for control of *E.coli* cells were captured by FEI-SEM,QUANTA 200 3D, tungstenfilament. SEM pictures were taken by JEOL, JSM-6360A.The microtiter plate reading were recorded by microtiter plate reader SpectraMax M2.

Result & Discussion:

X-Ray Diffraction:

XRD is first step for the analysis of structure, phase and crystallinity of the serine modified ZnOnanoparticles. Following figure 1 indicates the XRD pattern of synthesized ZnOnanoparticlesand ZnOnanoparticles with increasing the concentration of serine in θ-2θ scan mode.The diffraction pattern of ZnO shows pure and crystalline phase.Additional peaks corresponding to impurities like Zn, Zn-OH or $Zn(OH)_2$ are not observed in ZnO control sample. All the diffraction prominent peaksare corresponding to Wurtzite structure having JCPDS Card No.01-079-2205 with space group P63mc.The increase in concentration of serine in ZnO host has not altered the crystal structure for ZnO-S1 and ZnO-S2. Whereas a new peak is observed at ~57^0(labeled by *****) for ZnO-S3 and ZnO-S4 concentration. For higher concentration of serine (0.15 mg/mL) the series of additional peaks were observed. The Bragg's diffraction peaks of serine modified ZnO manifest little reposition. The diffraction peaks are shifted and broadening

is seen which are the implications of change in lattice parameters due to intervening *of serine molecule with the ZnO.*

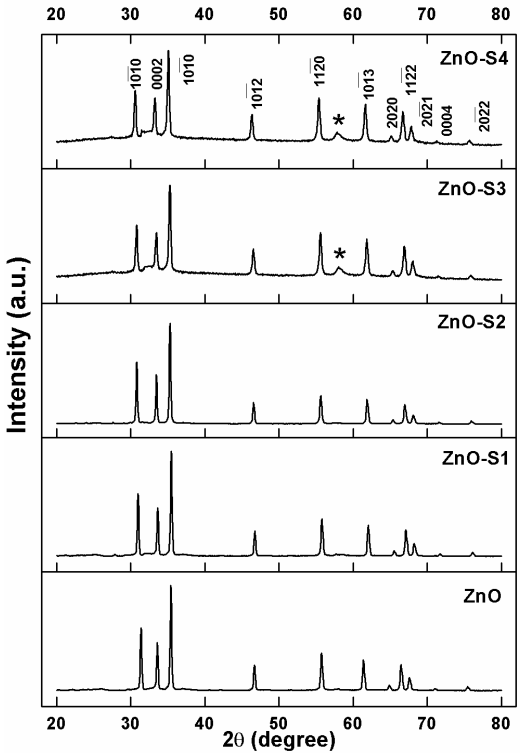

Figure 1 XRD pattern for ZnO and serine modified ZnO

Table 1 Variation of FWHM for the $10\bar{1}0$ and 0002 planes by incorporation of Serine

Sample	FWHM(degree)		d-spacing (A^0)	
	$10\bar{1}0$	0002	$10\bar{1}0$	0002
ZnO	0.192	0.158	2.8464	2.6645
ZnO-S1	0.200	0.202	2.8826	2.6680
ZnO-S2	0.216	0.202	2.9010	2.6788
ZnO-S3	0.221	0.214	2.9010	2.6788
ZnO-S4	0.255	0.221	2.9197	2.6940

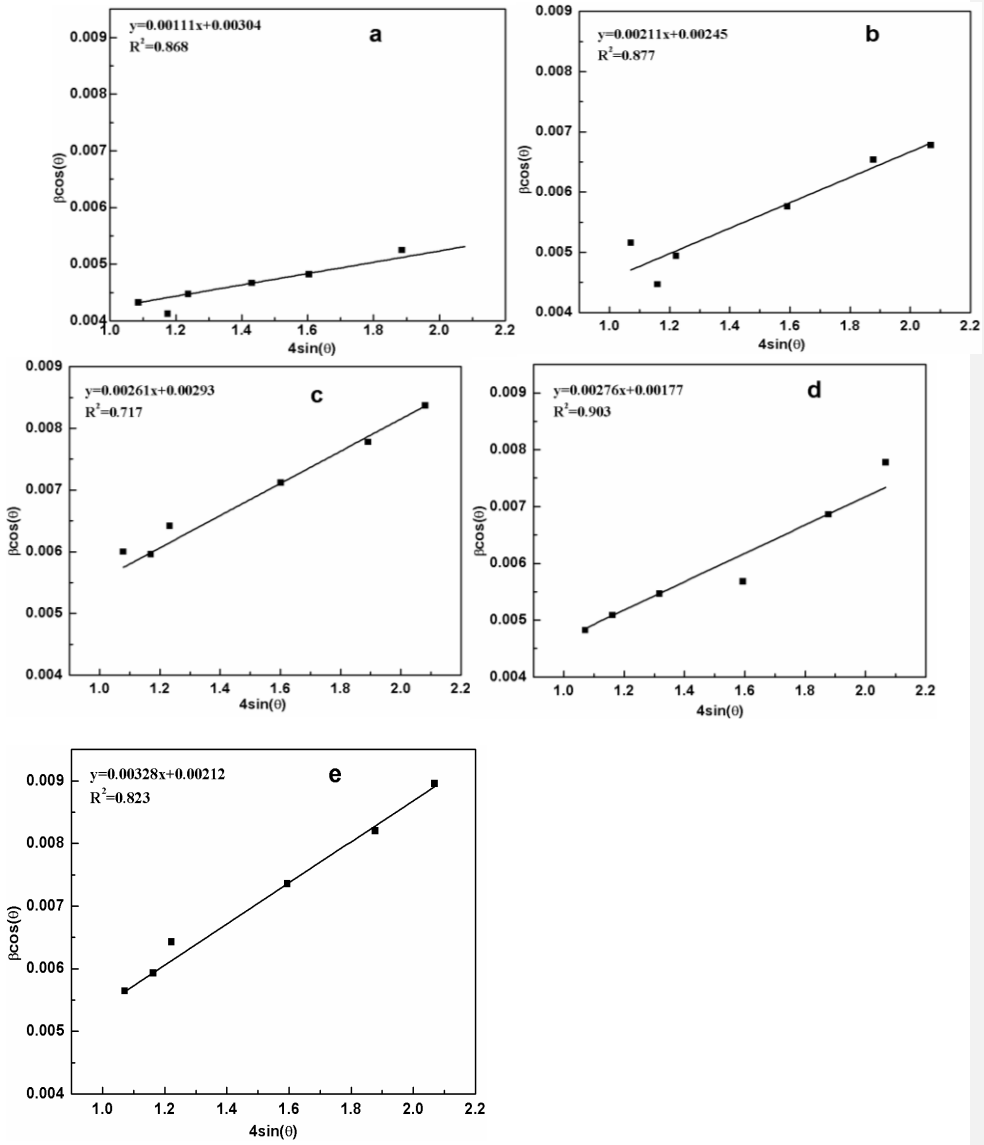

Figure 2 Strain estimation from W.H. method for :a) ZnO , b)ZnO-S1, c)ZnO-S2 ,d)ZnO-S3 and e) ZnO-S4nanoparticles

Table 2 Representation of strain and size with serine estimated by W.H.method

Sample	$\epsilon(X10^{-3})$	D (nm)
ZnO	1.11	30.4
ZnO-S1	2.11	24.5
ZnO-S2	2.61	29.3
ZnO-S3	2.76	17.7
ZnO-S4	3.28	21.2

The diffraction peaks revealed slight shift towards lower angle for the ZnO-S3 and ZO-S4 samples. The lattice parameters calculated for ZnO and serine mediated ZnO shows the intervening of serine in ZnO leads to develop strain in the crystal. The c-axis has observed to strained maximum as compared to other lattice parameters due to incorporation. Since, serine has shown different communication with different faces of ZnO as both lattice parameters are showing different strain by addition of serine. In addition, with this the intervening of serine leads to width of the diffraction peaks to increase. The observed FWHM of peak is consequence of sample and instrument. Therefore, for accurate calculation of size and strain the FWHM was corrected by following equation (I) given by

$$\beta=[(\beta_M)^2-(\beta s)^2]^{1/2}\text{----------(I)}$$

where, β_M is measured FWHM and β_s is instrumental FWHM. The FWHM corrected by above formula corresponding to peaks $10\bar{1}0$ and 0002 are indicated in following table 1. Eventually the average crystallite size also decreases with serine. The average crystallite size calculated by modified Scherrer formula given by

$$\text{average crystallite size}=\left(\frac{K\lambda}{\sqrt{(\beta_M^2-\beta_S^2)}cos\theta}\right)+\eta tan\theta \text{ ----------(II)}$$

where,K is the shape factor ~ 0.9, $\beta_M$is the measured FWHM of the diffraction peak where the Bragg's condition is satisfied and β_S is instrumentFWHM from the standard sample, η is the strain observed along c-axis. The influence of various amino acid on calcite was screened and calcite crystal responds to amino acid by generation of lattice strain and distortion [15].The average crystallite size found to be ~ 31nm.

It is evident from above table that serine incorporation generates impact on particle size, lattice parameter and interplanar distance. In another words serine induces the lattice distortion in ZnO host crystal. The concentration for ZnO-S4 shows maximum influence on ZnO matrix.

Generally, strain induced in lattice parameter and sizes are responsible for peak broadening. The strain developed can be given by $\epsilon \approx \beta/4\tan\Theta$ .We have employed Williamson-Hall method for the details of strain induced by serine in ZnO matrix. The Williamsons-Hall equation in uniform deformation model is given by

$$\beta cos\Theta = \frac{K\lambda}{D} + 4\epsilon sin\Theta \text{----------(III)}$$

where, K is the shape factor ~ 0.9,D is crystallite size, ϵ is strain developed due to crystal imperfection and distortion. Above equation III presumes the strain is uniform in all directions. The value of $\beta cos\Theta$ *and* $4\epsilon sin\Theta$, was taken from y-axis and x-axis respectively; linear fitting of this graph was done. The strain was calculated from the slope and crystallite size was estimated from y-intercept of the linear fitted line. The observed strain and size of the samples with increase in serine concentration is given in the table2.

Room Temperature Photoluminescence:

The important characteristics of optical properties of the composite can analyzed by photoluminescence study. This technique investigates band gap and defect of impurity induced transitions. Fig. 3displays the room temperature photoluminescence of ZnO and ZnO-Si (i=1-4) composite within the wavelength of 350-600nm. All samples indicate intense and broad peak at ~ 376.77nm in agreement with the earlier reported data [16].This peak is observed due to significant absorption at absorption edge of ZnO. Xiao et al. has been analyzed broadening and splitting in near band edge in UV region in case of 20nm grain and also had discussed that this observation of broadening can assigned to quantum confinement effect [17].

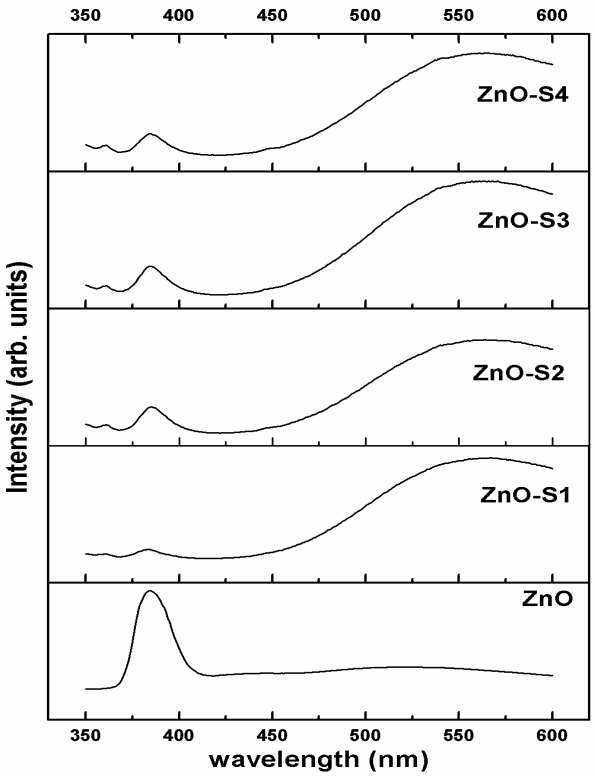

Figure 3 Room Temperature Photoluminescence of ZnO with increase in serine

Accompanying with this all synthesized samples exhibits broad luminescence band between the wavelength scale of ~450-600nm was observed. Since this broad luminescence is less prominent in ZnO while it becomes more intense in the serine-ZnO composite with serine. It was reported that the inception of violet is presence of zinc interstitial [18], zinc vacancy [19]. Blue emissions are observed due to oxygen vacancy [20]. This broad luminescence band observed in the visible region has cardinal importance in determining the defects present in ZnO samples. Impurity atoms are also responsible for this contribution in visible scale. Intrinsically in ZnO lattice zinc atoms are located at half of tetrahedral positions and octahedral sites are empty [21]. This leads to availability of favorable condition of atoms to accommodate and defects are

inherently present. Serine ($C_3H_7NO_3$) integration in ZnO matrix has generated more intense visible luminescence as compared to ZnO which implies that the defects are enhanced due to serine.

SEM:

Morphological analysis of the synthesized samples is effectively done by FE-SEM. Serine mediated ZnO nanostructure was synthesized at pH 8-9 in this study. Serine is either protonated or deprotonated decided by pH of the solution. Serine has pKa value 2.21 for terminal carboxyl group and 9.15 for terminal α-amino group. It has CH_2OH as a side chain. At pH 8-9 carboxyl group is deprotonated (pH>pKa of $–CO_2H$) whereas amino group is half protonated and half deprotonated (as little difference between pH & pKa of $–NH_3^+$).Along these lines the overall charge on serine molecule is -0.5 by carboxylic acid at pH ~9.Thus owing to the interaction between serine and ZnO the morphology get altered. The transition in morphology has revealed by the SEM images shown in figure 4.

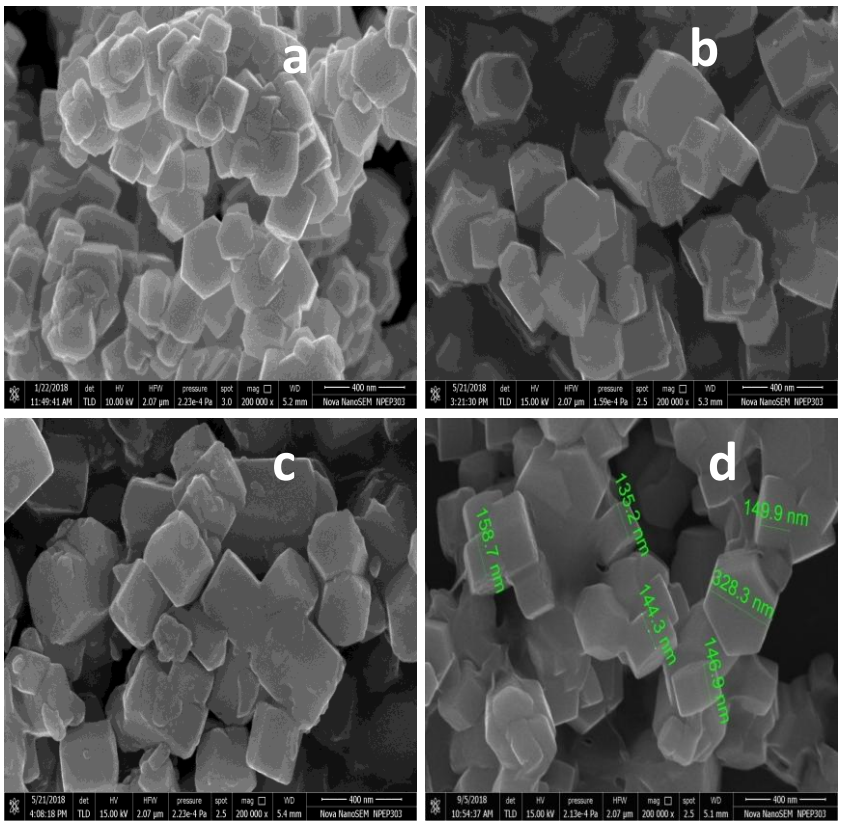
a
b
c
d
158.7 nm
135.2 nm
149.9 nm
328.3 nm
144.3 nm
146.9 nm

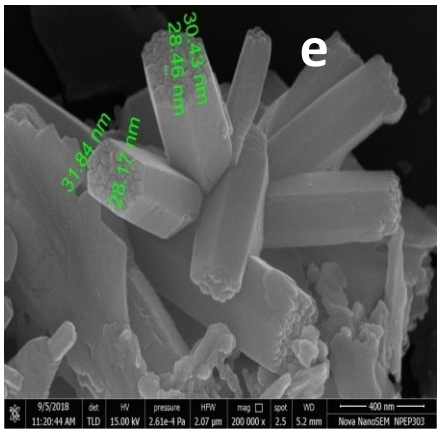
e
30.43 nm
28.46 nm
31.84 nm
28.17 nm

Figure 4 FE-SEM images of synthesized samples with increase in serine concentration: a) ZnO, b) ZnO-S1, c) ZnO-S2, d) ZnO-S3 and e) ZnO-S4

SEM image of ZnO has depicted the hexagonal disc like structure which is greatly varied as serine intervening takes place. The crystal growth gets favored in a particular direction as directed by serine molecules. Preferentially COO^- group reacts with ZnO surface which results to advance in morphology [22] .The crystallite size estimated by W.H. method agrees with the size observed by FE-SEM images.

X-Ray Photoelectron Spectroscopy (XPS):

The sample was taken in the palletized form for the XPS spectra. For the identification of existence of serine in the synthesized samples we have performed the XPS. The analysis of the XPS spectra of carbon atom was performed. The fig. 5 represents the XPS of Carbon atom in the serine modified sample of ZnO for maximum concentration of serine (ZnO-S4). It exhibits the sign of confirmation of serine molecules communication with ZnO. The deconvoluted peak of C1S shows three distinct peaks. First peak observed at 284.89eVwhich attributes to carbon atom belonging to methyl group, 286.65eVcorresponding to carbon atom belonging to carbon atom in the environment of Nitrogen atom of amino group and 288.70eV attributed to carbon atom belonging to carboxyl group. The same species were observed in the interaction of alanine with ZnO surface [22].Only single peak corresponding to carbon atom was observed in the pristine ZnO sample.

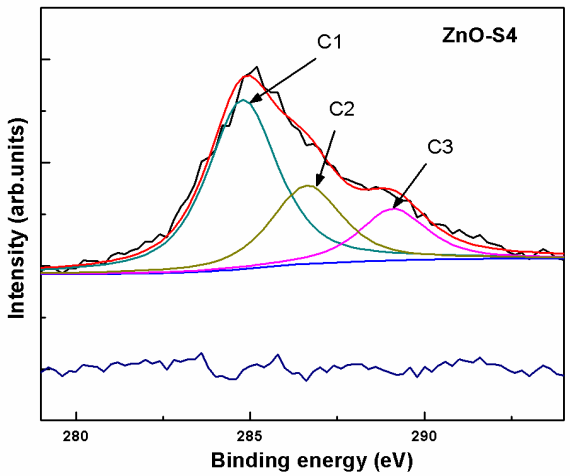

Figure5. XPS of C1S peak with maximum concentration of serine in ZnO

Microtitre Plate Assay:

To evaluate the effect of serine on antibacterial activity of ZnO we have performed this assay for *E.coli* we have used above mentioned equation 3).Figure 6shows the divergence in percentages of cells inhibited with varying concentrations of ZnO and serine integrated composite. It is evident that ZnO shows good antibacterial activity as expected whereas the composite shows decreasing in it as serine concentration increases. This is revealed that the % cell inhibition of *E.coli* in the presence of the synthesized samples is indicating unprecedented observation as compared with pristine ZnO.

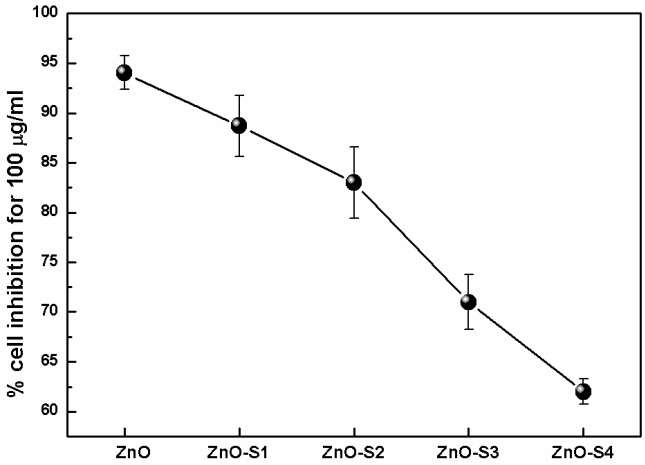

Figure6 % cell inhibition of *E.coli* by the samples

Conclusion: Current study concludes that the biomolecules like amino acid are playing crucial role with the interaction of inorganic material. While in composite of serine with ZnO the crystal structure indicates development of strain in the ZnO crystal, remarkable modification in morphology and enhancement in visible luminescence. The XPS spectra of carbon atom show footprints of existence of serine in the synthesized composite. The integration of serine in ZnO has confirmed by weaning of antibacterial activity of ZnO. This trend of weaning of antibacterial activity of ZnO has observed with increase in concentration of serine.

Acknowledgement: Authors are thankful to Savitribai Phule Pune University, Pune for providing lab facility to carry out this study. S.Mahakal specially thanks to UGC and Annasaheb Awate College, Manchar for providing support under scheme.

Reference:

[1] Lippard, S.J. and Berg, J.M., 1994. *Principles of bioinorganic chemistry* (Vol. 70). Mill Valley, CA: University Science Books.

[2] Levy-Lior, A., Shimoni, E., Schwartz, O., Gavish-Regev, E., Oron, D., Oxford, G., Weiner, S. and Addadi, L., 2010. Guanine-based biogenic photonic-crystal arrays in fish and spiders. *Advanced Functional Materials*, *20*(2), pp.320-329.

[3] Djurišić, A.B., Ng, A.M.C. and Chen, X.Y., 2010. ZnO nanostructures for optoelectronics: Material properties and device applications. *Progress in quantum electronics*, *34*(4), pp.191-259.

[4] Bhargava, S.K., Booth, J.M., Agrawal, S., Coloe, P. and Kar, G., 2005. Gold nanoparticle formation during bromoaurate reduction by amino acids. *Langmuir*, *21*(13), pp.5949-5956.

[5] Xie, J., Lee, J.Y., Wang, D.I. and Ting, Y.P., 2007. Silver nanoplates: from biological to biomimetic synthesis. *ACS nano*, *1*(5), pp.429-439.

[6] Dickerson, M.B., Sandhage, K.H. and Naik, R.R., 2008. Protein-and peptide-directed syntheses of inorganic materials. *Chemical reviews*, *108*(11), pp.4935-4978.

[7] Brif, A., Ankonina, G., Drathen, C. and Pokroy, B., 2014. Bio-Inspired Band Gap Engineering of Zinc Oxide by Intracrystalline Incorporation of Amino Acids. *Advanced Materials*, *26*(3), pp.477-481.

[8] Limo, M.J., Sola-Rabada, A., Boix, E., Thota, V., Westcott, Z.C., Puddu, V. and Perry, C.C., 2018. Interactions between metal oxides and biomolecules: from fundamental understanding to applications. *Chemical reviews*, *118*(22), pp.11118-11193.

[9] Popow-Stellmaszyk, J., Bajorowicz, B., Malankowska, A., Wysocka, M., Klimczuk, T., Zaleska-Medynska, A. and Lesner, A., 2018. Design, synthesis, and enzymatic evaluation of novel ZnO quantum dot-based assay for detection of proteinase 3 activity. *Bioconjugate chemistry*, *29*(5), pp.1576-1583.

[10] Pokroy, B. and Anastasia, B.R.I.F., Technion Research and Development Foundation Ltd, 2017. *Crystals of semiconductor material having a tuned band gap energy and method for preparation thereof*. U.S. Patent 9,771,263.

[11] Gharagozlou, M., Baradaran, Z. and Bayati, R., 2015. A green chemical method for synthesis of ZnO nanoparticles from solid-state decomposition of Schiff-bases derived from amino acid alanine complexes. *Ceramics International*, *41*(7), pp.8382-8387.

[12] Tarlani, A., Fallah, M., Lotfi, B., Khazraei, A., Golsanamlou, S., Muzart, J. and Mirza-Aghayan, M., 2015. New ZnO nanostructures as non-enzymatic glucose biosensors. *Biosensors and Bioelectronics*, *67*, pp.601-607.

[13] Bhattacharjee, A. and Ahmaruzzaman, M., 2018. α-Amino acid assisted facile synthesis of two-dimensional ZnO nanotriangles for removal of noxious pollutants from water phase. *Journal of environmental chemical engineering*, *6*(4), pp.4970-4979.

[14] Muhammed, M.A.H., Lamers, M., Baumann, V., Dey, P., Blanch, A.J., Polishchuk, I., Kong, X.T., Levy, D., Urban, A.S., Govorov, A.O. and Pokroy, B., 2018. Strong Quantum Confinement Effects and Chiral Excitons in Bio-Inspired ZnO–Amino Acid Cocrystals. *The Journal of Physical Chemistry C*, *122*(11), pp.6348-6356.

[15] Borukhin, S., Bloch, L., Radlauer, T., Hill, A.H., Fitch, A.N. and Pokroy, B., 2012. Screening the incorporation of amino acids into an inorganic crystalline host: the case of calcite. *Advanced Functional Materials*, *22*(20), pp.4216-4224.

[16] Kunj, S. and Sreenivas, K., 2016. Residual stress and defect content in magnetron sputtered ZnO films grown on unheated glass substrates. *Current Applied Physics*, *16*(7), pp.748-756.

[17] Xiao, S.S., Zhao, L., Liu, Y.H. and Lian, J.S., 2013. Nanocrystalline ZnO films prepared by pulsed laser deposition and their abnormal optical properties. *Applied surface science*, *283*, pp.781-787.

[18] Yang, Q., Tang, K., Zuo, J. and Qian, Y., 2004. Synthesis and luminescent property of single-crystal ZnO nanobelts by a simple low temperature evaporation route. *Applied Physics A*, *79*(8), pp.1847-1851.

[19] Heo, Y.W., Norton, D.P. and Pearton, S.J., 2005. Origin of green luminescence in ZnO thin film grown by molecular-beam epitaxy. *Journal of Applied Physics*, *98*(7), p.073502.

[20] Chia, M.Y., Chiu, W.S., Daud, S.N.H., Khiew, P.S., Radiman, S., Abd-Shukor, R. and Hamid, M.A.A., 2015. Structural-and optical-property characterization of three-dimensional branched ZnO nanospikes. *Materials Characterization*, *106*, pp.185-194.

[21] Schmidt-Mende, L. and MacManus-Driscoll, J.L., 2007. ZnO–nanostructures, defects, and devices. *Materials today*, *10*(5), pp.40-48.

[22] Gao, Y.K., Traeger, F., Shekhah, O., Idriss, H. and Wöll, C., 2009. Probing the interaction of the amino acid alanine with the surface of ZnO ($10\bar{1}0$). *Journal of colloid and interface science*, *338*(1), pp.16-21.

Paper 52

Dielectric constant, Density and Refractive Index Study on Mixing Properties of Carbon Tetrachloride-Acetone Binary Liquid Mixtures

Commented [AMD3R2]:

S. P. Kamble

Department of Physics, C.T. Bora College, Shirur Dist. Pune. (M.S.).India

ABSTRACT: In this work the densities, refractive indices and dielectric constants of binary mixture of Carbon Tetrachloride-Acetone; have been measured over the entire range of composition at different temperatures 288.15, 298.15, 308.15 and 318.15 K. Excess dielectric constant, excess molar volume, refractive index deviations, molar refraction and excess molar refraction at different temperatures have been computed from the experimentally measured values of the aforesaid parameters and fitted to the Redlich-Kister equation. Excess dielectric constant, refractive index deviations are positive whereas excess molar volume and molar refraction deviation are negative over entire composition range of Acetone for all temperatures. The results are discussed in the light of intermolecular interactions occurring in the binary mixture. The concentration dependent plots of excess properties were used to explore the complex formation through hydrogen bonding between polar and nonpolar molecules. Estimated coefficients of the Redlich-Kister polynomial and the standard error between excess parameters and Redlich-Kister model along with standard error of the coefficients and 95% confidence intervals are also reported.

Keywords: Density, Refractive index, Dielectric constant, Excess properties, Binary liquid mixtures

*Corresponding author Email: spkamble008@gmail.com

Introduction:

Mixed solvents have a wide range of chemical, biological, pharmaceutical, industrial, biophysics, condensed matter physics, and laboratory applications. Among different solvents, the nonpolar like Carbon Tetrachloride represent an important class of organic solvents due to their high solvating power and a large liquid state range.

Accurate knowledge of thermodynamic mixing properties of binary mixtures has great relevance in theoretical and applied areas of research. These data are needed for design process in chemical, petrochemical and pharmaceutical industries [1].

The density and refractive index of the binary mixtures provides very useful analytical information for industrial purposes [2–5].Refractive index and density measurements of binary liquid mixtures are essential for determination of composition of binary mixtures usually for non-ideal mixtures where direct experimental measurements are performed over the entire composition range.

Most empirical approach for calculating the excess properties is an attempt to explain non-ideality in terms of specific intermolecular interactions. The most widely used rules for predictivity of refractivity in case of binary liquid mixtures are Arago-Biot[6], Gladstone-Dale[7], Lorentz-Lorenz[8-9], Eykman[10], Weiner[11], Heller[12], Kurtz[13], Oster[14]and Eyring-John[15]. Many authors [16-20] have applied these properties to study the structures, solvent-solute interactions and the solvation behaviour in binary liquid mixtures.

The measurement of dielectric parameters is a good tool to study molecular interactions in hydrogen bonded liquids such as esters and halogen group, because each molecule has an electric dipole moment. M. Iglesias et al [21], Resa et al [22], Aralaguppi [23] et al, Jose´ Canosa et al [24] reported excess properties of Acetone in binary mixture,

Very few attempts have been made to study the dielectric behaviour of Carbon Tetrachloride-Acetone binary mixture. To gain some insight into the nature of molecular interactions between the associating molecules, a dielectric study of a Carbon Tetrachloride-Acetone system should be helpful.

2. Experimental

Materials:

The chemicals Carbon Tetrachloride and Acetone are obtained from Qualigens fine chemicals and Kemphasol, Mumbai. These chemicals were used without further purification as the supplier claims their purity is more than 99%. The mixtures were prepared by mixing appropriate volume of liquids.

Measurements:

Refractive indices were measured using thermostatically controlled Abbe refractometer with accuracy 0.001units.Water was circulated in to the prism of the refractometer by a circulation pump connected to an external thermostated water bath. Calibration was performed by measuring the refractive indices of doubly distilled water and Acetone at defined temperatures within 0.01 K. The sample mixture was directly injected in to the prism assembly of the instrument using a syringe.

Density of pure components and their mixtures were measured pyknometer having a bulb volume approximately 3 cm^3 and internal diameter of the capillary tube of about 0.275 mm with the precision of density measurements was 10^{-4} g cm^{-3}.

Dielectric constant is measured by indigenouslly designed instrument in our laboratory with accuracy 0.0001.

Table1: Literature Value of Density, Refractive Index and dielectric constant of pure Carbon Tetrachloride and Acetone at 293.15 K

Liquid/Properties	ρ gm/cc		η_D		ϵ_S	
	literature	Exp	literature	Exp	literature	Exp
CCL_4	1.5940[a]	1.5802[*]	1.4601[a]	1.456[*]	2.2379[a]	2.1689[*]
Acetone	0.7902[a]	0.7853[*]	1.3614[a]	1.355[*]	20.7*[a]	6.1912[*]

[a] CRC Handbook of chemistry # temperature. 288.15 K [*] temperature 298.15 K

3. Results and discussion

Excess properties:

The information related to solute-solvent interaction can be obtained by excess properties [25] related to the dielectric constant, density and refractive index in the mixture.

The excess properties of the mixtures were calculated using the following equation.

$$A^E = A_{Mix} - (A_1 X_1 + A_2 X_2) \quad \ldots\ldots\ldots\ldots\ldots\ldots\ldots\ldots\ldots\ldots\ldots\ldots \quad (1)$$

where, A^E represents the refractive index deviation, excess densities or excess molar volume etc, A_1, A_2 and A_{mix} represent the refractive index or density or molar volume of pure liquids 1, 2 and mixture respectively. The X_1 & X_2 represents the mole fraction of component 1and 2 of the mixtures

The computed results of excess properties have been fitted to a Redlich-Kister type polynomial equation. The estimated coefficient along with standard deviation is listed in tables given below.

Excess dielectric constant: The excess dielectric constant, ϵ^E, which provides qualitative information about molecular interaction in the mixture, can be determined by using equation1. The excess dielectric constant ϵ^E values are positive over the entire range of composition and values of excess dielectric constant decreases as temperature increases depicted in figure 1. This is due to the constituents of the binary mixture interact in such a way that they act as H-bonded 'structuremakers' with parallel dipolar alignments in the same direction, which results in increase of effective number

of aligned dipoles contributing to the mixture dielectric polarization. The magnitude of values is the evidence of the strength of unlike molecules H-bond interactions i.e., the higher the values the stronger is the H-bond molecular connectivities [26].

Excess molar volume and refractive index deviation:

Many researchers have been tried to derive information about excess density, refractive index deviation and excess molar volume in binary mixtures and tertiary mixtures of polar and non-polar solvents for molecular conformations, and derived results showed that excess density and refractive index deviation have the same sign of excess properties with opposite to excess molar volume [27, 28].Molar volume determined by using the relation

$$V_m = (X_1M_1 + X_2M_2)/ \rho_{mix} \quad \text{----------2}$$

The excess molar volume V^E values are negative over the entire range of composition and V^E curves are shifted in a regular way with increasing temperature as shown in figure 2. The negative V^E values indicate that there is a volume contraction on mixing i.e. his composition range corresponds to the most dens and packed mixed solvent.

This result shows the molecular correlations, between Acetone and CCL_4 is strong. According to Fort and Moore [29], the excess volumes can be interpreted into three terms: namely of physical, chemical and structural effects. The physical effects involve dispersion forces in the mixture, adding negative contributions to V^E. The chemical interactions result in a decrease in volume, which includes charge transfer-type forces and other complex-forming interactions between the two species; thereby these chemical effects contribute negative values of V^E. The structural effects that arise from the geometrical fitting of one component into the other are due to the different molar volumes and free volumes of pure components and negative contributions to V^E. This negative excess molar volume V^E is an indication of strong molecular interaction in the liquid mixtures and is attributed to charge-transfer, dipole–dipole interactions and hydrogen bonding between the Acetone and CCL_4 molecules. The magnitudes of the contribution will vary with the components and composition of the mixtures. Esters (Acetone, ethyl acetate, n-propyl acetate and n-butyl acetate) are weak hydrogen accept acceptors and they are not donors due to the lack of an acidic proton. In these mixtures the observed negative values of V^E are attributed to the combined effect of specific interactions and molar volume is outweighed the dispersion interactions. The graphical evidence supports the above said forces are operating between the unlike molecules of Carbon Tetrachloride and esters. Carbon Tetrachloride is

strongly associated liquid, when it is mixed with esters it looses its aggregates contributing to the contraction of volume, hence declustering of Carbon Tetrachloride molecules [30].

From figure 3 it is observed that he refractive index deviation values (η_D^E) are positive over the entire range of composition and it increase as temperature decreases indicating existence of the strong intermolecular interaction.

Molar refraction, molar refraction deviation and molar polarization

The structural property of liquid and liquid mixtures can be integrated through refractive indexes employing molar refraction. In general molar refraction increases with molecular weight (pure or mixture) for symmetric and asymmetric molecules. Density and refractive index depend on molecular weight and nature of solution. Density and refractive index values decrease with increase of temperature from 288.15K to 318.15K

With the aim of gathering further information about the specific intermolecular interactions in the studied binary mixture, we have investigated the molar refraction Rm, defined by the Lorentz–Lorenz equation [31]:

$$Rm = (n^2 - 1/ n^2 + 2)\, Vm \quad \text{----------3}$$

Where, Vm is the molar volume of liquid. It must be remembered that Rm is a computed property strictly related to the electronic mean molecular polarisability, of a real system by the equation:

$$Rm = N_A \alpha / 3\epsilon_0 \quad \text{----------4}$$

Where N_A is the Avogadro constant, ϵ_0 is the dielectric constant of free space and α is the mean polarizability of the liquid.

Generally, the polarizability consists of two contributions, the first one measuring the ability with which the molecules will be deformed by an electric field, and the other due to the orientation of the molecular dipoles under the action of this field. The second effect depends on the temperature, whereas the first is practically temperature independent. The higher the permanent electric dipole moment of molecules, the more important are the orientational effects. Since we measured the refractive index in the optical region, the polarisability should not include orientational effects. Therefore, the molar refraction should not depend on temperature over a small temperature range. This shows that Rm values can, in fact, be associated with electronic polarisabilities. The Rm values obtained for the CCl_4–Acetone solution lie in the range 17. 48 cm3 mol^{-1} (pure CCl_4 at 288.15 K) to 26.52 cm3 mol^{-1} (pure CCl_4 at 318.15 K). Figure 4 reproduces the experimental trend of molar

refraction versus mole fraction for the investigated system from 288.15 to 318.15 K. This plot shows that the Rm profiles and, as a consequence, the electronic polarization of the mixture, increase monotonously only with Acetone mole fraction. As can be seen in Table 4, the polarizability of the CCl_4–Acetone mixture is slightly affected by the temperature variation in the range selected.

In considering volume change and related effects when two liquids are mixed, it is very important to consider the changes of the molar volume and the appearance of specific interactions. Since carbon tetrachloride has a capacity for self-association and association complexes between carbon tetrachloride and Acetone species is formed in the binary mixtures, we believe that the observed change on mixing for these two functions is due to a lowering of the molar volume and the presence of specific interactions leading to hydrogen-bonded intermolecular complexes. We, therefore, conclude that the formation of new hydrogen-bonded species in the mixture and the lowering of the free volume are the primary contributors to the mixture effect for the system reported here [32].

The molar polarization is also an important parameter which gives the information about inter and intramolecular association and internal rotation with the temperature variation. The interionic distance in the crystalline state is not exactly additive for the radii of the constituent ions, it can be explains it in terms of polarization. As can be seen form table 3 molar polarization decreases as mole fraction of Acetone increases and also it decreases as temperature increases.

The results presented in the paper were expected to be useful for design purposes. Also these results have been exploited in a variety of applications involving fibers, fabrics etc. Some applications are meant for quality control, some for processing and some for functional performance. The major application areas where the dielectric properties have been used in various fields of textile technology.

4. Conclusion:

In this article, the densities and refractive index of CCL_4-A mixture are reported at 288.15, 298.15, 308.15, and 318.15K temperatures as a function of Acetone composition. From these data, excess molar volumes (V^E), deviations in refractive index (n_D^E), and excess molar refraction (ΔRm), have been computed, and were correlated by the Redlich–Kister-type equation. In all cases, for each Acetone composition, both the absolute excess molar volumes and excess molar refraction noticeably increase over the entire mole fraction with a decrease of temperature from 318.15 to 288.15 K. These results are discussed in terms of molecular interactions between the mixing components.

Furthermore, we have obtained no dependence of the corresponding molar refraction calculated using the Lorentz–Lorenz relation on temperature.

References:

[1] Sangita Sharma, Pragnesh B. Patel, Rignesh S. Patel and J. J. Vora; E-Journal of Chemistry, 4, 3 (2007) 343-349.

[2] Glasstone, S.: Tratado de Qu´ımica F´ısica. Aguilar, Madrid (1970)

[3] Belda, R., Herraez, J.V., Diez, O., Phys. Chem. Liquids 42, (2004) 467–479.

[4] Belda, R., Herraez, J.V., Diez, O., Chem. Liquids 43, (2005) 91–101.

[5] Tasic, A.Z., Djordjevic, B.D., Grozdanic, D.K., Radojkovic, N., Chem.Eng. Data 37, (1992) 310–313.

[6] Arago D F J and Biot J B, Mem. Acad. Fr. 1806, 7.

[7] Gladstone F and Dale D, Philos. Trans. R. Soc. 1858, 148, 887.

[8] Lorentz H A, Weid. Ann., 9, 641(1880).

[9] Lorenz L Weid. Ann., 11, 70 (1880).

[10] Bottcher C J F, Theory of Electric Polarization, Elsevier, Amsterdam, (1952).

[11] Weiner O, Leipz. Ber. 62, 256(1910).

[12] Heller W, Phys. Rev., 68, 5(1945).

[13] Kurtz S S and Ward A L J, Franklin Inst., 222, 563(1936)

[14] Oster G, Chem. Rev., 43, 319(1948).

[15] Eyring H and John M S, Significant liquid structures, John Wiley, New York, (1969).

[16] Lal K, Tripathi N and Dubey G P, J. Chem. Eng. Data, 45, 961(2000)

[17] Pal A and Kumar A, J. Chem. Eng. Data, 43, 143(1998).

[18] Pineiro A, Brokos P, Amigo A, Pintos M and Bravo R, J. Chem. Thermodyn., 31, 931(1999).

[19] Aminabhavi T M and Banerjee K, J. Chem. Eng. Data, 43, 509(1998).

[20] Page M and Jolicoeur C, J. Chem. Thermodyn., 25, 139(1993).

[21] M. Iglesias, B. Orge, J. M. Canosa, A. Rodríguez, M. Domínguez, M. M. Piñeiro and J. Tojo; Fluid Phase Equilibria,Vol. 147, 1-2, (1998)285-300.

[22] José M. Resa, Cristina González, Marina Juez, Salomé Ortiz de Landaluce, and Miguel Iglesias; Fluid Phase Equilibria, 217, 2, (2004) 175-180.

[23] M. I. Aralaguppi, C. V. Jadar, and T. M. Aminabhavi. D. Ortego,S. C. Mehrotra; J. Chem.Eng. Data, 42, 2(1997) 301–303.

[24] Jose´ Canosa, Ana Rodrı´guez, Beatriz Orge, Miguel Iglesias, and Jose´ Tojo J. Chem. Eng. Data, 42 (1997) 1121-1125.

[25] Hasted, J. B. Aqueous Dielectrics; Chapman and Hall: London, (1973).

[26] R.J. Sengwa, Vinita Khatri, Sonu Sankhala; J. Molecular Liquids, 144, (2009) 89–96.

[27] Arvind Kumar, Solution Chem., 37 (2008) 203–214

[28] Pietro Baraldi, Maria Grazia Giorgini, Daniela Manzini, Andrea Marchetti and Lorenzo Tassi; J. Sol. Chemistry, 31, 11, (2002).

[29] R.J. Fort and W.R. Moore, Trans. Faraday Soc. 62, 1112 (1966).

[30] Veeraswamy Jaana and Satyanarayana Nallani; Rasayan J. Chem; 1, 3 (2008) 612-617.

[31] A.Zˇ .Tasic´, B.D. Djordjevic´, D.K. Grozdanic´, and N.J. Radojkovic´, J. Chem. Eng. Data 37, 310, (1992).

[32] Manuel Lazarte, Ana C. G´omez Marigliano, and Horacio N. S´olimo J. Solution Chemistry, 33, 12, (2004).

Table2: Density, Refractive Index and Dielectric constant of CCL4 and Acetone binary mixture at various temperatures

Mole fraction of Acetone	288.15 K			298.15 K			308.15 K			318.15 K		
	P	η_D	ϵ	P	η_D	ϵ	P	η_D	ϵ	P	η_D	ϵ
0.0000	1.6030	1.461	2.4507	1.5827	1.456	2.2280	1.5650	1.450	2.0871	1.5404	1.444	1.8388
0.0833	1.5392	1.452	3.1100	1.5172	1.446	2.9301	1.4974	1.440	3.1100	1.4758	1.433	2.5981
0.1697	1.4733	1.442	4.0753	1.4514	1.436	3.7349	1.4328	1.430	3.6352	1.4052	1.423	3.2129
0.2595	1.4001	1.432	4.6209	1.3808	1.426	4.3530	1.3629	1.420	4.0875	1.3405	1.413	3.7349
0.3528	1.3359	1.422	5.0589	1.3192	1.416	4.8425	1.3006	1.410	4.6306	1.2765	1.403	4.3530
0.4498	1.2703	1.413	5.1887	1.2546	1.407	5.0350	1.2369	1.400	4.7802	1.2117	1.393	4.5215
0.5509	1.2053	1.403	5.4182	1.1900	1.397	5.2398	1.1741	1.391	4.9284	1.1523	1.384	4.6879
0.6561	1.1381	1.393	5.7183	1.1241	1.387	5.3516	1.1087	1.381	5.0668	1.0882	1.375	4.9783
0.7658	1.0719	1.383	5.8956	1.0595	1.377	5.5687	1.0460	1.372	5.4247	1.0275	1.366	5.2398
0.8804	1.0079	1.373	6.1247	0.9987	1.368	5.8455	0.9850	1.363	5.6278	0.9703	1.357	5.5687
1.0000	0.9440	1.364	6.1912	0.9350	1.359	6.1500	0.9267	1.354	5.8956	0.9113	1.348	5.8455

Table 3: Molar polarization and Molar refraction of CCL4 –Acetone binary system at various temperatures

Mole fraction of Acetone of CCl_4	288.15 K		298.15 K		308.15 K		318.15 K	
	P_m	R_m	P_m	R_m	P_m	R_m	P_m	R_m
0.0000	31.2766	26.3317	28.2278	26.4186	26.5596	26.4139	21.8188	26.5252
0.0833	39.4827	25.7951	37.9776	25.8684	41.1789	25.9033	34.6607	25.9197
0.1697	48.1989	25.1932	46.0938	25.2725	46.6852	25.2927	42.3795	25.4212
0.2595	51.9998	24.6623	50.8843	24.7023	50.3689	24.7192	47.3602	24.7639
0.3528	54.0976	23.9086	53.5020	23.9089	53.9121	23.9434	51.9654	24.0274
0.4498	54.1009	23.1518	53.9208	23.1426	54.2695	23.1162	52.5614	23.2314
0.5509	54.3006	22.2493	54.0785	22.2382	54.0719	22.2372	52.5868	22.2977
0.6561	54.5169	21.2833	53.4452	21.2576	53.6743	21.2545	53.1726	21.3500

0.7658	53.6481	20.1822	52.8392	20.1345	53.7911	20.1514	52.8595	20.2189
0.8804	52.3246	18.8997	51.7063	18.7983	52.2794	18.8275	52.0148	18.8270
1.0000	49.7267	17.4892	50.0588	17.4392	50.3968	17.3758	50.1993	17.3988

Table4: Parameters of Excess Molar Volume

Temperature		a_0	a_1	a_2	a_3	Standard Error of the Estimate
288.15 K	Value of coefficient	-68.5154	-24.0163	-8.45737	2.026404	0.0781
	95% (+/-)	0.426965	1.67628	1.97544	4.381868	
298.15 K	Value of coefficient	-68.231	-23.0821	-7.68474	-1.03296	0.1277
	95% (+/-)	0.698162	2.74101	3.230189	7.165118	
308.15 K	Value of coefficient	-67.4529	-22.7202	-4.59594	3.968055	0.0691
	95% (+/-)	0.378038	1.48419	1.749069	3.879738	
318.15 K	Value of coefficient	-67.4392	-21.0682	-6.91572	-0.60307	0.1231
	95% (+/-)	0.995777	3.909456	4.607164	10.21949	

Table 5: Parameters of Refractive index deviation

Temperature		a_0	a_1	a_2	a_3	Standard Error of the Estimate
288.15 K	Value of coefficient	2.01E-02	5.51E-03	-8.50E-05	-2.13E-02	2.25453E-10
	95% (+/-)	1.23E-09	4.84E-09	5.70E-09	1.27E-08	
298.15 K	Value of coefficient	1.61E-02	3.33E-03	-5.27E-03	-1.16E-02	0.000226586
	95% (+/-)	1.24E-03	4.86E-03	5.73E-03	1.27E-02	
308.15 K	Value of coefficient	1.24E-02	-1.86E-03	1.52E-03	9.02E-04	0.000187955
	95% (+/-)	1.03E-03	4.03E-03	4.75E-03	1.05E-02	
318.15 K	Value of coefficient	8.50E-03	-1.15E-04	2.17E-03	9.29E-03	0.000187955
	95% (+/-)	8.88E-04	3.49E-03	4.11E-03	9.11E-03	

Table6: Parameters of Molar Refraction deviation

Temperature		a_0	a_1	a_2	a_3	Standard Error of the Estimate
288.15 K	Value of	6.557459	2.182981	0.372988	0.679636	0.025216
	95% (+/-)	0.137873	0.541294	0.637897	1.414966	
298.15 K	Value of	6.516717	2.229956	0.305443	-0.06263	0.031941
	95% (+/-)	0.17464	0.685643	0.808008	1.7923	
308.15 K	Value of	6.637415	2.008148	1.022126	0.851006	0.025566
	95% (+/-)	0.139784	0.548798	0.64674	1.434581	
318.15 K	Value of	6.758842	2.249116	0.51045	0.949414	0.037402
	95% (+/-)	0.204503	0.802885	0.946174	2.098777	

Table 7: Parameters of Excess Molar Polarization

Temperature		a_0	a_1	a_2	a_3	Standard Error of the Estimate
288.15 K	Value of	63.1361	-28.7737	4.55200	43.9798	0.436212
	95% (+/-)	2.38505	9.36380	11.0349	24.4773	
298.15 K	Value of	67.8568	-28.0566	-2.7149	25.6072	0.136511
	95% (+/-)	0.74639	2.93037	3.45335	7.66013	
308.15 K	Value of	69.7389	-24.0724	29.0376	-18.8547	0.665449
	95% (+/-)	3.63844	14.2846	16.8339	37.3406	
318.15 K	Value of	74.8305	-24.9736	10.1480	9.35508	0.521754
	95% (+/-)	2.85276	11.2000	13.1989	29.2774	

Figures

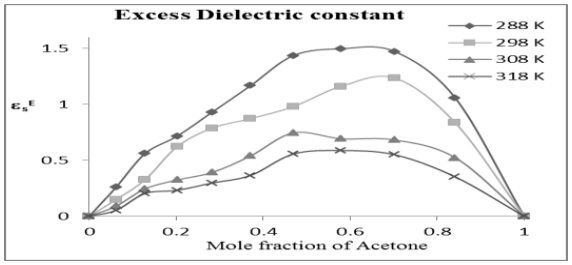

Figure 1: Variation of excess dielectric constant with mole fraction of Acetone

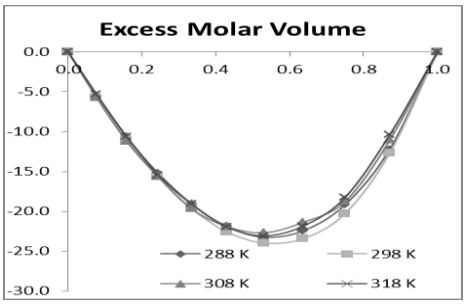

Figure 2: Variation of excess molar volume with mole fraction of Acetone

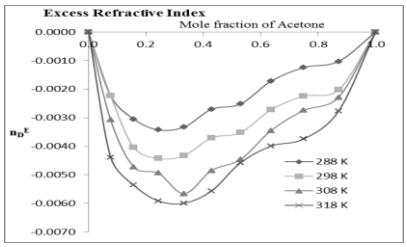

Figure 3: Variation of refractive index deviation with mole fraction of Acetone

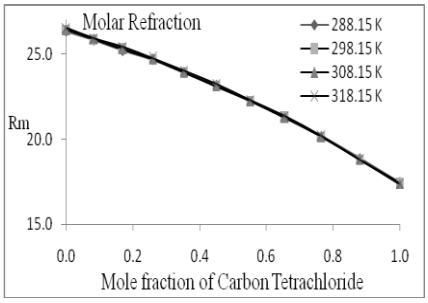

Figure 4: Variation of molar refraction with mole fraction of Acetone

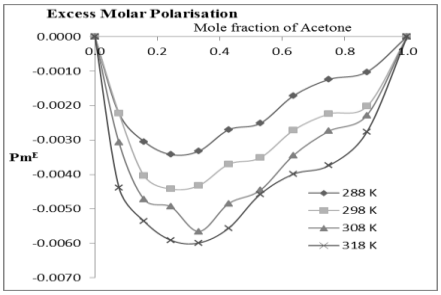

Figure 5: Variation of excess molar Polarization with mole fraction of Acetone

Paper 53

Solar photocatalytic degradation of methylene blue using Sb-doped TiO_2 nanoparticles

B.Y. Pagare[a] R.R. Bhosale[b], S.K. Narwade[a,*]

[a] *Department of Chemistry, Shri Anand College, Pathardi, Ahmednagar, Maharashtra, India*

[b] *Department of Chemistry, Arts, Science and Commerce College, Indapur, Pune, Maharashtra, India*

Abstract

Sb-doped TiO_2 were synthesized by sol–gel process combined with surfactant incorporating method. The concentration level of Sb (III) additive was varied systematically from 1 to 11 wt.%. Wide structural and surface characterization of samples was carried out in order to establish a correlation between the effects of antimony incorporation on the TiO_2 photocatalytic properties. Results revealed that the anatase structure is highly stable for Sb/TiO_2 with enhancement in the surface area. UV–Vis diffuse reflectance spectra showed that this dopant was responsible for narrowing the band gap of TiO_2 and shifting its optical response from ultraviolet to visible-light region. The photocatalytic activity of the Sb/TiO_2 catalyst was evaluated in the decomposition of methylene blue solution under solar light irradiation with respect to the content of antimony on the catalyst surface. The results showed that the incorporation of antimony into the TiO_2 seems to enhance the photocatalytic activity of the samples, which is ascribed to the enlargement of specific surface area, photo generated carriers separation, light absorption, as well as the higher surface acidity. The photocatalytic efficiency and activity of the composites remained good, even after three cycles.

Keywords: Sb/TiO_2; Nanomaterials; Solar photocatalysis; Methylene blue.

*Corresponding author. Tel.: +91 02428222736 ; fax: +91 02428223033.
E-mail address: sknarwade1967@gmail.com (S.K. Narwade).

1. Introduction

Photocatalysis has emerged as an effective technique to decontaminate toxic and non-biodegradable environmental pollutants [1-2]. Among various functional metal oxides, TiO_2 is the most nontoxic, highly stable, cost effective, strong oxidant, and noncorrosive semiconductor, which make it more suitable choice for removing organic and inorganic contaminants from the environment [3-4]. The photochemical reactions proceed on a pure TiO_2 surface, when irradiated with ultraviolet light. This barricades the frequent and convenient use of TiO_2 photocatalyst. The increase in redox potential and decrease in the particle size is essential to enhance the photochemical reaction rates. Decreasing the particle size to nano scale, results in the larger surface area per unit mass. Reduction of band gap facilitates the catalyst to make use of solar and visible light energy, which makes it environmentally and electrically suitable photo catalyst [5]. Further, the anatase to rutile phase ratio is also an important factor in enhancing photo catalytic activity. The anatase

phase is kinetically more stable and higher hydrophobicity of this phase increases the absorption of reactive species, while rutile phase scatters light which decreases its absorption power [6-7].

Recently, much attention has been paid in modifying TiO_2 to enhance its catalytic efficiency or expand its applicability under solar irradiation [8]. Different metallic [9] and nonmetallic dopants [10] have been doped to decrease the band gap and increase excitation life time of pure TiO_2. Mao et. al, used nitrogen dopant for the photo-oxidation of organic molecules in water [11]. Shamalah et. al, showed degradation of Brilliant Green dye with Zn and Cu-doped TiO_2 [12]. Moreover, many attempts have been carried out in direction of attaining high surface area photocatalysts to increase active sites by using the support materials like zeolites [13], HZSM-11 zeolite [14], Clinoptilolite [15] and silica–clay composite [16]. Zhang et. al. synthesized mixed platinum catalysts supported on various carbon nanomaterials [17]. The nano Ag/Pt and methyl violet co-doped catalyst was developed resulted in higher photodegradation activities towards various dyes [18]. Elham S. Baeissa investigated the removal of cyanide employing cobalt metal doped on TiO_2–SiO_2 nanoparticles [19]. Nano sheets of Au/$HTiNbO_5$ have also been synthesized by Hsin-Yu Lin, et. al to produce hydrogen from water splitting [20]. The important issue governing the efficiency of photocatalytic oxidative degradation is minimizing electron-hole recombination by maximizing the rate of interfacial electron transfer to capture the photogenerated electron and/or hole. Various n and p type photocatalysts are well documented in the literature. A Na-doped p-type flower-like ZnO photocatalyst (Na:ZnO) that is highly visible-light-sensitive in air at room temperature was synthesized by a continuous flow microreactor [21]. Rh-doped $BaTiO_3$ powder was prepared by the polymerized complex (PC) method, and the photocatalytic activity for H_2 evolution from water was examined. $BaTiO_3$ is a wide-gap n-type semiconductor having a band gap of 3.0 eV. Doping Rh species into the lattice of $BaTiO_3$ resulted in the formation of new absorption bands in visible light region [22]. Different p-type Cu_2O powders were prepared from electro deposition and subjected to analysis of their photocatalytic activity in water reduction [23]. Sb-doped catalyst on different supports has been synthesized previously [24-25]. However, they did not evaluate the effect of concentration level of Sb (III) on crystallite size, specific surface area and phase transformation and surface acidity. The effect of variation of concentration of Sb (III) additive on the particle size and surface area of Sb-doped TiO_2 system is not reported in the literature so far.

In the present study highly pure and stable anatase Sb-doped TiO_2 nanopowders have been synthesized by sol-gel method at lower calcination temperature. The developed procedure is simple and low cost, which avoids the use of hazardous chemical compounds. The synthesized powders were structurally, morphologically and optically characterized and its photocatalytic properties studied under solar light irradiation.

2. Experimental details

2.1.1 Synthesis of Sb-doped TiO_2

In a typical procedure, 25 ml of titanium butoxide was hydrolyzed in 300 ml water containing 0.1M HNO_3 (10 ml) as a catalyst. The procedure was followed by the addition of 10% 10 ml of cationic surfactant cetyltrimethylammonium bromide. The solution was stirred vigoursly overnight to get peroxy sol. To obtain a composition of 1 wt.% Sb (III), a calculated amount of $SbCl_3$ was added to the above solution. The sol was stirred again for 5 h and then kept for aging. After keeping the sol for aging (5 days), it was concentrated and dried at 70°C. Finally, all the samples were calcined at 400°C, using muffle furnace for 2 h. Following this method, the various amounts of Sb (III) (0, 1, 3, 5, 7, 9, and 11 wt.%) were

added to TiO_2.

2.1.2 Photocatalytic activity

Photocatalytic degradation of methylene blue (MB) was carried out by solar light irradiation. About 40 mg of photocatalyst was immersed into a 50 ml (50 ppm) of aqueous MB solution in closed cylindrical Pyrex bottles (100 ml). Prior to irradiation, the suspensions were magnetically stirred in the dark for 30 min to ensure establishment of an adsorption–desorption equilibrium among the photocatalyst, MB and atmospheric oxygen. All the experiments were carried out at the same conditions on May 2014 from 12.00 p.m. to 1.00 p.m. The average insolation of the solar irradiation was 25.28 W/m^2 measured by an UV irradiance meter at range of 375–475 nm. At a given irradiation time interval, 10 ml of the suspension was collected, and then filtered through a Millipore filter to separate the photocatalyst. The changes in MB concentration were analyzed by a UV–visible spectrophotometer and the absorption peak at 650 nm was recorded.

2.1.3 Characterization

X-ray powder diffraction (XRD) patterns have been recorded on a model D8 Bruker AXS with monochromatic Cu radiation (40 kV and 30 mA), over the 2θ collection range of 20-80°. Thermo gravimetric analysis (TG) and differential scanning calorimetric analysis (DSC) was carried out simultaneously in a static N_2 atmosphere, using a Netzsch STA 409 instrument. BET surface area measurements were carried out using a Quantachrome NOVA 1200 instrument. Surface morphology and elemental analysis of the samples were carried out using an energy dispersive spectrophotometer (EDS) (Jeol; JED-2300). The microscopic nanostructures were observed by transmission electron microscopy (TEM; FEI, Tecnai F30, HRTEM, FEG operated at 300 kV). To determine the acidity of the samples, ammonia TPD measurements in the range of 100-600°C were performed in a conventional flow-type apparatus at a heating rate of 10°C min^{-1} in a nitrogen atmosphere. The acidity determination was supported by the TGA studies using 2, 6-dimethylpyridine as a probe molecule. Previously activated samples were kept in a desiccators saturated with vapors of 2, 6-dimethylpyridine at room temperature for 24 h and then subjected to thermal analysis in N_2 atmosphere at a heating rate of 10°C min^{-1}. The fraction of weight loss in the range of 300-600°C was calculated and taken as a measure of Brönsted acidity of the samples. FT-IR spectra were recorded on a Shimadzu-8400 spectrometer in the range of 4000-500 cm-1. UV-Vis diffuse reflectance spectra (UV–Vis–DRS) were recorded in an air at room temperature in the wavelength range of 200–800 nm using a PE LAMBDA35 spectrophotometer.

3. Results and discussion

3.1 XRD analysis

To understand phase symmetry in the calcined samples, a systematic X-ray diffraction study was undertaken. Fig. 1(a–g) shows the XRD patterns of the pure TiO_2 and with different concentration levels of Sb (1, 3, 5, 7, 9 and 11wt.%) for Sb/TiO_2 system, respectively. Pure TiO_2 (Fig. 1(a)) shows two main peaks at 2θ =25.5 and 27.5, corresponding to (101) phase of anatase and (110) phase of rutile, respectively. In the case of Sb-doped TiO_2 (Fig. 1(b-g)), the rutile phase is < 1%, which means metal-doping retards

the transformation from anatase to rutile phase. Metal-doping of the TiO_2 stabilizes a well-crystallized pure anatase upon calcination at 400°C, in contrast with the simultaneous growth of the rutile phase observed for the pure TiO_2. The results are in good agreement with previous reports [26-27]**.** Further, all peaks measured by XRD analysis could be assigned to those of TiO_2 crystal. No peaks corresponding to the metal oxide is detected, suggesting that it exist as the amorphous phase without getting incorporated into the TiO_2 phase; that is, they are in a highly dispersed form on the surface. The peaks of TiO_2 have been slightly shifted due to solid solution of metal ion with TiO_2. The average particle sizes of the samples were calculated using Debye-Scherrer formula based on the XRD peak broadening analysis at 101 peaks, listed in Table 1. The particle size calculated from XRD data is as large as 9-22 nm for 1, 3, 7, 9 and 11 wt.% Sb-doped TiO_2 and as small as 6 nm for the 5 wt.% Sb-doped TiO_2. This apparent fall in the particle size (higher specific surface area) will ensure high photocatalytic activity for the 5 wt.% Sb-doped TiO_2 when it is used for photocatalytic applications.

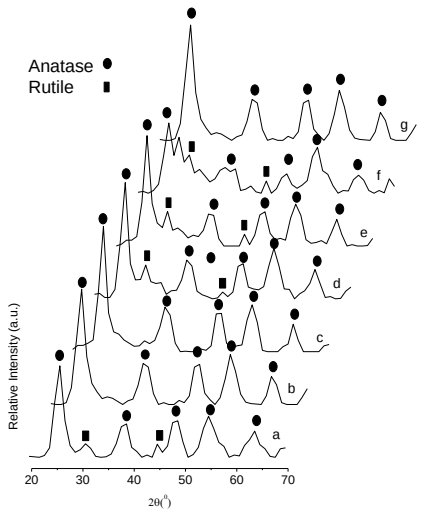

Fig. 1.(a–g) XRD of (a) Pure TiO_2, (b) 1 wt.% Sb/TiO_2, (c) 3 wt.% Sb/TiO_2, (d) 5 wt.% Sb/TiO_2, (e),7 wt.% Sb/TiO_2, (f) 9 wt.% Sb/TiO_2, (g) 11 wt.% Sb/TiO_2.

3.2. TEM and HRTEM analysis

In order to confirm the effect of metal incorporated samples on particle size and hence higher specific surface area of TiO_2 in the composite powders, the particle size of 3, 5 and 7 wt.% Sb-doped TiO_2 samples were observed using TEM.

Fig. 2(a-d) shows TEM and HRTEM images of 3, 5 and 7 wt.% Sb/TiO_2 samples and its corresponding Fourier transfer patterns (FTT) are also presented in the inset of

figures. It can be seen that the particle size of composite samples with 3, 5 and 7 wt.% metal loading are about 6, 8 and 10 nm, respectively. The HRTEM images of samples (Fig. 3(c-d) also represent presence of highly crystalline nanoparticles with mesopores. The fringes appearing in the micrographs allow for the identification of the crystallographic spacing of the doped-TiO_2 nanocrystallites. The fringes most frequently observed correspond to the (101) crystal planes of TiO_2 anatase. The fringes of d = 3.7 Å observed in Fig. 3(c and d) match with (101) crystal planes of anatase TiO_2.

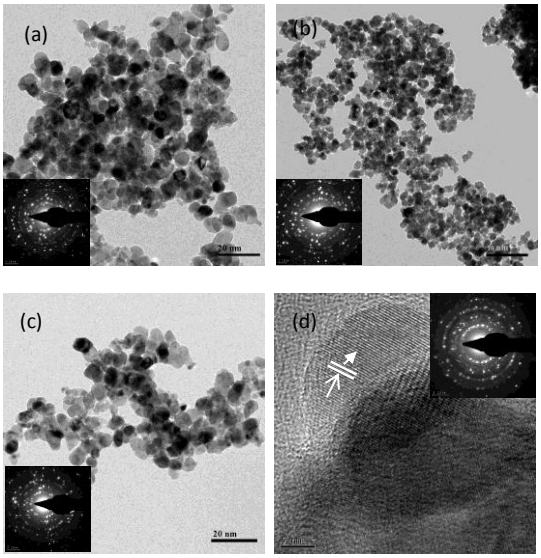

Fig. 2. (a–b) Typical TEM and HRTEM images of the (a) 3 wt% Sb/TiO_2, (b) 5 wt% Sb/TiO_2, (c) 7 wt% Sb/TiO_2.

3.3 BET surface area

All Sb-doped TiO_2 samples exhibit relatively high specific surface areas with respect to the pure TiO_2 (Table 1). The addition of Sb (III) metal ion cause a setback to the crystallization and sintering process, which is evident from the higher surface area of the samples in comparison with the pure TiO_2. [28]. The metal oxide species prevent the agglomeration of TiO_2 particles, resulting in a higher specific surface area. The surface area of the 5 wt.% Sb-doped TiO_2 sample calcined at 400°C is about 535.5 m^2/g. For the other samples, there is no much difference in the surface area.

Table 1. BET surface area, particle size, and surface acidity of synthesized samples

Samples	BET surface area (m^2 g^{-1})	Particle size nm)	Total amount of ammonia desorbed (mmol g^{-1}), 100-600°C	Weight loss (%) of 2,6-DMP
Pure TiO_2	34.00	12.61	0.6270	0.72
1 wt.% Sb/TiO_2	93.00	9.52	0.9521	5.11
3 wt.% Sb/TiO_2	435.7	6.01	0.9032	5.28
5 wt.% Sb/TiO_2	535.5	8.05	0.9362	4.65
7 wt.% Sb/TiO_2	516.0	10.03	0.9437	5.32
9 wt.% Sb/TiO_2	278.0	18.54	1.0029	2.55
11 wt.% Sb/TiO_2	105.0	22.38	0.9362	2.41

3.3 UV–VIS DR spectral analysis

Fig. 3 shows UV–vis diffuse reflectance spectra (DRS) of the Sb/TiO_2 photocatalyst calcined at 400°C. The impact of Sb (III) doping on the band gap of TiO_2 was investigated and a progressive shift in the band gap toward red region is observed.

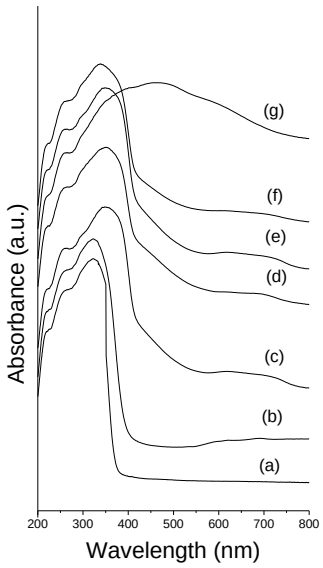

Fig. 3(a–g) UV–VIS-DR spectra of (a) Pure TiO_2, (b) 1 wt.% Sb/TiO_2, (c) 3 wt.% Sb/TiO_2, (d) 5 wt.% Sb/TiO_2, (e),7 wt.% Sb/TiO_2 (f) 9 wt.% Sb/TiO_2 (g) 11 wt.% Sb/TiO_2

The absorption shifts of the samples toward the longer wavelength increases with

increase in the percentage of loaded metal as shown in the Fig. 3(a-g). The calculated band gap of pure TiO_2 is 3.09 eV [29], whereas the band gap is lowered to approximately 2.11 eV after the addition of Sb (III) dopant ions. The Band gap narrowing may be due to the substitution of surface oxygen sites by Sb metal ions on TiO_2 surface [30] or by accumulation of Sb ions on oxygen-deficient sites formed in the grain boundaries [31].

3.4 Thermal analysis

Fig. 4 shows the thermal evolution of 5 wt.% Sb/TiO_2. Several components, such as physically adsorbed water and residual organic materials coming from the synthesis may be removed before the start of the loss of the sulfate and assigned to different steps in the TG curve. Sharp weight losses are observed in two temperature ranges, the first between 50 and 300°C and the second between 350 and 600°C.

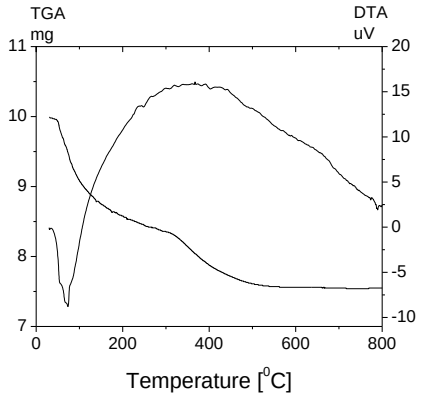

Fig. 4. TG-DTA curve of 5 wt.% Sb-doped TiO_2 sample.

The DTA curve displayed three corresponding valleys for Sb/TiO_2 sample. The first one appeared at about in the temperature region between 50 and 250°C, which is ascribed to water desorption from the samples [32]. The second one emerging at about 400°C could be due to the decomposition of strongly bonded chemical species. The fourth one emerging at about 500°C could be due to the amorphous to anatase transformation of TiO_2 [33].

3.5 FT-IR analysis

The FT-IR spectra of pure TiO_2 and Sb-doped TiO_2 catalysts are shown in Fig. 5(a-g). The FT-IR spectrum of pure TiO_2 shows an absorption band at 1630–1635 cm^{-1}, which is due to the presence of the unassociated H_2O on TiO_2 surface. The broad absorption band at 3800–2500 cm^{-1} reveals a large amount of adsorbed H_2O and surface OH− groups on the TiO_2 surface [34]. A peak appeared at 730 cm^{-1} corresponded to the Ti–O, Ti–O–Ti from titanium dioxide. The Sb-doped TiO_2 samples (Fig. 5(b-g) shows bands in the range 3600–3000 cm^{-1} related to the presence of hydroxyl groups of TiO_2. The absorption band at 1630–1635 cm^{-1}, indicates the presence of the unassociated H_2O on TiO_2 surface. As samples temperature increased the water desorbed and, correspondently, the associated absorptions decreased up to disappear at 400°C. Generally, the bands in the low-wavenumber region (400-600 cm^{-1}) can be assigned to Ti-O bond vibrations. The FT-IR

spectra of the modified samples do not show any band corresponding to the transition metal oxide, which confirms the XRD results.

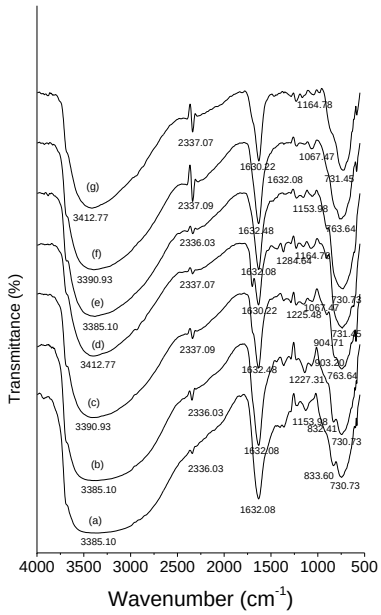

Fig. 5.(a–g) FT-IR spectra of (a) Pure TiO_2, (b) 1 wt.% Sb/TiO_2, (c) 3 wt.% Sb/TiO_2, (d) 5 wt.% Sb/TiO_2, (e),7 wt.% Sb/TiO_2 (f) 9 wt.% Sb/TiO_2 (g) 11 wt.% Sb/TiO_2

3.6 Acidity measurements

NH_3-TPD is used for the evaluation of the surface acidity of the samples. NH_3 desorption peaks were detected between 100 and 600°C, and the total acidity values of the different samples are shown in Table 1. These results indicate that a weak and strong site appears on the surface of these catalysts. Pure TiO_2 shows only low acidity, however, the nature of acid sites is greatly influenced by the amount of the metal incorporated into the lattice and interaction of it with the TiO_2. The TPD study of 2,6- dimethylpyridine was carried out for a comparative evaluation of the Brönsted acidity in the samples [35]. The amount of 2,6- dimethylpyridine desorbed at an appropriate temperature (> 300°C) due to desorption for Brönsted acid sites of samples are also shown in Table 1. The acidity increases in the case of metal incorporated TiO_2, compared to simple TiO_2 [36].

3.7 Photocatalytic activity

The photocatalytic activities of pure TiO_2, and Sb-doped TiO_2 samples are shown in Fig. 6. In the presence of pure TiO_2, decomposition of MB was not observed. However, in the presence of the Sb- doped TiO_2 samples, the decomposition of MB obviously increased. Among the different concentration levels of Sb (1, 3, 5, 7, 9 and 11wt.%) for Sb/TiO_2

system, 5 wt.% Sb-doped TiO_2 sample exhibited the highest photocatalytic activity under solar light irradiation, only 1-1.5 % of MB remained, and in the case of 3 and 7 wt.% of Sb (III) 3-5 % of MB remained after exposure to solar light for 60 min. While as high as 6-8 % remained in the case of 1, 9, and 11 wt.% of Sb (III). From the observed results it was found that the 5 and 7 wt.% Sb-doped TiO_2 are found to be composite photocatalyst, in this case once optical excitation occurs, the photogenerated electrons can be transferred to the lower-lying conduction band Sb (III), while the holes will accumulate in the valence band of TiO_2, and effectively scavenged by the oxidation of MB, whereas the photogenerated electrons can be transferred into the surface of Sb (III), rather than undergoing bulk recombination. Further, 5 and 7 wt.% Sb-doped TiO_2 samples calcined at 400°C temperature presents a higher surface area and anatase phase. Furthermore, the acid properties of the catalyst are still significant. On the other hand, the acidified surface would lead to the formation of oxygen deficiency upon calcination. The presence of surface oxygen deficiencies can act as capture centers for the photoexcited electrons, and effectively restrain the recombination of electrons and holes, while the surface hydroxyl groups acts as centers for the photocatalytic reaction [37].

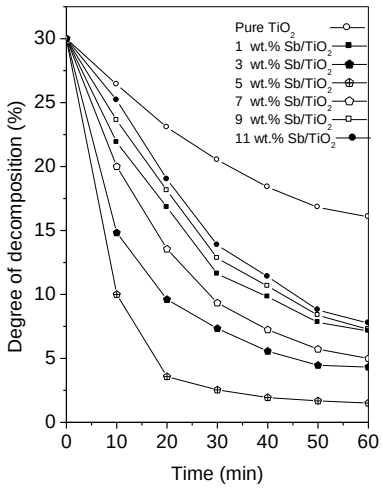

Fig. 6. Rate of decomposition of methyl blue by using (1) pure TiO_2, (2) 1 wt.% Sb/TiO_2, (3) 3 wt.% Sb/TiO_2, (4) 5 wt.% Sb/TiO_2, (5) 7 wt.% Sb/TiO_2,, (6) 9 wt.% Sb/TiO_2, (7) 11 wt.% Sb/TiO_2 calcined at 400°C.

Sb-doped TiO_2 samples shows red-shift in the absorption range compared with pure TiO_2. The existence of oxygen deficiencies, probably located at the anatase-rutile boundary, leads to localized electronic states between the valence and conduction band, shows certain absorption in the visible range. This seems to indicate the absorption could also enhance the efficiency of the photocatalytic reaction since the number of photons participating in the photocatalytic reaction is larger. Furthermore, the higher specific surface area of 5 and 7 wt.% Sb-doped TiO_2 samples implies high adsorption capacity. The conjunction of all this features can lead to the improvement of the photocatalytic efficiency

of the 5 and 7 wt.% Sb-doped TiO_2 composite materials.

Conclusion

Sb-doped TiO_2 nanoparticles were prepared by a sol–gel method. The prepared samples were characterized by XRD, HRTEM, FT-IR, XPS, TGA and UV–VIS DRS. The prepared catalyst showed significant photocatalytic activity toward solar light. The smaller particle size and higher concentration of anatase phase contributed to high photocatalytic activity. The catalyst prepared with 5 wt.% antimony containing TiO_2 showed maximum photocatalytic activity in solar light within one hour. The above findings could be helpful for further development of more efficient titanium dioxide photocatalyst.

References

[1] M. Liu, L.Y. Piao, W.J. Wang, J. Nanosci. Nanotechnol. 10 (2010) p. 7469.
[2] E. Abdelkader, L. Nadjia, B. Ahmed, Appl. Surf. Sci. 258 (2012) p. 5010.
[3] M. Liu, X. Qiu, M. Miyauchi, K. Hashimoto, Chem. Mater. 23 (2011) p. 5282
[4] A.G. Mailer, P.S. Clegg, J. Colloid Interface Sci. 417 (2014) p. 317.
[5] J.A. Rengifo-Herrera, E. Mielczarski, J. Mielczarski, N.C. Castillo, J. Kiwi, C. Pulgarin, Appl. Catal. B-Environ. 84 (2008) p. 448
[6] W. Li, C. Ni, H. Lin, C.P. Huang, S. Ismat Shah, J. Appl. Phys. 96 (2004) p. 6663.
[7] D.A.H. Hanaor, C.C. Sorrell, J. Mater. Sci. 46 (2011) p. 855
[8] F. Wang, L. Feng, D. Zhang, Q. Tang, D. Feng, J. Alloy. Compd. 611 (2014) p. 125.
[9] L. Kernazhitsky, V. Shymanovska, T. Gavrilko, V. Naumov, V. Kshnyakin, T. Khalyavka, J. Solid State Chem. 198 (2013) p. 511.
[10] M.L. Kaariainen, D.C. Cameron, Thin Solid Films 526 (2012) p. 212.
[11] X. Chen, L. Liu, P.Y. Yu, S.S. Mao, Science 331 (2011) p. 746.
[12] S. Munusamy, R.S.L. Aparna, R.G.S.V. Prasad, Sustain. Chem. Process 1:4 (2013) p. 1.
[13] C. Wang, H. Shi, Y. Li, Appl. Surf. Sci. 257 (2011) p. 6873.
[14] S. Gomez, C.L. Marchena, L. Pizzio, L. Pierella, J. Hazard. Mater. 258– 259 (2013) p. 19.
[15] A.N. Ejhieh, M. Amiri, Powder Technol. 235 (2013) p. 279.
[16] F. Li, Y. Jiang, M. Xia, M. Sun, B. Xue, X. Ren, J. Hazard. Mater. 165 (2009) p. 1219.
[17] J. Zhang, S. Tang, L. Liao, W. Yu, J. Li, F. Seland, G.M. Haarberg, J. Power Sources 267 (2014) p. 706.
[18] B. Karthikeyan, L. Natanapatham, S. Senthilvelan, V.L. Chandraboss, M. Murugavelu, Mat. Sci. Semicon. Proc. 16 (2013) p. 23.
[19] E.S. Baeissa, J. Ind. Eng. Chem. 20 (2014) p. 3761.
[20] H.Y. Lin, Y.S. Chang, Int. J. Hydrogen Energ. 39 (2014) p. 3118.
[21] K.J. Kim, P.B. Kreider, C. Choi, C.H. Chang, H.G. Ahn, RSC Adv., 3 (2013) p. 12702.
[22] K. Maeda, ACS Appl. Mater. Interfaces. 6(3) (2014) p. 2167.
[23] C.C. Hu, J.N. Nian, H. Teng, Sol. Energ. Mat. Sol. C. (2008) p. 1071.
[24] J. Wang, Y. Wang, P. Zhang , D. Zhang, X. Ren, J. Alloy Compd. 610 (2014) p. 308.
[25] J. Xua, Q. Li , M.K. Hansen , E. Christensen , A.L.T. Garcı´ , G. Liu, X. Wanga, N.

J. Bjerrum, Int. J. Hydrogen Energ. 37 (2012) p. 18629.

[26] C.C. Pei, W.W.F. Leung, Sep. Purif. Technol. 114 (2013) p. 108.
[27] L. Rizzoa, D. Sanninob, V. Vaianob, O. Saccob, A. Scarpaa, D. Pietrogiacomic, Appl. Catal. B-Environ. 144 (2014) p. 369.
[28] H. Takagi, Y. Fujishiro, M. Awano, J. Mater. Sci. 36 (2001) p. 949.
[29] Y. Lva, L. Yua, H. Huangb, H. Liub, Y. Fengb, J. Alloy. Compd. 488 (2009) p. 314.
[30] R.R. Bhosale, S.R. Pujaria, M.K. Lande, B.R. Arbad, S.B. Pawar, A.B. Gambhire, Appl. Surf. Sci. 261 (2012) p. 835.
[31] T. Ihara, M. Miyoshi, Y. Triyama, O. Marsumato, Appl Catal B 42 (2003) p. 403.
[32] A. Bellifa, L. Pirault-Roy, C. Kappenstein, A. Choukchou-Braham, Bull. Mater. Sci. 37 (2014) p. 669.
[33] C.J. Bodson, S.L. Pirard, R. Pirard, L. Tasseroul, C. Bied, M.W.C. Man, B. Heinrichs, S.D. Lambert, J. Chem. Eng. Mater. Sci. 2 (2014) p. 17.
[34] M.Li, K.N. Hui, K.S. Hui, S.K. Lee, Y.R. Cho, H. Lee, W. Zhou, S. Cho, C.Y.H. Chao, Y. Li, Appl. Catal. B- Environ. 107 (2011) p. 245.
[35] M.V. Dozzi, E. Selli, Catalysts 3 (2013) p. 455.
[36] R.M. de Almeida, F.T.C. Souza, M.A.C. Júnior, N.J.A. Albuquerque, S.P. Meneghetti, M.R. Meneghetti, Catal. Commun., 46 (2014) p. 179.
[37] L. Liu, Y. Li, Aerosol Air Qual Res, 14 (2014) p. 453.

Paper 54

Estimation of Socio-economic Coastal Vulnerability Index for Coastal Villages of Dapoli Tahsil, Ratnagiri District, Maharashtra

Mithilesh Chavan[1], Sunil Gaikwad[2], Tushar Ghorpade[3], Vilas Ugale[4], Dipesh Karmarkar[5]

[1]*Asst. Prof. & Research Scholar, Dept. of Geography, Sir Parashurambhau College, Pune*

[2]*Prof. & Head, Dept. of Geography, Sir Parashurambhau College, Pune*

[3]*Asst. Prof., Dept. of Geography, Waghire College of Arts, Commerce & Science, Pune*

[4]*Associate Prof., Dept. of Geography, Sir Parashurambhau College, Pune*

[5]*Asst. Prof., Dept. of Geography, Smt. Chandibai Himathmal Mansukhani College, Ulhasnagar*

Abstract

Coastal vulnerability assessment is highly useful for identifying areas of coastline that are vulnerable to impacts of climate change, natural hazards and coastal processes. The tropical cyclones in the Arabian Sea striking the Konkan coastal area in recent years have stressed the importance of assessing the vulnerability of coastal areas to such hazards. In the present research work, an attempt has been made to assess the socio-economic coastal vulnerability of the coastal villages of Dapoli Tahsil situated in the northern part of Ratnagiri district. This research work analyses and integrates anthropological variables to assess the socio-economic coastal vulnerability. The population data of 2011 published by Census of India, various reports published by Maharashtra Government, Survey of India toposheets, latest Google Earth images and digital satellite images of IRS LISS-III have been utilized for the computation of various parameters of the socio-economic coastal vulnerability index (SCVI). The five socio-economic and demographic variables analysed are population density, settlements, land use, coastal roads and economic activities. Each of the five socio-economic parameters is ranked for vulnerability into one of the three categories: high (3), moderate (2) or low (1). Once all the coastal villages in Dapoli Tahsil are assigned a risk value for every variable, the SCVI (Socio-economic Coastal Vulnerability Index) is calculated as the square root of the product of the ranked variables divided by the total number of variables. Harnai, Dabhol, Ade, Ladghar, Juikar Mohalla, Pandhari, Burondi, Kelashi, Anjarla, Saldure and Murud villages were classified as highly vulnerable according to the calculated SCVI. The exercise of socio-economic coastal vulnerability assessment is very crucial for the prioritization of coastal villages for disaster management and mitigation.

Key words: socio-economic coastal vulnerability index (SCVI), population density, settlements, land use.

Introduction

Coastal environments are under increasing pressure from both predicted consequences of climatic change such as sea level rise and rapid anthropogenic development. Coastal erosion and inundation pose a threat to human populations, activities and infrastructure, especially within the context of a changing climate and increasing coastal populations. The interplay of both natural

and anthropogenic factors has contributed to and compounded problems such as erosion, pollution, salt water intrusion, flooding, deterioration and loss of natural habitats, etc.

Study Area

Dapoli Tahsil is situated in the northern part of Ratnagiri district. The study area is bounded by the Bharja River in the north and Vashishthi River in the south, which are debouching into the Arabian Sea in the west. The study area is a part of the low-lying Konkan coastal strip. The study area comes in the tropical climatic region with hot and humid climate. Heavy rainfall results in highly eroded landscape in the coastal region. The drainage network is dense, well developed and dendritic pattern. The study area is classified as agro ecological region of Western Ghats and Coastal Plains Ecoregion and the forest type is tropical moist deciduous forest. The tropical cyclones in the Arabian Sea viz. Tauktae (2021) and Nisarga (2020) striking the Konkan coast especially of Ratnagiri District have stressed the importance of assessing the vulnerability of coastal areas to flooding and inundation. The coastline of Dapoli Tahsil, which has number of beaches, sites of importance to tourism, tourist resorts, hotels, fishing villages, ports and towns, has experienced threat from many disasters such as cyclone, flood and erosion.

Figure 1: Location of the Study Area

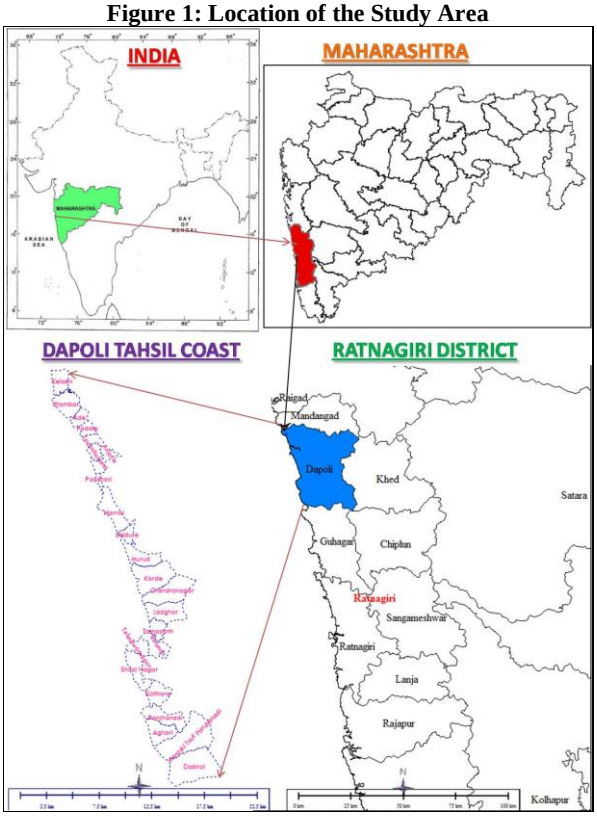

Source: Author

Objectives

Specific objectives of the present research work are as follows:

1. To estimate the socio-economic coastal vulnerability index for the coastal villages along the coast of Dapoli Tahsil using multi-criteria analysis.

2. To identify highly vulnerable coastal villages based on socio-economic parameters.

Data and Methodology

The Census of India data of 2011, various reports published by Maharashtra Government, Survey of India (S.O.I.) topographical maps, recent Google Earth images and digital satellite images of IRS LISS-III have been utilized for the computation of various parameters of the socio-economic coastal vulnerability index (SCVI). The coastal vulnerability assessment model provides an estimate of exposure of coastal areas to erosion and inundation in terms of a vulnerability index, which is useful to differentiate areas having relatively high or relatively low exposure. The original Coastal Vulnerability Index (CVI) is expressed as square root of the product of the weighted variables and divided by the total number of variables (Cornitz et al. 1997).

$$CVI = \sqrt{(a * b * c * d * e * f / 6)} \quad \text{… Equation 1}$$

Where,

'a' refers geomorphology of the coastal area;

'b' is shoreline erosion/accretion rate (m/yr);

'c' is coastal slope (%);

'd' is mean sea level rise rate (mm/yr);

'e' is mean wave height (m); and

'f' is mean tidal range (m).

In this research work, only the socio-economic variables have been considered separately for the estimation of the socio-economic coastal vulnerability index. The socio-economic coastal vulnerability index is equally important when compared with the physical coastal vulnerability index. The socio-economic coastal vulnerability index (SCVI) is calculated by using five socio-economic and demographic variables. The five socio-economic and demographic variables analysed are population density, settlements, land use, coastal roads and economic activities. Population density was calculated with the help of Census of India data for Ratnagiri District. The settlements, land use and coastal roads were identified from S.O.I. topographical maps, recent Google Earth images and Land Use Land Cover map prepared by the classification of digital satellite images of IRS LISS-III in QGIS 3.20 software. The data about economic activities in the coastal villages were acquired from the Census of India reports of 2011 and various socio-economic reports published by Maharashtra Government. Each of the five socio-

economic parameters is ranked for vulnerability into one of the three categories: high (3), moderate (2) or low (1). High risk values were assigned for coastal villages having very high density of population, closely spaced settlements, intensive land use, presence of coastal roads and tourism activity. Low risk values were assigned for coastal villages having low density of population, few or no settlements near the coast, barren lands or rocky areas, absence of coastal roads and no major economic activities. After each coastal village is assigned a risk value based on each socio-economic variable, the Socio-economic Coastal Vulnerability Index (SCVI) is calculated as the square root of the geometric mean of the ranked variables as follows:

$$SCVI = \sqrt{(g * h * i * j * k / 5)} \quad \text{… Equation 2}$$

Where,

'g' is population density per sq. km

'h' is settlements

'i' is land use

'j' is roads

'k' is economic activities

The coastal villages are classified as highly vulnerable, moderately vulnerable and least vulnerable according to the calculated socio-economic coastal vulnerability index. The final map showing the classification of coastal villages based on the calculated socio-economic coastal vulnerability index has been prepared in QGIS 3.20 software.

Results and Discussion

Population density:

For estimation of the exposure of coastlines to coastal hazards, it is important to consider the population of humans which will be subjected to those coastal hazards. In the present study, the population has been considered as exerting pressure on the coastal environment and resources and hence coastal villages having higher concentration of population were considered as more vulnerable to coastal hazards. Coastal villages which are densely populated are generally regarded as highly vulnerable, as there is a relatively higher risk and damage when a disaster occurs. Population data for each coastal village of Dapoli Tahsil were gathered from the Indian Census 2011 – Ratnagiri District Handbook for the year 2011. For the risk ranking, the coastal villages with the highest population density were considered as the most vulnerable. Pandhari has the highest population density among all the coastal villages of Dapoli Tahsil. The population density of Pandhari is 10,194 persons per square kilometre land area, which is extremely high. Pandhari is also the third most populated coastal village of Dapoli Tahsil having a total population of 5780 in 2011.The population density of four coastal villages - Harnai, Burondi, Kelshi and Ade is more than 1100 persons per square kilometre land area, which is very high. Harnai is situated very closely to the south of densely populated Pandhari. The population density of Harnai is 1229 persons per square kilometre land area. Harnai has the highest population (7274) among all the coastal villages of Dapoli Tahsil. The coastal village of Burondi

in the central part along the coast of Dapoli Tahsil has a very high population density of 1201 persons per square kilometre land area. Kelshi village in the extreme north of Dapoli Tahsil and Ade village in the northern part of Dapoli Tahsil have very high population density (1186 and 1176 persons per square kilometre land area respectively). Adjoining to Pandhari is Juikar Mohalla village situated along the south bank of river near its mouth is having 810 persons per square kilometre land area which is categorised as high density of population. The Census Town of Dabhol situated along the north bank of Vashishthi River near its mouth is also categorised as coastal area having high density of population as this area has 786 persons per square kilometre land area. Dabhol has the second highest population (7038) among all the coastal villages / census towns of Dapoli Tahsil. The coastal village of Murud which is a popular tourist place has moderately high density of population (394 persons per square kilometre land area). The coastal villages of Tamastirth, Panchanadi, Kolthare, Ladghar, Anjarla, Padale and Saldure have moderate density of population ranging from 200 to 300 persons per square kilometre land area. Teleshwarnagar, Utambar, Tadachakond, Chandranagar, Karde, Vanoshi Tarf Panchanadi and Shital Nagar villages have a comparatively low density of population (less than 200 persons per square kilometre land area). Shital Nagar has the lowest population density among all the coastal villages of Dapoli Tahsil. The population density of Shital Nagar is only 86 persons per square kilometre land area, which is very low.

Table 1: Population Density of Coastal Villages of Dapoli Tahsil

Sr. No.	Village Name	Area of Village (sq.km)	Total Population	Population Density (persons per sq.km)
1	Kelashi	2.6516	3145	1186
2	Utambar	4.2092	788	187
3	Ade	1.4597	1718	1176
4	Padale	1.5084	355	235
5	Anjarla	5.58	1394	249
6	Tadachakond	1.657	269	162
7	Juikar Mohalla	1.786	1447	810
8	Pandhari	0.567	5780	10194
9	Harnai	5.9143	7274	1229
10	Saldure	1.6298	356	218
11	Murud	4.2092	1662	394
12	Karde	7.802	1097	140
13	Chandranagar	7.42	1084	146
14	Ladghar	5.58	1398	250
15	Tamastirth	2.14	641	299
16	Burondi	3.3	3966	1201
17	Teleshwarnagar	2.2661	453	199
18	Shital Nagar	4.07	354	86
19	Kolthare	3.7358	1007	270
20	Panchanadi	4.6868	1361	290
21	Aghari	4.6868	501	106
22	Vanoshi Tarf Panchanadi	12.02	1684	140
23	Dabhol	8.95	7038	786

Source: Ratnagiri District Census Handbook, 2011 and Population Density Calculation: Author.

Settlements:

The coastal villages having very few settlements or no settlements near the coast have been assigned low risk rating. These villages are Utambar, Tadachakond, Chandranagar, Teleshwarnagar, Shital Nagar, Aghari and Vanoshi Tarf Panchanadi. The coastal villages having numerous closely spaced settlements near the coast have been assigned moderate risk rating. These villages are Kelashi, Padale, Anjarla, Murud, Saldure, Karde, Ladghar, Tamastirth, Kolthare and Panchanadi. The coastal villages having very closely spaced compact settlements near the coast have been assigned high risk rating. These villages are Ade, Juikar Mohalla, Pandhari, Harnai, Burondi and Dabhol.

Land Use:

Land use type is of great significance in determining the socio-economic coastal vulnerability. Bare rocks, barren land or sparsely vegetated areas have been considered to exhibit low vulnerability naturally. These coastal villages are Utambar and Tadachakond in the northern part of the Tahsil; Chandranagar in the central part; and Teleshwarnagar, Shital Nagar, Aghari and Vanoshi Tarf Panchanadi in the southern part of the Tahsil. Agricultural areas and settlements with *Wadis* are considered to have moderate vulnerability. These coastal villages are, Kelashi, Ade, Padale, Anjarla, Murud, Saldure and Karde in the northern coastal region of Dapoli; Ladghar and Tamastirth in the central coastal region and; Kolthare and Panchanadi in the southern coastal region of Dapoli. Clustered or compact settlements, urban places and industrial areas have been considered as having relatively high vulnerability. These coastal villages are Juikar Mohalla, Pandhari, Harnai, Burondi and Dabhol.

Coastal Roads:

The coastal villages having no roads along the coast have been assigned low risk rating. The villages having roads of local importance along the coast have been assigned moderate risk rating. The coastal villages through which state highways are passing along the coast have been assigned high risk rating. These villages are Harnai, Saldure and Ladghar. The Maharashtra State Highway number 4 passes very closely from the coast of these villages.

Economic Activities:

In the coastal villages of Utambar, Tadachakond, Juikar Mohalla, Pandhari, Chandranagar, Teleshwarnagar, Shital Nagar, Panchanadi, Aghari and Vanoshi Tarf Panchanadi, major economic activities are not observed. Hence, these coastal villages have been assigned low risk rating. The coastal villages such as Kelashi, Ade, Padale, Saldure, Burondi and Dabhol where economic activities such as agriculture and tourism are observed to a limited extent, have been assigned moderate risk rating. The coastal villages in which tourism is the dominant economic activity have been assigned high risk rating. These villages are Anjarla, Harnai, Murud and

Karde along the northern coast of Dapoli Tahsil; Ladghar and Tamastirth along the central coast of Dapoli Tahsil and Kolthare along the southern coast of Dapoli Tahsil.

Table 2: SCVI (Socio-economic Coastal Vulnerability) of Coastal Villages of Dapoli Tahsil

Sr. No.	Village Name	Population Density	Settlements	Land Use	Coastal Roads	Economic Activities	SCVI	SCV
1	Kelashi	3	2	2	2	2	3.10	High
2	Utambar	1	1	1	2	1	0.63	Low
3	Ade	3	3	2	2	2	3.79	High
4	Padale	2	2	2	2	2	2.53	Mod.
5	Anjarla	2	2	2	2	3	3.10	High
6	Tadachakond	1	1	1	1	1	0.45	Low
7	Juikar Mohalla	3	3	3	2	1	3.29	High
8	Pandhari	3	3	3	2	1	3.29	High
9	Harnai	3	3	3	3	3	6.97	High
10	Saldure	2	2	2	3	2	3.10	High
11	Murud	2	2	2	2	3	3.10	High
12	Karde	1	2	2	2	3	2.19	Mod.
13	Chandranagar	1	1	1	2	1	0.63	Low
14	Ladghar	2	2	2	3	3	3.79	High
15	Tamastirth	2	2	2	1	3	2.19	Mod.
16	Burondi	3	3	3	2	1	3.29	High
17	Teleshwarnagar	1	1	1	1	1	0.45	Low
18	Shital Nagar	1	1	1	1	1	0.45	Low
19	Kolthare	2	2	2	1	3	2.19	Mod.
20	Panchanadi	2	2	2	1	1	1.26	Mod.
21	Aghari	1	1	1	1	1	0.45	Low
22	Vanoshi Tarf Panchanadi	1	1	1	1	1	0.45	Low
23	Dabhol	3	3	3	2	2	4.65	High

Source: Author

Figure 2: Classification of Coastal Villages of Dapoli Tahsil by SCVI (Socio-economic Coastal Vulnerability)

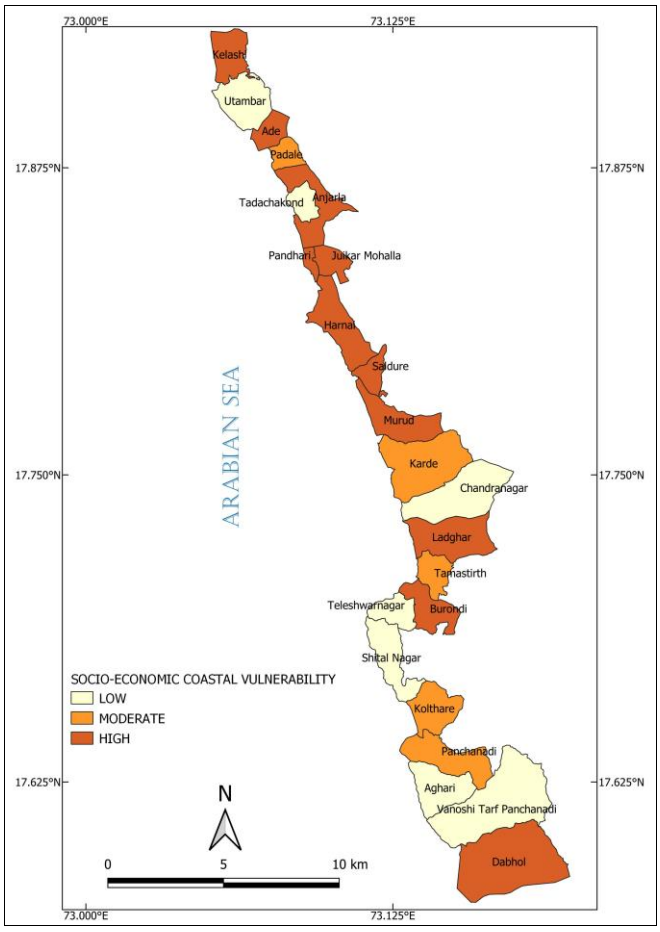

Source: Author

Conclusion

The results revealed the highly vulnerable coastal locations with high SCVI (index value more than 3), moderately vulnerable locations (index value between 1 and 3) and least vulnerable coastal locations with low SCVI (index value less than 1). Harnai, Dabhol, Ade, Ladghar, Juikar Mohalla, Pandhari, Burondi, Kelashi, Anjarla, Saldure and Murud villages were classified as highly vulnerable according to the calculated SCVI. Harnai has the highest SCVI value of 6.97 followed by Dabhol Census Town (4.65). Padale, Karde, Tamastirth, Kolthare and Panchanadi

villages were classified as moderately vulnerable according to the calculated SCVI. Utambar, Chandranagar, Tadachakond, Teleshwarnagar, Shital Nagar, Aghari and Vanoshi Tarf Panchanadi were classified as least vulnerable according to the calculated SCVI. The exercise of socio-economic coastal vulnerability assessment along with the physical coastal vulnerability assessment is very crucial for the prioritization of coastal villages. Coastal vulnerability assessment on the basis of biophysical parameters only will not give the comprehensive condition of coastal vulnerability. The coastal vulnerability map prepared for the coastal villages along Kelshi-Dabhol coastal stretch of Dapoli Tahsil can be used by the local administration for proper decision making in times of disaster mitigation and management as well as it can be used for coastal zone management.

References

[1] Cutter, S.L., Boruff, B.J., Shirley, W.L., 2003. Social vulnerability to environmental hazards. Social Science Quarterly 84, 242-261.

[2] Census of India. 2011. District Census Handbook: Ratnagiri – Village and Town Directory. Series-28. Part XII-A. Directorate of Census Operations, Maharashtra.

[3] Census of India. 2011. District Census Handbook: Ratnagiri – Village and Town wise Primary Census Abstract. Series-28. Part XII-A. Directorate of Census Operations, Maharashtra.

[4] Duriyapong, F., Nakhapakorn, K., 2011. Coastal vulnerability assessment: a case study of Samut Sakhon coastal zone. Songklanakarin J. Sci. Technol. 33, 469-476.

[5] Dwarakish, G.S., Vinay, S.A., Dinakar, S.M., Pai, J.B., Mahaganesha, K., Natesan, U., 2008. Integrated coastal zone management plan for Udupi coast using remote sensing, geographical information system and global position system. Journal of Applied Remote Sensing 2.

[6] Gornitz, V.M., Beaty, T.W., Daniels, R.C., 1997. A coastal hazard database for the U.S. West Coast. Oak Ridge National Laboratory, Oak Ridge, Tennessee, p. 162 pages.

[7] Gornitz, V.M., Daniels, R.C., White, T.W., Birdwell, K.R., 1994. The development of a coastal risk assessment database: Vulnerability to sea-level rise in the U.S. southeast. Journal of Coastal Research Special Issue No. 12, 327-338.

[8] Government of Maharashtra (2010). Marine fisheries census 2010. Central marine fisheries research institute, part-II, Cochin, India.

[9] Kumar, A.A., Kunte, P.D., 2012. Coastal vulnerability assessment for Chennai, east coast of India using geospatial techniques. Natural Hazards 64, 853-872.

[10] Kumar, T.S., Mahendra, R.S., Nayak, S., Radhakrishnan, K., Sahu, K.C., 2010. Coastal Vulnerability Assessment for Orissa State, East Coast of India. Journal of Coastal Research 26, 523-534.

[11] Maharashtra Tourism Development Corporation. 2015. Tourism Survey for the State of Maharashtra, Final Report, Mumbai, India.

[12] Maharashtra Tourism Development Corporation. 2019. Tourism Survey for the State of Maharashtra, Final Report, Mumbai, India.

[13] McLaughlin, S., McKenna, J., Cooper, J.A.G., 2002. Socio-economic data in coastal vulnerability indices: constraints and opportunities. Journal of Coastal Research Special Issue 36, 487-497.

[14] Tragaki, A., Gallousi, C., and Karymbalis, E., 2018. Coastal Hazard Vulnerability Assessment Based on Geomorphic, Oceanographic and Demographic Parameters: The Case of the Peloponnese (Southern Greece). Land 2018, 7, 56, 1-16.

Paper 55

Bio-Inspired Heteroatom Doped Engineering of Graphene Nanomaterial for its Adsorption and Absorbing Performance with Facile Recycling

Commented [AMD4R3]:

U.D.Patil[1,3], D.M. Nerkar[2],Neetu Paliwal[3]

[1]Department of Physics, Annasaheb Awate College, Manchar, Tal: Ambegaon Dist.: Pune , Maharashtra, India.

[2]Department of Physics, Sathaye College, Vile Parle (E), Mumbai Maharashtra, India.

[3]Department of Physical Sciences, Rabindranath Tagore University Bhopal, India.

Abstract

The current study intends to manufacture a sulphur and nitrogen codoped reduced graphene oxide (SN-rGO) nanomaterial utilizing an easy, ecological technique, and to use it to the spectroscopic detection of heavy metal ions such as mercury (Hg^{2+}) and chromium-VI [Cr(VI)] in drinkable water. Initially, GO sheets were incorporated with S and N heteroatoms and were produced in an environmentally friendly manner utilizing Slaughterhouse waste extract as a green reducing agent. The SN-rGO nanomaterial was then investigated for their functional chemical bonding, surface morphology,, chemical structure, and elemental compositions using Fourier transform Infrared spectroscopy (FTIR), Scanning electron microscope (SEM), Energy dispersive X-ray spectroscopy (EDX), and Ultraviolet Visible spectroscopy (UV-Vis) sensing. Notably, the findings of this investigation revealed that the SN-rGO nanomaterial demonstrated a plethora of astounding properties in terms of analyte sensing. In a nutshell, UV-visible and Fourier transform infrared (FTIR) spectroscopies verified the effective synthesis of SN-rGO nanomaterial. The wrinkled, folded, and cross-linked network architectures in the SEM images verified the surface modification and sulphur and nitrogen doping in the rGO sheet, as well as the synthesis of SN-rGO. The elemental composition of the SN-rGO nanomaterial was verified using EDX. Finally, the SN-rGO probe has a lower detection limit for Hg^{2+} and Cr (VI) of 15 µM and 25 nM, respectively, due to its greater surface area, porous nature, and high carrier mobility. In summary, our findings show that SN-rGO nanomaterials have a high sensitivity to Hg^{2+} and Cr (VI) in potable water, implying that they can help with environmental cleanup.

1. Introduction

As a result of remarkable characteristics, carbon compounds, in particular, graphene, have attracted researchers in a wide range of areas during the past few years [1]–[3]. It may be owing to its large surface area relative to other allotropes of carbon, as well as the fact that it may be utilized to create materials in many dimensions, such as 1D nanostructures, 2D layer stacked films, 3D graphene hydrogel, and aerogel, etc[4], [5]. There is a constant effort by scientists to enhance graphene in some way. In order to do this, scientists use graphite that has been oxidized to create graphene oxide (GO) [6], [7]. Defects created due to different oxygen groups available in GO can be used in various applications. GO undergoes further development, resulting in the production of reduced GO (rGO) [7]–[10]. This has led to the development of numerous rGO techniques that have certain drawbacks, such as affecting graphene's original electrical characteristics. Ion doping has been demonstrated in several published studies, regardless probability of clusters in nanocomposites. In addition, the employment of chemical reducing agents for the fabrication of rGO is dangerous, perhaps flammable, and extremely harmful to human health and the environment. As a result, the usage of such hazardous chemical agents must be avoided. Numerous biomaterials, phytochemicals, and microorganisms have been described as eco-friendly green reducing agents for rGO's encapsulation and reduction agent [11]. Researches have come up with several innovative techniques that include amino acids, vitamins, and glucose for the reduction of GO [12], [13]. It implies that the increased interest in green chemistry and ecologically friendly GO synthesis might lead to the development of numerous novel techniques towards reducing GOs as great alternatives to existing chemical procedures.

To improve the performance of graphene-based devices for a wide variety of applications, heteroatom doping of graphene has emerged as a promising study area [14]–[19]. Chemical doping allows for the tailoring of graphene's electrical characteristics, revealing a plethora of possible features that may enhance photocatalysis [20]–[24]. Although the lack of an inherent bandgap severely limits the applications of graphene in fields such as nanoelectronics, electrocatalysis, and energy storage, it is appealing to generate a bandgap from graphene in order to advance the aforementioned applications. Doping agents in substitutional doping can disrupt the sp^2 carbon network and cause the development of sp^3 defect areas via covalent interaction with graphene [20]. Doping with heteroatoms, for instance, opens up wider opportunities for altering the structural and electrical characteristics of graphene [25], [26]. Heteroatom doping induces polarisation in the sp2 hybridized network, which opens a band gap at the Dirac point by reducing the adjacent density of states and confers semiconducting

characteristics to graphene [16], [17], [25], [27]. Furthermore, the altered local electronic structures significantly improve the carbon matrix's binding affinity. In light of these concerns, heteroatom doping of graphene materials presents an interesting and potential emerging research field for the invention of next-generation durable adsorbents and photocatalysts for bioremediation [28], [29].

As we all know, the quantity of heavy metals naturally present in the environment is within a typical range. Regrettably, the proportion of heavy metals in nature is quickly increasing due to expansion in a wide variety of industries. It might be as a result of different industrial and deliquescing processes. Furthermore, outdated infrastructural water supplies, pollution from automobiles, contaminated paint, various pesticides, polymers, and so on, all lead to the rise in heavy metals concentrations [30]. It is important to note that the majority of industrialized and developing countries are dealing with heavy metal contamination [31]. It has now become a serious issue. However, we are currently experiencing quality water shortages as a result of water pollution. In this context, numerous contaminants, particularly heavy metals, are hazardous to both humans and the environment. It has a significant impact on the quality of naturally accessible water. Consequently, the presence of such heavy metals causes a variety of health problems, including gastrointestinal ailments, muscle diseases, cancers, reproductive diseases, neurodegenerative disorders, chromosomal abnormalities, etc [30]. As a result, detecting and separating heavy metal levels in drinkable water is necessary. Several research organizations are working on the identification and isolation of these kinds of water pollutants. Nonetheless, the majority of methods face challenges such as sensitivity and selectivity. Furthermore, the chemically produced materials for detecting pollutants have restricted applicability due to the usage of hazardous chemicals in the creation of such nanomaterials.

Initially, we have fabricated SN-rGO by incorporating heteroatoms and concurrently reducing GO sheets in a single step using Slaughter House Waste (SHW) extract as a green reducing agent. Finally, employing a stable SN-rGO nanomaterial, the spectroscopic detection of heavy metal ions in drinkable water was studied. As a consequence, the SN-rGO nanomaterial spectroscopic sensing of Hg^{2+} and Cr (VI) ions in potable water demonstrated an excellent potential to sense these heavy metal ions reliably. Taken as a whole, SN-rGO might be an easy, hasty, and low-cost technique for detecting heavy metals in water. Our current study may inspire future SN-rGO-based applications to remove Hg^{2+} and Cr (VI) ions from drinkable water.

2. Experimental Section

2.1. Materials

Graphite powder (Asbury carbon, New Jersey, USA.), Conc. Sulphuric acid (Merck specialities Pvt. Ltd. Mumbai, India), Potassium permanganate (Loba Chemie. Chemicals. Pvt. Ltd. Mumbai, India), Hydrogen peroxide (RFCL Limited, Mumbai, India), Hydrochloric acid (Merck specialities Pvt. Ltd. Mumbai, India.), Bone meal powder (Local Slaughter House Shirpur, Maharashtra, India). All additional chemicals and reagents were of analytical quality and used exactly as received.

2.2. Preparation of GO

GO was prepared according to an improved Hummers method by oxidation of natural graphite powder [1]. Under continuous stirring in an ice bath, 3.0 g of accurately weighed graphite powder was mixed with 70 mL concentrated H_2SO_4. When homogenization was obtained 9.0 g $KMnO_4$ were applied at a slow pace retaining the cold temperature below 5°C for a time of 30 min. It formed a pasty mass and transferred the reaction mixture to the 40℃ water bath and stirred them intensely for about 15 minutes. The deionized water 150 mL was then applied and the solutions were stirred at 95° C for 15 minutes. Afterward, 500 mL of water has been added, followed by a steadily added 5 ml H_2O_2 (30%) whereby it turns the solution from yellow to dark brown. To extract metal ions, the mixture was purified and washed with 10% HCl and water in triplicate. Drying of the resulting solids was carried out in air or an oven at 35°C.

2.3. Preparation of Codoped SN-rGO using SHW

SHW rinsed with deionized water and sterilized under ultraviolet light for 15 min. to decontaminate thoroughly the bone meal powder. The powder (10 gm) were taken in round-bottom flasks (RBF) with (60 ml) distilled water and reflux for 1 hr. The extract was then filtered through Whatman filter paper to remove insoluble fractions and macromolecules. The obtained concentrated filtrate was used for further phytochemical testing and the nanocomposite synthesis process. The SN-rGO were fabricated by adding 30 ml of BME in 250 ml of 2 neck RBF containing previously sonicated 60ml of (1mg/ml) GO dispersion. The RBF is then placed in the heating mantle for 6 hrs at 90℃. A thermometer pocket is inserted to maintain the constant temperature throughout the reaction. After completion of the

reaction, the mixture is then filtered by in vacuum filter by Millipore filter paper. The residue was then washed with distilled water and dried in the oven at 60℃[3].

2.4. Characterization of SN-rGO nanomaterial

Various spectroscopic methods were used to characterize the fabricated GO and SN-rGO nanomaterials. Firstly, the UV-visible spectroscopy of GO and SN-rGO were acquired within 800-400 nm with a quartz cuvette on a Shimadzu UV 1800 spectrophotometer (Japan). An IR spectrophotometer (DRS 8000 IR spectrophotometer Shimadzu 8400s, Japan) was used to scan the functional groups of GO and SN-rGO nanomaterials throughout a wave range of 4000-400 cm^{-1}. The morphology and elemental analyses of GO and SN-rGO nanomaterials were studied using a scanning electron microscope (SEM) with a 15 kV acceleration voltage and interpreted using a Bruker, 1530-2 FESEM/EDX, Germany. Material geometry and thickness were examined via a High-Resolution Transmission Electron Microscope (HR-TEM, Jeol/JEM 2100) with a 200 kV LaB6 light source.

2.5. Spectroscopic sensing of heavy metal ions by SN-rGO nanomaterial

Sensing of Hg^{2+} by SN-rGO nanomaterial

By adding various quantities of Hg^{2+}, the absorption spectra of the SN-rGO nanomaterial were recorded. In summary, several concentrations of $HgCl_2$ were made for testing (10 μM, 15 μM, 50 μM, 100 μM, 250 μM, 500 μM). Then, 1 mL of this solution was added to 2 mL of SN-rGO nanomaterial solution, and after shaking the mixture was allowed to settle for 2 minutes. Absorption spectra from 800 nm to 200 nm were recorded to track changes in the SN-rGO nanomaterial absorbance band when different doses of Hg^{2+} were added. To detect the varying Hg^{2+} concentrations, they were introduced individually into the SN-rGO nanomaterial solution, mixed, and then allowed to rest. Furthermore, utilizing SN-rGO nanomaterial, real-time Hg^{2+} detection was accomplished in a spiked sample. In this study, 75 μM Hg^{2+} was introduced to vials holding 2mL of SN-rGO nanomaterial. The intensity of the color changes in containers were seen with the naked eye proceeded by a recording of UV-Vis optical absorption from 800-200 nm.

Sensing of Cr (VI) by SN-rGO nanomaterial

Cr (VI) was detected utilizing the UV visible spectroscopic technique with the SN-rGO nanomaterial. To begin, a 1 mM $K_2Cr_2O_7$ stock solution was made in DDW. In the meantime, a DDW solution of SN-rGO nanomaterial (1 mg/mL) was produced. In separate vials, 1 mL

of 10 nM, 25 nM, 50 nM, 250 nM, 500 nM, 2500 nM, 5×10^3 nM, 75×10^2 nM, and 1×10^4 nM were added. After that, 2 mL of the SN-rGO nanomaterial solution was added to the vials that had already been prepared. The SN-rGO nanomaterial was used to detect Cr (VI) in a spiked sample in real-time. Latterly, 50 nM Cr (VI) was introduced to vials holding 2 mL of SN-rGO nanomaterial. The color changes in the solution were noticed by recoding UV-Vis absorption spectra from 800 - 200 nm.

3. Results and Discussion

The presence of proteins, amino acids, and other phytoconstituents was revealed during the phytoconstituents screening of SHW extract[32]. The inclusion of phytoconstituents allows for the green ecofriendly synthesis of SN-rGO nanomaterial [33].

3.1. UV Spectroscopy Analysis

Figure 1 shows the UV absorption spectra of GO and SN-rGO nanomaterial. Although to graphite oxidation, the polarity of the graphene layer and its solubility in water are frequently enhanced. This is caused by the bonding of oxygen to the graphene layers. The produced GO should have a maximum absorbance at around 220-270 nm for a thoroughly oxidized material. According to the literature [34]–[36], most heteroatom doped graphene solutions have a displaced absorption peak, indicating that GO reduction has occurred. This phenomenon may be explained by the shift in absorbance crest from 226 nm to 264 nm (as seen in Fig.1) caused by oxygen containing groups removal from the graphene lattice. The absorbance band attributed to oxidized graphene at around 320 nm shifts higher with the reduction of GO. This change is caused by connected oxygen on the sheets being desorbed by the reducing agent [35], decreased oxygen - containing groups, and a rise in aromatic rings, which ensue in electrons getting excited at a lower energy [34]. It also represents electrical conjugation inside rGO sheets, which is reactivated when GO is reduced [36]. In addition, the GO dispersion showed a strong absorption peak at 226 nm (λ_{max}) owing to π-π* transitions of an aromatic ring comprising C-C bonds and a marginally lower intensity subsequent crest at 300 nm attributed to graphene, n-π transitions of C-O bonds, respectively. It validated the synthesis of GO and SN-rGO on the basis of this.

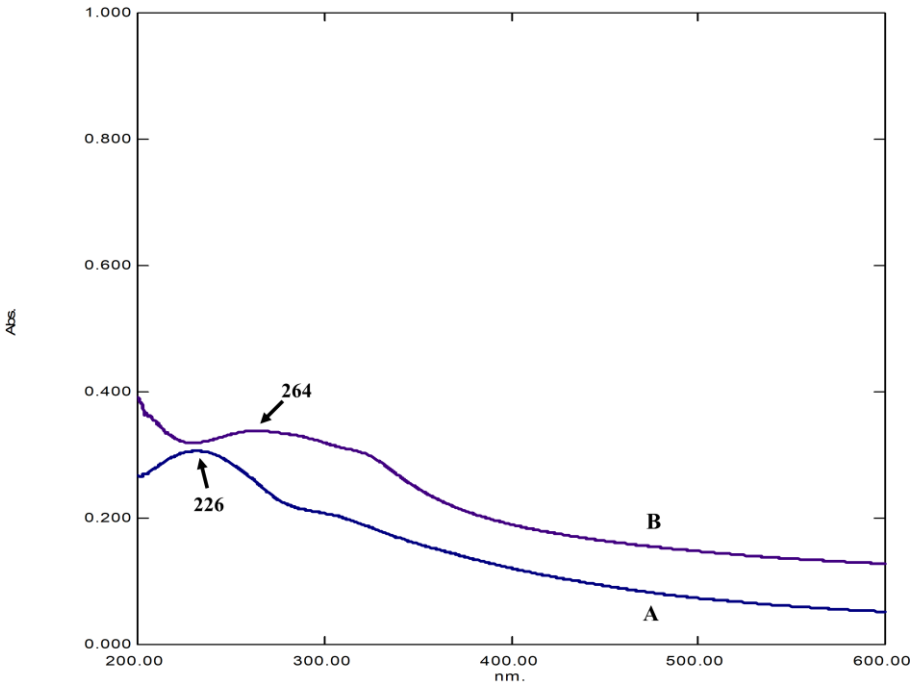

Figure 1 UV visible spectra of (a) GO and (b) SN-rGO

3.2. Fourier transform infrared (FTIR) spectroscopy

The FTIR of synthesized GO and SN-rGO samples were recorded in the range 400 - 4000 cm^{-1} as shown in figure 2. The existence of characteristics of oxygen containing groups like hydroxyl and carboxyl group is evident from spectra of GO. The prominent peaks observed in FTIR spectra are and its spectral assignment were analysed. The notable peaks at 1070, 1250 and 1750cm^{-1} were attributed to C-O stretching, C-O-C stretching and C=O carbonyl stretching [37]. The major peaks in the FTIR responses of both the samples are similar. The peak at 1042cm^{-1} shown by the SN-rGO sample is arises due to SO_4 group [37].The band between 620 to 650 cm^{-1} is ascribed to existence of N in the sample of SN-rGO [37].The occurrence of prominent broad peak at 3619cm^{-1} can be related to presence of water adsorbed [38].

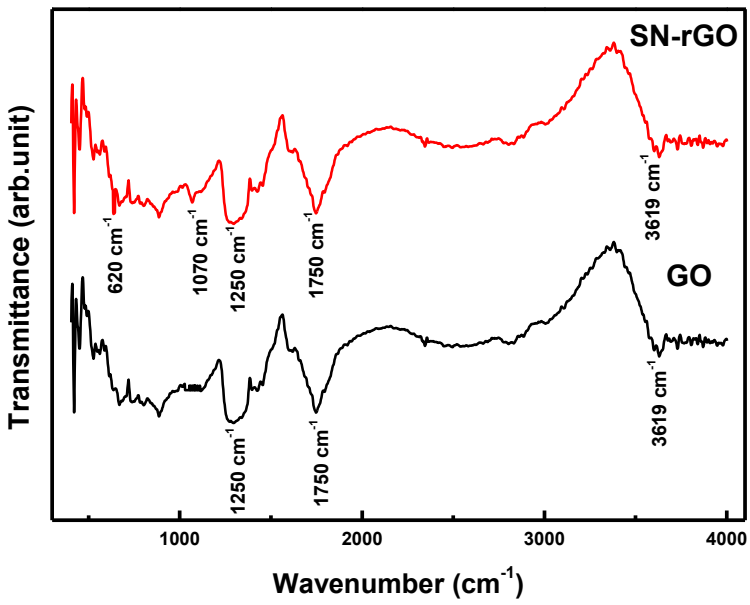

Figure 2 Fourier transform Infrared spectroscopy analysis (FTIR) analysis of the Graphene Oxide (GO) and Sulphur,Nitrogen Codoped Reduced Graphene Oxide (SN-rGO)

3.3. Scanning electron microscopy (SEM) analysis

Figure 3 illustrates the structure and shape of the GO and SN-rGO nanosheets. Figure 3 illustrates the structure and shape of the GO and SN-rGO nanosheets. The typical SEM picture of segregate GO nanosheets is given in Fig. 3 (a,b). Graphite oxide was produced by a few layers of GO after oxidation, as seen in Fig. 3. (a). The picture of the produced GO displayed thin and crumpled nanosheets that might concede electron beam passage [34]. Crumple and ripple patterns were also featured in the GO nanosheets, as described by [39]. The emergence of these characteristics could be related to the distortion of the graphite oxide layers that developed during the exfoliation and restacking operations[40], [41]. The framework of the SN-rGO revealed by SEM is illustrated in Fig. 3 (c) and (d). The thermodynamic instability of the exfoliated 2-D arrangement of GO layers, as well as the van der Waals interactions among the GO sheets, might explain this behavior . The exfoliated GO sheets are linked with each other to stabilize form dense layers attributable to the thermodynamic disequilibrium [42]. Moreover, the presence of oxygen functional groups in GO layers promotes to thermal destabilization at high temperatures [43]. The internal and exterior linking of the exfoliated GO sheets are supposed to generate microwrinkling along

with multiple layers [44]. It is noticeable from the SEM images that the stretched sheets displayed a lateral dimensions varying between several microns in size to tens of microns in length exhibiting layered architectures.

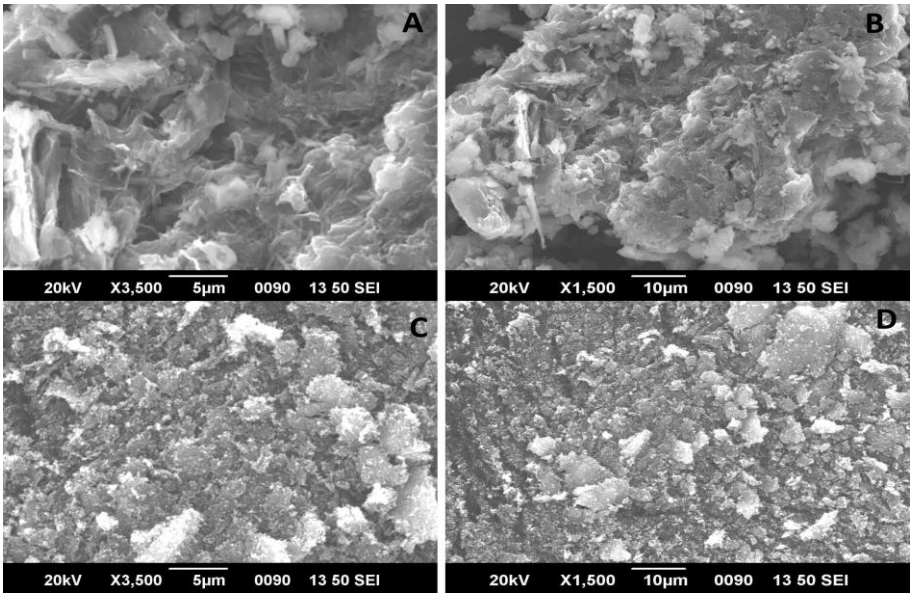

Figure 3 Microstructure observation of Graphene Oxide(GO) and Sulphur, Nitrogen Codoped Reduced Graphene Oxide (SN-rGO)

3.4. Elemental analysis using Energy dispersive X-ray spectroscopy (EDX)

For extremely sensitive analyte detection, the elemental composition of nanocomposites is crucial. For extremely sensitive analyte detection, the elemental composition of nanocomposites is crucial. In this case, the EDX gives information on the composition's elements. In this study, Figure 4 displays the EDX spectra of SN-rGO, which verified the existence of carbon (C), sulphur (S), nitrogen (N), and oxygen (O), respectively. The percentage composition of 'S' and 'N' present in the resulting material may be used to validate the doping of 'S' and 'N' in nanomaterial. In summary, the EDX spectra of SN-rGO indicated that the nanomaterial included 3.17 wt% of 'S,' 5.46 wt% of 'N,' and 50.5 wt% of 'C'. As a result, the overall synthesis of SN-rGO nanomaterial was validated using known components such as S, N, C, and O.

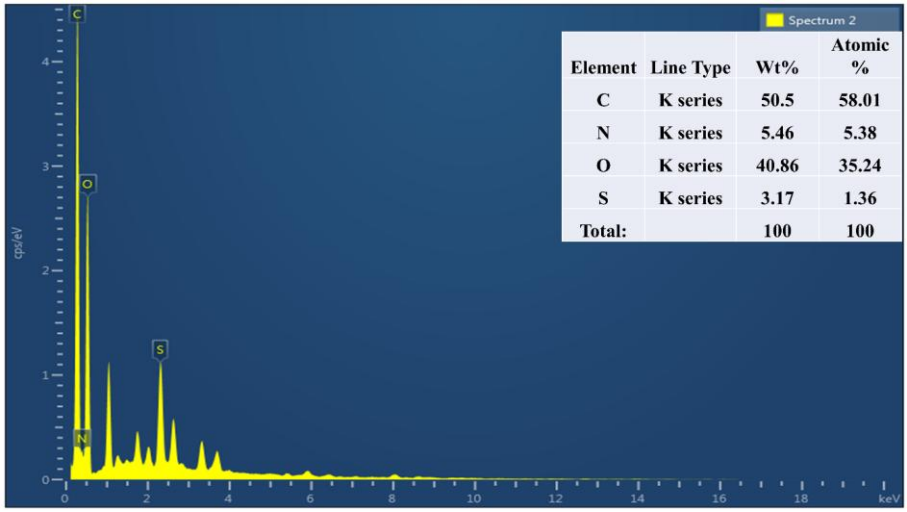

Figure 4 Energy dispersive X-ray spectroscopy (EDX) micrograph of the Sulphur,Nitrogen Codoped Reduced Graphene Oxide (SN-rGO)

3.5. Spectroscopic sensing of Pb2+, Hg2+, and Cr (VI) by SN-rGO nanomaterial

In this work, the SN-rGO nanomaterial was tested for spectral and optical detection of the aforementioned heavy metal ions. The sensing study's specifics are detailed under the relevant part.

Sensing of Hg^{2+}

The SN-rGO nanomaterial was put to the test for determining Hg^{2+} spectroscopically. It is considerably easier to perceive shifts in the UV absorption band during the measurement of Hg^{2+} because the SN-rGO nanomaterial forms a strong UV absorption band (Fig. 5). When the quantity of Hg^{2+} ions was increased, there was a substantial drop in the absorption crest with a red shift in the UV band of the SN-rGO nanomaterial. As a result, Hg^{2+} at a concentration of 15 µM was chosen as the detection limit for SN-rGO nanomaterial (r^2 = 0.022x + 0.09). The UV absorbance peak vanished after 500 µM concentration of Hg^{2+} was added to the nanocomposite. The existence of 75 µM Hg^{2+} ions in the contaminated sample was verified by the loaded sample analysis. The red-shift and substantial fall in the peak intensity were occurred attributable to the redox interaction involving the Hg^{2+} ions and the SN-rGO nanomaterial. The adsorption of Hg^{2+} across the SN-rGO nanomaterial layer,

which resulted in the formation of a combination, is responsible for the red-shift in the UV absorption band. Finally, by adding Hg2+, the SN-rGO nanomaterial became colorless.

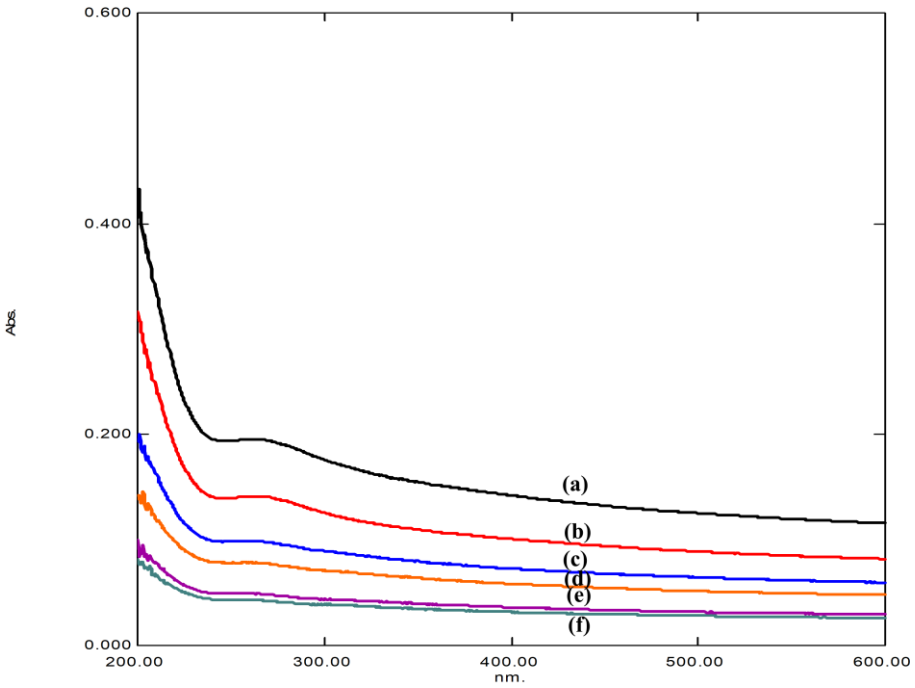

Figure 4 UV absorption spectral changes observed for SN-rGO nanomaterial upon the addition of Hg^{+} ions: (a) 0 µM, (b) 15 µM, (c) 50 µM, (d) 75 µM, (e) 100 µM, and (f) 250 µM of Hg^{+} ions with SN-rGO nanomaterial.

Sensing of Cr (VI)

The UV spectroscopic method was used to identify the Cr (VI) ion by the SN-rGO nanomaterial. Figure 6 depicts how the UV absorption spectra of SN-rGO nanomaterial diminish as the concentration of Cr (VI) ions increases. This indicates that the strength of the SN-rGO nanomaterial's UV absorption peak is inversely related to the concentration of Cr (VI). At the greatest concentration of Cr (VI) ions, the peak finally vanished. At a concentration of Cr (VI) ions of 25 nM, the UV spectra of SN-rGO nanomaterial shift. It displayed a strong peak at 283 nm (r^2 = 0.0014x + 0.05). The height of this peak was considerably lowered with rising concentration of Cr (VI) . The abrupt changes in the peak at 25 nM Cr (VI) concentration were regarded as a detection limit. The distinctive UV absorption peak was entirely eliminated with the addition of 1×10^4 nM Cr (VI) ions to the SN-rGO nanomaterial solution. The spiking sample findings reveled that the wastewater

contained 50 nM of Cr (VI). Altogether, the high adsorption of Cr (VI) on the SN-rGO nanomaterial offers good sensing capabilities. Lastly, the addition of Cr (VI) ion in the solution of SN-rGO nanomaterial was rendered colorless, which can be detected visually and can be validated by UV spectroscopy.

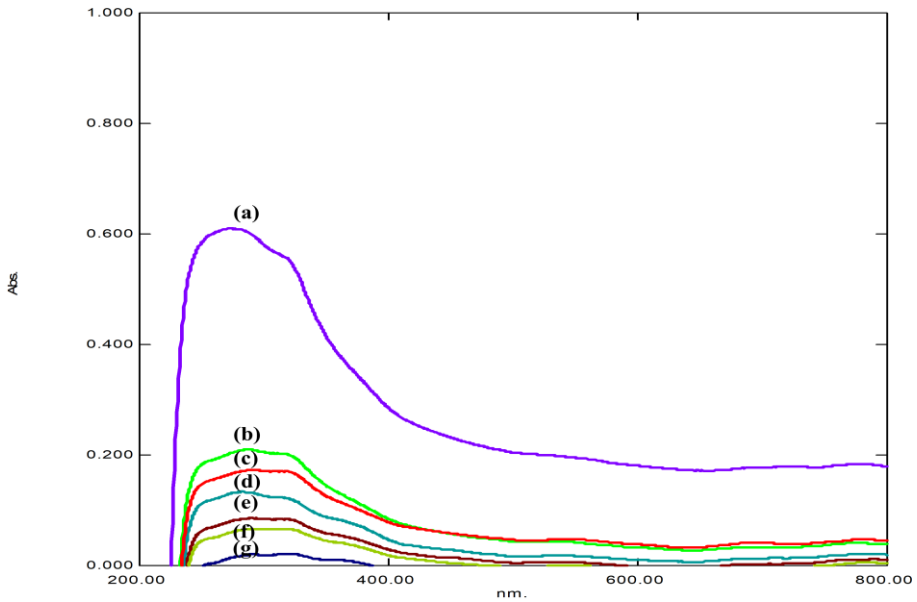

***Figure 5** Spectroscopic sensing of Cr (VI) using SN-rGO nanomaterial: (a) 0 nM, (b) 25 nM, (c) spiked sample (50 nM), (d) 100 nM, (e) 250 nM, (f) 500 nM, and (g) 2500 nM of $K_2Cr_2O_7$ solution with SN-rGO nanomaterial*

The basic sensing mechanism of this nanomaterial is yet unclear, however numerous potential processes have been described by previously published literature. The basic sensing mechanism of this nanomaterial is yet unclear, however numerous potential processes have been described by previously published literature. In summary, the inclusion of rGO aids heavy metal adsorption on the surface of nanomaterial via strong electrostatic interaction plus π-π stacking. It is worth noting that the S and N has the same atomic radius as graphene, which includes carbon. Because it has the same atomic radius as ‘N,' it is easily doped into carbon grid. As a consequence of the effective doping of 'S' and ‘N' into graphene lattice, the sensing ability has been enhanced, resulting in the lowest detection limit for heavy metal ions.

4. Conclusion

To summarize, the ecological synthesis of SN-rGO nanomaterial is a one-step, simple, cost-effective, and time-efficient technique. The Slaughter House Waste are rich in ‘S' and ‘N' containing amino acids and proteins, which deliver the S and N doping. This also helps to stabilize the nanomaterial by reducing the GO. SEM and EDX analyses were used to describe the fabricated sulphur and nitrogen codoped graphene, as well as the GO, providing concreate evidence of S and N element codoping. The FTIR result confirmed the SEM and EDX findings, as evidenced by the absence of the OH- and C-O bands following GO reduction. In a nutshell, the disclosed technique resulted in the environmentally benign production of the SN-rGO nanomaterial. With lower detection limits of 15 μM and 25 nM, this nanomaterial provided an effective probe for the detection of Hg^{2+} and Cr (VI), respectively. Furthermore, employing generated SN-rGO nanomaterial to analyze heavy metals (Hg^{2+} and Cr (VI)) in spiked samples demonstrated great potential. Additionally, the use of a simple spectroscopic approach in conjunction with sustainable and ecological nanocomposites can give an inexpensive alternative to traditional and costly techniques for heavy metal identification in water. Overall, the results of these studies indicated that the SN-rGO nanomaterial performed better in terms of Hg^{2+}, and Cr (VI) sensing in water using the spectroscopic technique. This nanomaterial has the potential to improve environmental upswing in the future.

Acknowledgements

The authors are also grateful to Asist Prof.Shradhha Mahakal, Mr.Sopan Nangare for there valuable guidance.As well the Management and Principal, RCPACS and HRPIPER college college, Shirpur for providing the necessary facilities, support and encouragement.

Conflict of Interests

The authors declare that no competing interest exists.

References

[1] A. K. Geim and K. S. Novoselov, “The rise of graphene,” in *Nanoscience and technology: a collection of reviews from nature journals*, World Scientific, 2010, pp. 11–19.

[2] V. B. Mohan, K. Lau, D. Hui, and D. Bhattacharyya, “Graphene-based materials and their composites: A review on production, applications and product limitations,” *Compos. Part B Eng.*, vol. 142, pp. 200–220, 2018.

[3] P. O. Patil *et al.*, "Graphene-based nanocomposites for sensitivity enhancement of surface plasmon resonance sensor for biological and chemical sensing: A review," *Biosens. Bioelectron.*, vol. 139, p. 111324, 2019.

[4] H. Liu and H. Qiu, "Recent advances of 3D graphene-based adsorbents for sample preparation of water pollutants: A review," *Chem. Eng. J.*, vol. 393, p. 124691, 2020.

[5] B. Y. Z. Hiew *et al.*, "Review on synthesis of 3D graphene-based configurations and their adsorption performance for hazardous water pollutants," *Process Saf. Environ. Prot.*, vol. 116, pp. 262–286, 2018.

[6] T. Szabó *et al.*, "Evolution of surface functional groups in a series of progressively oxidized graphite oxides," *Chem. Mater.*, vol. 18, no. 11, pp. 2740–2749, 2006.

[7] W. Gao, L. B. Alemany, L. Ci, and P. M. Ajayan, "New insights into the structure and reduction of graphite oxide," *Nat. Chem.*, vol. 1, no. 5, pp. 403–408, 2009.

[8] F. Kim, L. J. Cote, and J. Huang, "Graphene oxide: surface activity and two- dimensional assembly," *Adv. Mater.*, vol. 22, no. 17, pp. 1954–1958, 2010.

[9] X. Li, H. Wang, J. T. Robinson, H. Sanchez, G. Diankov, and H. Dai, "Simultaneous nitrogen doping and reduction of graphene oxide," *J. Am. Chem. Soc.*, vol. 131, no. 43, pp. 15939–15944, 2009.

[10] K. A. Mkhoyan *et al.*, "Atomic and electronic structure of graphene-oxide," *Nano Lett.*, vol. 9, no. 3, pp. 1058–1063, 2009.

[11] P. Zhang, T. Tachikawa, M. Fujitsuka, and T. Majima, "Efficient charge separation on 3D architectures of TiO 2 mesocrystals packed with a chemically exfoliated MoS 2 shell in synergetic hydrogen evolution," *Chem. Commun.*, vol. 51, no. 33, pp. 7187–7190, 2015.

[12] Y. Agrawal *et al.*, "High-performance stable field emission with ultralow turn on voltage from rGO conformal coated TiO 2 nanotubes 3D arrays," *Sci. Rep.*, vol. 5, no. 1, pp. 1–12, 2015.

[13] A. L. Linsebigler, G. Lu, and J. T. Yates Jr, "Photocatalysis on TiO2 surfaces: principles, mechanisms, and selected results," *Chem. Rev.*, vol. 95, no. 3, pp. 735–758, 1995.

[14] S. J. Lee *et al.*, "Heteroatom-doped graphene-based materials for sustainable energy applications: A review," *Renew. Sustain. Energy Rev.*, vol. 143, p. 110849, 2021.

[15] R. Kumar *et al.*, "Heteroatom doped graphene engineering for energy storage and conversion," *Mater. Today*, 2020.

[16] S. Kaushal, M. Kaur, N. Kaur, V. Kumari, and P. P. Singh, "Heteroatom-doped graphene as sensing materials: a mini review," *RSC Adv.*, vol. 10, no. 48, pp. 28608–28629, 2020.

[17] X. Wang, G. Sun, P. Routh, D.-H. Kim, W. Huang, and P. Chen, "Heteroatom-doped graphene materials: syntheses, properties and applications," *Chem. Soc. Rev.*, vol. 43, no. 20, pp. 7067–7098, 2014.

[18] L. K. Putri, W.-J. Ong, W. S. Chang, and S.-P. Chai, "Heteroatom doped graphene in photocatalysis: a review," *Appl. Surf. Sci.*, vol. 358, pp. 2–14, 2015.

[19] J. Duan, S. Chen, M. Jaroniec, and S. Z. Qiao, "Heteroatom-doped graphene-based materials for energy-relevant electrocatalytic processes," *Acs Catal.*, vol. 5, no. 9, pp. 5207–5234, 2015.

[20] B. Guo, L. Fang, B. Zhang, and J. R. Gong, "Graphene Doping: A Review," *Insciences J.*, vol. 1, no. 2, pp. 80–89, 2011, doi: 10.5640/insc.010280.

[21] A. Castellanos-Gómez *et al.*, "Electronic inhomogeneities in graphene: the role of the substrate interaction and chemical doping," *arXiv Prepr. arXiv1210.4147*, 2012.

[22] H. Wang *et al.*, "Phosphorus-doped graphene and (8, 0) carbon nanotube: structural, electronic, magnetic properties, and chemical reactivity," *Appl. Surf. Sci.*, vol. 273, pp. 302–309, 2013.

[23] H. Lee, K. Paeng, and I. S. Kim, "A review of doping modulation in graphene," *Synth. Met.*, vol. 244, pp. 36–47, 2018.

[24] E. García-Hernández, E. Salazar-García, E. Shakerzadeh, and E. Chigo-Anota, "Effect of dehydrogenated hydrocarbon doping on the electronic properties of graphene-type nanosheets," *Phys. Lett. A*, vol. 384, no. 27, p. 126702, 2020.

[25] A. Y. Luo *et al.*, "Electronic structure, carrier mobility and device properties for mixed-edge phagraphene nanoribbon by hetero-atom doping," *Org. Electron.*, vol. 51,

pp. 277–286, 2017.

[26] T.-F. Yeh, J. Cihlář, C.-Y. Chang, C. Cheng, and H. Teng, “Roles of graphene oxide in photocatalytic water splitting,” *Mater. Today*, vol. 16, no. 3, pp. 78–84, Mar. 2013, doi: 10.1016/j.mattod.2013.03.006.

[27] Y. Fujimoto, “Formation, energetics, and electronic properties of graphene monolayer and bilayer doped with heteroatoms,” *Adv. Condens. Matter Phys.*, vol. 2015, 2015.

[28] Y. Jiang, S. Chowdhury, and R. Balasubramanian, “New insights into the role of nitrogen-bonding configurations in enhancing the photocatalytic activity of nitrogen-doped graphene aerogels,” *J. Colloid Interface Sci.*, vol. 534, pp. 574–585, 2019.

[29] C. Maouche *et al.*, “A 3D nitrogen-doped graphene aerogel for enhanced visible-light photocatalytic pollutant degradation and hydrogen evolution,” *RSC Adv.*, vol. 10, no. 21, pp. 12423–12431, 2020.

[30] A. M. Massadeh, A.-W. O. El-Rjoob, and S. A. Gharaibeh, “Analysis of selected heavy metals in tap water by inductively coupled plasma-optical emission spectrometry after pre-concentration using chelex-100 ion exchange resin,” *Water, Air, Soil Pollut.*, vol. 231, pp. 1–14, 2020.

[31] A. Mahar *et al.*, “Challenges and opportunities in the phytoremediation of heavy metals contaminated soils: a review,” *Ecotoxicol. Environ. Saf.*, vol. 126, pp. 111–121, 2016.

[32] R. Chandrashekhar, B. Ram, and N. L. Bhavani, “Quantitative Analysis of Phytochemical Compounds in the Cotton (Gossypium) Seed Extracts; an Important Commercial Crop Plant.,” *Bull. Pure Appl. Sci.*, no. 1, 2019.

[33] J. H. Patil, M. P. More, M. R. Mahajan, A. G. Patil, P. K. Deshmukh, and P. O. Patil, “Green synthesis of graphene based manocomposite for sensing of heavy metals,” *J. Pharm. Biol. Sci.*, vol. 7, no. 2, pp. 56–62, 2019.

[34] V. Loryuenyong, K. Totepvimarn, P. Eimburanapravat, W. Boonchompoo, and A. Buasri, “Preparation and characterization of reduced graphene oxide sheets via water-based exfoliation and reduction methods,” *Adv. Mater. Sci. Eng.*, vol. 2013, 2013.

[35] J. Leffler, “Towards graphene based transparent conductive coating,” *Luleå Univ.*, 2012.

[36] E.-Y. Choi *et al.*, "Noncovalent functionalization of graphene with end-functional polymers," *J. Mater. Chem.*, vol. 20, no. 10, pp. 1907–1912, 2010.

[37] A. K. Mageed *et al.*, "Preparation and characterization of nitrogen doped reduced graphene oxide sheet," *Int J Appl Chem*, vol. 12, no. 1, pp. 104–108, 2016.

[38] I. A. de B. Moura, T. G. de Sousa, A. M. Lima, W. O. da Silva, and L. P. Brandao, "Synthesis and Characterization of graphene-oxide reinforced copper matrix composite," in *Materials Proceedings*, 2020, vol. 4, no. 1, p. 72.

[39] C. Fu, G. Zhao, H. Zhang, and S. Li, "Evaluation and characterization of reduced graphene oxide nanosheets as anode materials for lithium-ion batteries," *Int. J. Electrochem. Sci*, vol. 8, no. 5, pp. 6269–6280, 2013.

[40] H. C. Schniepp *et al.*, "Functionalized single graphene sheets derived from splitting graphite oxide," *J. Phys. Chem. B*, vol. 110, no. 17, pp. 8535–8539, 2006.

[41] M. Alanyalıoğlu, J. J. Segura, J. Oro-Sole, and N. Casan-Pastor, "The synthesis of graphene sheets with controlled thickness and order using surfactant-assisted electrochemical processes," *Carbon N. Y.*, vol. 50, no. 1, pp. 142–152, 2012.

[42] W. Zhang, P. Wu, Z. Li, and J. Yang, "First-principles thermodynamics of graphene growth on Cu surfaces," *J. Phys. Chem. C*, vol. 115, no. 36, pp. 17782–17787, 2011.

[43] N. J. Vickers, "Animal communication: when i'm calling you, will you answer too?," *Curr. Biol.*, vol. 27, no. 14, pp. R713–R715, 2017.

[44] H.-M. Ju, S.-H. Choi, and S. H. Huh, "X-ray diffraction patterns of thermally-reduced graphenes," *J. Korean Phys. Soc*, vol. 57, no. 6, p. 1649, 2010.

Paper 56

APPLICATIONS OF PROBABILITY ON COWRY SHELL GAME

Commented [AMD5R4]:

PRADEEP KUMAR R[1], PRAGATHI G[2], RAJESH KANNA M.R[3,*]

[1] Department of Mathematics,
The GSSS Institute of Engineering and Technology for Women,
Mysuru, India.
[2] Student, Bachelor of Engineering
Department of Information Science and Engineering,
The GSSS Institute of Engineering and Technology for Women,
Mysuru India.

[3]Department of Mathematics,
Sri. D. Devaraja Urs Government First Grade College,
Hunsur India

Abstract

In this article, we computed the probability values of cowry shells, plotted the graph for the cowry shell values and determined the mean, variance and standard deviation of cowry shell by applying binomial distribution

Mathematics Subject Classification: 60A05, 60E05, 60E99

Keywords and Phrases: Probability distribution function, sample space, binomial distribution, mean, variance, standard deviation, cowry shell

1. INTRODUCTION

Probability is defined as number of favourable events to number of total events. A probability distribution is a function that describes all possible values that a random variable can take within a given range [1]. p(x) is said to be probability function if it satisfies two conditions

i. $p(x_i)>=0$
ii. $\sum_{i=1}^{n} p(xi) = 1$

where x is a random variable defined as a variable whose future value is unpredictable despite knowing its past performance. The mean is the average or the most common value in a collection of all possible outcome values. Variance measures how far each number in the set is from the mean and also every other number in the set [2]. Standard deviation is

calculated as the square root of variance by determining each data point's deviation relative to mean.

Cowry game is an ancient board game originated in India. It is a game of chance and strategy [3] with the objective of moving players pieces through a specified path into a final location, according to the roll of special dice called cowry shells. The cowry shells contain an element of chance such as in dice [4,11]. The cowry shell involves uncertainty and fuzziness. [5,6,7] Hence it can be served as an excellent example to apply methods and concepts of probability.

Binomial distribution was introduced by JAKOB BERNOULLI, a Swiss mathematician, in 1713 [8]. Binomial distribution has exactly two possible outcomes. The assumptions of binomial distribution are that there is only one outcome for each trial, that each trial has the same probability of success and that each trial is mutually exclusive or independent of each other [9].

Cowry shell also has exactly two possible outcomes one with a cowry shell upwards and other with a cowry shell downwards. Hence the concepts of binomial distribution can be applied to cowry shell. This project is aimed at evaluating the values of cowry shell using probability concepts which may be further helpful in the field of Machine Learning and Artificial Intelligence [10].

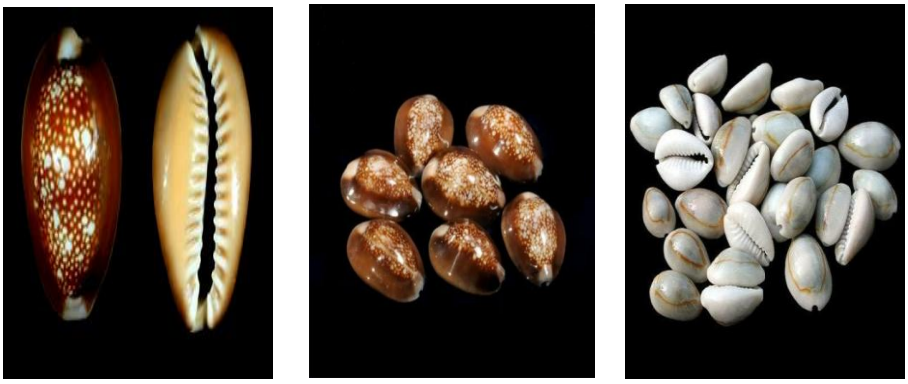

Figure 1.1: Cowry Shells

2. COWRY SHELL PROBABILITY VALUES

Theorem 2.1. For 'n' number of cowry shells there will be 'n+1' number of possible outcomes [for all n≥1]

Proof:

- Consider n=4

  If we throw 4 cowry shells the possible outcomes are 1, 2, 3, 4, 8

  There are 5 possible outcomes [4+1]

- Consider n=6

  If we throw 6 cowry shells the possible outcomes are 1, 2, 3, 4, 5, 6, 12

  There are 7 possible outcomes [6+1]

Therefore, we can conclude that for 'n' cowry shell, we get 'n+1' possible outcomes.

Theorem 2.2. For 'n' number of cowry shell, the minimum and maximum values are always one and 2n respectively [for all n≥1]

Proof:

- consider n=4

  If we throw 4 cowry shells, the possible outcomes are 1, 2, 3, 4, 8

  Here the minimum is 1 and maximum is 8 [2×4]

- consider n=3

  If we throw 3 cowry shells, the possible outcomes are 1, 2, 3, 6

  Here the minimum is 1 and maximum is 6 [2×3]

- consider n=6

  If we throw 6 cowry shells, the possible outcomes are 1, 2, 3, 4, 5, 6, 12

  Here the minimum is 1 and maximum is 12[2×6]

- consider n=1

  If we throw a cowry shell, the possible outcomes are

  1, 2 not 1 and 0

  Because in the cowry game, the piece has to move at least one step forward in each chance of throwing the cowry shells. Getting a number 0 in that game has no meaning.

Theorem 2.3. For 'n' number of cowry shell, the probability of getting 'n/2' value is more when compared to other possible outcome values [If n is even].

Proof:

- Consider n=4

  Let us write a sample space for this:

  Sample space: $2^n = 2^4 = 16$

  {

  (0,0,0,0)

  (0,0,0,1) (0,0,1,0) (0,1,0,0) (1,0,0,0)

  (0,0,1,1) (0,1,1,0) (1,1,0,0) (1,0,0,1) (0,1,0,1) (1,0,1,0)

  (0,1,1,1) (1,0,1,1) (1,1,0,1) (1,1,1,0)

  (1,1,1,1)

  }

  Probability of getting 1: 4/16 = 0.25

  Probability of getting 2: 6/16 = 0.375

  Probability of getting 3: 4/16 = 0.25

  Probability of getting 4: 1/16 = 0.0625

  Probability of getting 8: 1/16 = 0.0625

  Here n/2 =2

  By observing the above values, probability of getting 2 is 0.375 which is greater than all.

  GRAPH: If we plot a graph by taking possible outcomes along X axis verses taking the probability values along Y axis,

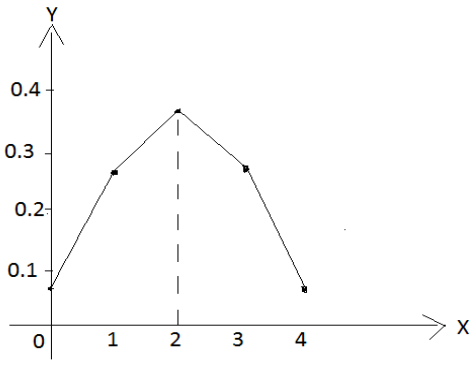

Figure 2.1: Cowry shell values for n=4

The resulting graph is symmetric.

- Consider n=6

Let us write a sample space for this:
Sample space: $2^n = 2^6 = 64$

{

(0,0,0,0,0,0)

(0,0,0,0,0,1) (0,0,0,0,1,0) (0,0,0,1,0,0) (0,0,1,0,0,0)
(0,1,0,0,0,0) (1,0,0,0,0,0)

(0,0,0,0,1,1) (0,0,0,1,0,1) (0,0,1,0,0,1) (0,1,0,0,0,1)
(0,1,1,1,1,0) (0,0,0,1,1,0) (0,0,1,0,1,0) (0,1,0,0,1,0)
(1,0,0,0,1,0) (0,0,1,1,0,0) (0,1,0,1,0,0) (1,0,0,1,0,0)
(0,1,1,0,0,0) (1,0,1,0,0,0) (1,1,0,0,0,0)

(0,0,0,1,1,1) (0,0,1,0,1,1) (0,1,0,0,1,1) (1,0,0,0,1,1)
(0,0,1,1,1,0) (0,1,0,1,1,0) (1,0,0,1,1,0) (0,1,1,1,0,0)
(1,0,1,1,0,0) (1,1,1,0,0,0) (1,1,0,1,0,0) (1,1,0,0,1,0)
(1,1,0,0,0,1) (0,1,1,0,1,0) (0,1,1,0,0,1) (0,1,0,0,1,1)
(0,0,1,1,0,1) (1,0,0,0,1,1) (1,0,0,1,0,1) (1,0,1,0,0,1)

(1,1,1,1,0,0) (1,1,1,0,1,0) (1,1,0,1,1,0) (1,0,1,1,1,0)
(0,1,1,1,1,0) (1,1,1,0,0,1) (1,1,0,1,0,1) (1,0,1,1,0,1)
(0,1,1,1,0,1) (1,1,0,0,1,1) (1,0,1,0,1,1) (0,1,1,0,1,1)
(1,0,0,1,1,1) (0,1,0,1,1,1) (0,0,1,1,1,1)

(1,1,1,1,1,0) (1,1,1,1,0,1) (1,1,1,0,1,1) (1,1,0,1,1,1)
(1,0,1,1,1,1) (0,1,1,1,1,1)

(1,1,1,1,1,1)

}

Probability of getting 1: 6/64 = 0.09375
Probability of getting 2: 15/64 = 0.234375
Probability of getting 3: 20/64 = 0.3125
Probability of getting 4: 15/64 = 0.234375
Probability of getting 5: 6/64 = 0.09375

Probability of getting 6: 1/64 = 0.015625

Probability of getting 12: 1/64 = 0.015625

GRAPH: If we plot a graph by taking possible outcomes along X axis verses taking the probability values along Y axis,

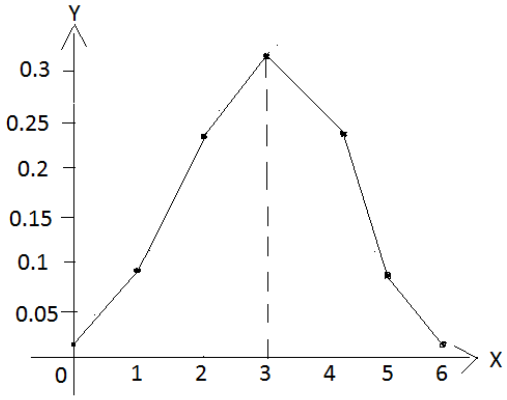

Figure 2.2: Cowry shell values for n=6

The resulting graph is symmetric.

Here n/2 =3

By observing the above values, probability of getting 3 is 0.3125 which is greater than all.

Theorem 2.4. The mean, variance, standard deviation of 'n' cowry shells can be calculated by n/2, n/4, $\sqrt{n/4}$ respectively.

Proof:

- Consider n=4

  The probability distribution table is as follows:

x_i	0	1	2	3	4
$p(x_i)$	0.0625	0.25	0.375	0.25	0.0625

Given: It is a probability distribution

Clearly, it is a probability function

i. $p(x_i)>=0$

ii. $\sum_{i=1}^{n} p(xi) = 1$

Mean: $\mu = \sum_{i=1}^{n} xi \,.\, p(xi)$

$= 0(0.0625) +1(0.25) +2(0.375) +3(0.25) +4(0.0625)$

$\mu = 2$

Mean: $n/2 = 4/2 = 2$

Since the above values are same mean can also be calculated by n/2.

Variance: $V = \sum_{i=1}^{n} p(xi).\, (x_i)^2 - \mu^2$

$= 0(0.0625) +1(0.25) +4(0.375) +9(0.25) +16(0.0625) - 2^2$

$= 5-4$

$= 1$

Variance: $n/4 = \frac{4}{4} = 1$

Since the above values are same variance can also be calculated by n/4.

Standard deviation is a root of variance

Therefore, σ can be calculated by $\sqrt{\frac{n}{4}}$.

- Consider n=6

The probability distribution table is as follows:

x_i	0	1	2	3	4	5	6
$p(x_i)$	0.015625	0.09375	0.234375	0.3125	0.234375	0.09375	0.015625

Given: It is a probability distribution

Clearly, it is a probability function

iii. $p(x_i)>=0$

iv. $\sum_{i=1}^{n} p(xi) = 1$

Mean: $\mu = \sum_{i=1}^{n} xi \,.\, p(xi)$

=0(0.015625) +1(0.09375) +2(0.234375) +3(0.3125) +4(0.234375)
+5(0.09375) +6(0.01625)
= 3

Mean: n/2 = $\frac{6}{2}$ =3

Since the above values are same mean can also be calculated by n/2.

Variance: V= $\sum_{i=1}^{n} p(xi)$. $(x_i)^2$ - μ^2

=0(0.015625)+1(0.09375)+4(0.234375)+9(0.3125)+16(0.234375)+25(0.09375)
+36(0. 015625) - 3^2

= 10.5 – 9

= 1.5

Variance: n/4 = $\frac{6}{4}$ =1.5

Since the above values are same variance can also be calculated by n/4.

Standard deviation is a root of variance

Therefore, σ can be calculated by $\sqrt{\frac{n}{4}}$.

Theorem 2.5. The probability of getting 'x' desired value out of 'n' cowry shell can be calculated using [${}^{n}C_{x}\,(0.5)^{n}$] formula.

Proof:

WKT, Binomial distribution is given by the formula

${}^{n}C_{x}\,p^{x}\,q^{n-x}$

In cowry shell concept p and q values are 0.5 (constant)

= ${}^{n}C_{x}\,(0.5)^{x}\,(0.5)^{n-x}$

= ${}^{n}C_{x}\,(0.5)^{n}$ OR ${}^{n}C_{x}/2^{n}$

Examples:

- The probability of getting 4 out of 6 cowry shells is 0.2343

Consider, ${}^{n}C_{x}\,(0.5)^{n}$

Here n=6, x=4: ${}^{6}C_{4.}\,(0.5)^{6}$ = 0.2344

0.2343 ≈0.2344

- The probability of getting 16 out of 20 cowry shells can be calculated by using the above formula

Here n=20, x=16: $^{20}C_{16} . (0.5)^{20} = 0.0046$

APPLICATIONS:

- Cowry values and efficiency values are very helpful in risk management in the cowry and chess board game respectively and also in determining statistical significance
- These values have a wide application in game theory
- These values are useful to write algorithms in Machine Learning and Artificial Intelligence
- An example of cowry shell can be considered in the concepts of binomial distribution along with the dice

CONCLUSION:

It is proved in this article that the cowry shell is a binomial distribution and the graph has been plotted for the same. Mean, Variance and Standard deviation of cowry shells are computed.

REFERENCES:

[1] "Probability distribution", [Online]. Available: https://www.investopedia.com/terms/p/probabilitydistribution.asp

[2] "Variance", [Online]. Available: https://www.investopedia.com/terms/v/variance.asp

[3] "Strategy (game theory)", [Online]. Available: https://en.wikipedia.org/wiki/Strategy_(game_theory)

[4] "Chowka bhara", [Online]. Available: https://en.wikipedia.org/wiki/Chowka_bhara

[5] "Board game", [Online]. Available: https://en.wikipedia.org/wiki/Board_game

[6] "Pachisi", [Online]. Available: https://en.wikipedia.org/wiki/Pachisi

[7] "Chaupar", [Online]. Available: https://en.wikipedia.org/wiki/Chaupar

[8] "Binomial distribution", Available https://www.britannica.com/science/binomial-distribution

[9] “Binomial distribution”, Available:
https://www.investopedia.com/terms/b/binomialdistribution.asp

[10] I. Millington, J. Funge, “Artificial intelligence for games”, 2nd ed., Morgan Kaufmann Publishers, 2009

[11] Dr.P. Nagabhushan, “Machine as One Player in Indian Cowry Board Game: Strategies and Analysis of Randomness Model for Playing”, 2017.

[12] “Chess”, [Online]. Available:
https://en.m.wikipedia.org/wiki/Chess

[13] “Chess piece”, [Online]. Available:
https://en.m.wikipedia.org/wiki/Chess_piece#:~:text=Depicted%20are%20the%20king%2C%20queen,or%20sage)%2C%20and%20jester

Paper 57

STUDIES ON TOPOLOGICAL PROPERTIES OF VERAPAMIL

Commented [AMD6R5]:

Roopa S.[1,2] and M. R. Rajesh Kanna[1,*]

[1] Department of Mathematics, Sri D. Devaraja Urs Government First Grade College, Hunsur, Karnataka, India.

[2] **Research Scholar,** Career Point University, Kota, Rajasthan, India.

Abstract: Chemists can employ graph theory to create a number of useful tools, such as "topological indices". A topological index is a numerical representation of the topological structure of Top(H)=Top(G) for every graph H that is isomorphic to G is a number belonging to a graph G. In this manuscript, we determine some indices, ABC_4, ABC, Randic connectivity, GA, Sum connectivity, GA_5, First, Second, First Multiple, Second multiple, Augmented and Hyper Zagreb indices, Harmonic, Forgotten topological, Symmetric division and also First, Second, Third Zagreb polynomials, Sombor index, Reduced Sombor index and Banhatti index of Verapamil.

I. INTRODUCTION

Qualitative predictions about reactivity of various compounds and the structure may obtained by chemists using simple rules provided by Graph theory. All the aspects of the application of graph theory to chemistry is concerned with chemical graph theory, which is a branch of mathematical chemistry. A molecular graph is a connected graph with atoms and chemical bonds as vertices and edges.

Verapamil is a medication that is used to control angina and treat excessive blood pressure (chest pain). The immediate-release tablets are also used to prevent and treat irregular heartbeats, either alone or in combination with other medications. Its molecular formula is $C_{27}H_{38}N_2O_4$.

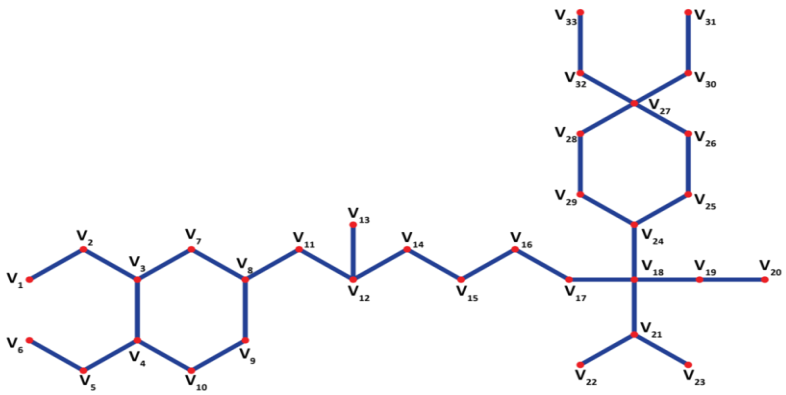

Figure 1 - Verapamil

The structures of chemical compounds are described by molecular descriptors which are nothing but topological indices. They help us to forecast certain physical and chemical properties like enthalpy of vaporization, stability, boiling point, etc. In this article, we have considered connected molecular graphs which have no multiple edges and loops.

Let G(V, E) be a graph with d_u as the degree of the vertex u. uv is an edge connected by the vertices u and v. "The ABC index is one of the degree – based molecular descriptors" , which was found by Estrada et al. It may also be used to model the thermodynamic properties of organic molecules as well as the stability of branched alkanes.

Definition.1.1. "ABC index" of G is stated as,

$$ABC(G) = \sum_{uv \in E} \sqrt{\frac{d_u + d_v - 2}{d_u d_v}}$$

The GA index was established by Vukicevic D. et.al. Have a look on further additional information [1,5].

Definition.1.2. "Fourth atom bond connectivity index" was established by Ghorbani M., et.al. in the year 2010 it was stated as

$$ABC_4(G) = \sum_{uv \in E(G)} \sqrt{\frac{s_u + s_v - 2}{s_u s_v}},$$

where S_u indicates the sum of degrees of all the, neighbors of vertex u in G, similarly for S_v.

Definition.1.3. One of the oldest topological indices based on degrees, which contributes quantitative measurement of branching of molecules is Randic index and is defined as,

$$\chi(G) = \sum_{uv \in E(G)} \frac{1}{\sqrt{d_u d_v}}$$

Definition.1.4. Zhou and Trinajstic established a sum connectivity index as,

$$S(G) = \sum_{uv \in E(G)} \frac{1}{\sqrt{d_u + d_v}}.$$

Definition.1.5. GA index can be stated as

$$GA(G) = \sum_{e=uv \in E(G)} \frac{2\sqrt{d_u d_v}}{d_u + d_v}$$

Definition 1.6. "Fifth Geometric – arithmetic index", was discovered by Graovac A., et.al. [9] in the year 2011, and is stated as

$$GA_5(G) = \sum_{uv \in E(G)} \frac{2\sqrt{s_u s_v}}{s_u + s_v}$$

Definition 1.7. "First and second Zagreb indices" can be stated as

$$Z_1(G) = \sum_{e=uv \in E(G)} (d_u + d_v) \quad , \quad Z_2(G) = \sum_{e=uv \in E(G)} (d_u d_v)$$

Definition 1.8. " Multiple Zagreb topological indices" of a graph G, according to the degree of vertices of G, were developed by Ghorbani M., and Azimi N., [6] in 2012. The following are the definitions for the first and second multiple Zagreb indices.

$$PM_1(G) = \prod_{e=uv \in E(G)} (d_u + d_v) \, , \quad PM_2(G) = \prod_{e=uv \in E(G)} (d_u d_v)$$

Definition.1.9. Furtula et.al. [4] established Augmented Zagreb index as

$$AZI(G) = \sum_{uv \in E} \left[\frac{d_u d_v}{d_u + d_v - 2}\right]^3$$

Definition.1.10. Zhong established Harmonic index can be stated as below

$$H(G) = \sum_{e=uv \in E(G)} \frac{2}{d_u + d_v}$$

Definition.1.11 . G. H. Shirdel et.al.[8] established Hyper-Zagreb index can be stated as,

$$HM(G) = \sum_{e=uv \in E(G)} (d_u + d_v)^2$$

For scientists in the pharmaceutical and medical fields, the forgotten topological index has proven to be valuable. It was used for building the biological and molecular characteristics of the recent medications. Such tactics are widely used in developing countries where there is a shortage of money for the purchase of relevant chemical reagents and equipment.

Definition.1.12. The "first, second, and third Zagreb Polynomials" were introduced by Faith – Tabar [2] in 2011.

$$ZG_1(G,x) = \sum_{e=uv \in E(G)} x^{d_u + d_v}$$

$$ZG_2(G,x) = \sum_{e=uv \in E(G)} x^{d_u d_v}$$

$$ZG_3(G,x) = \sum_{e=uv \in E(G)} x^{|d_u - d_v|}$$

Definition.1.13. "Furtula and Gutman" (2015)[3] established the forgotten topological index (also known as the F – index), which is defined as

$$F(G) = \sum_{e=uv \in E(G)} \left({d_u}^2 + {d_v}^2\right)$$

Definition.1.14. The forgotten topological polynomials for a graph G described as,

$$F(G,x) = \sum_{e=uv \in E(G)} x^{[(d_u)^2 + (d_v)^2]}.$$

Definition.1.15. Some new degree-bases graph invariants have been discovered, and they play an essential role in chemical graph theory. These topological indices can be used to calculate total surface area and heat formation in chemical compounds. The invariants of these graphs are as follows: Index of symmetric division

$$SDD(G) = \sum_{e=uv} \left\{ \frac{min(d_u, d_v)}{max(d_u, d_v)} + \frac{max(d_u, d_v)}{min(d_u, d_v)} \right\}$$

Definition.1.16. Novel graph invariant called the Sombor index of a graph is introduced by Gutman I., et .al. [7] and it is stated as

$$SO(G) = \sum_{uv \epsilon E} \left(\sqrt{{d_u}^2 + {d_v}^2} \right)$$

Definition.1.17. Recently I. Gutman established Reduced Sombor Index and it is stated as $SO_{red}(G) = \sum_{uv \epsilon E} \left(\sqrt{(d_u - 1)^2 + (d_v - 1)^2} \right)$, here d_u represents the degree of the vertex u, similarly for d_v **.**

It was shown that the reduced Sombor index can help to exhibit small discriminative potential and forecast physic-chemical properties of molecules, and that it performs slightly better than the Sombor index in this regards. Based on the results of a test of decreased Sombor indices predictive potential, it has been successfully applied to " modeling thermodynamic properties of substances".

Definition.1.18. "Banhatti Sombor index" of a connected graph G was established by Kulli [10]and is stated as

$$BSO(G) = \sum_{uv \epsilon E} \left(\sqrt{\frac{1}{{d_u}^2} + \frac{1}{{d_v}^2}} \right)$$

II. IMPORTANT OUTCOMES

Theorem 2.1 The ''Atom bond connectivity index'' of Verapamil is 23.6579525.

Proof: Consider a Verapamil $C_{27}H_{38}N_2O_4$. Let m_{ij} be the edges that connect the vertices of degrees $d_i$and d_j. "Two dimensional structure of Verapamil'' (as depicted in Figure – 1) contains edges of the type $m_{1,1}$, $m_{1,2}$, $m_{1,3}$, $m_{1,4}$, $m_{2,2}$, $m_{2,3}$, $m_{2,4}$, $m_{3,3}$, $m_{3,4}$. The number edges of these types, as shown in the diagram, are as follows: $|m_{1,1}|=1$, $|m_{1,2}|=4$, $|m_{1,3}|=3$, $|m_{1,4}|=1$, $|m_{2,2}|=6$, $|m_{2,3}|=11$, $|m_{2,4}|=5$, $|m_{3,3}|=1$ and $|m_{3,4}|=2$.

"Atom bond connectivity index" of verapamil

$$ABC(C_{27}H_{38}N_2O_4) = \sum_{uv \epsilon E} \sqrt{\frac{d_u + d_v - 2}{d_u d_v}}$$

$$= |\boldsymbol{m_{1,1}}| \sqrt{\frac{1+1-2}{1.1}} + |\boldsymbol{m_{1,2}}| \sqrt{\frac{1+2-2}{1.2}} + |\boldsymbol{m_{1,3}}| \sqrt{\frac{1+3-2}{1.3}} + |\boldsymbol{m_{1,4}}| \sqrt{\frac{1+4-2}{1.4}} + |\boldsymbol{m_{2,2}}| \sqrt{\frac{2+2-2}{2.2}} +$$

$$|\boldsymbol{m_{2,3}}| \sqrt{\frac{2+3-2}{2.3}} + |\boldsymbol{m_{2,4}}| \sqrt{\frac{2+4-2}{2.4}} + |\boldsymbol{m_{3,3}}| \sqrt{\frac{3+3-2}{3.3}} + |\boldsymbol{m_{3,4}}| \sqrt{\frac{3+4-2}{3.4}}$$

$$= 1 \times 0 + 4 \times \sqrt{\frac{1}{2}} + 3 \times \sqrt{\frac{2}{3}} + 1 \times \sqrt{\frac{3}{4}} + 6 \times \sqrt{\frac{2}{4}} + 11 \times \sqrt{\frac{3}{6}} + 5 \times \sqrt{\frac{4}{8}} + 1 \times \sqrt{\frac{4}{9}} + 26 \times \sqrt{\frac{5}{12}}$$

.

∴ ABC($C_{27}H_{38}N_2O_4$) = 23.6579525.

Theorem.2.2. The "Randic connectivity index" of Verapamil is 16.2296596.

Proof: TheRandic connectivity index of Verapamil $\chi(C_{27}H_{38}N_2O_4)$

$$\chi(C_{27}H_{38}N_2O_4) = \sum_{uv\in E(G)} \frac{1}{\sqrt{d_u d_v}}$$

$$= |m_{1,1}|\left(\frac{1}{\sqrt{1\times1}}\right) + |m_{1,2}|\left(\frac{1}{\sqrt{1\times2}}\right) + |m_{1,3}|\left(\frac{1}{\sqrt{1\times3}}\right) + |m_{1,4}|\left(\frac{1}{\sqrt{1\times4}}\right) + |m_{2,2}|\left(\frac{1}{\sqrt{2\times2}}\right) +$$

$$|m_{2,3}|\left(\frac{1}{\sqrt{2.3}}\right) + |m_{2,4}|\left(\frac{1}{\sqrt{2.4}}\right) + |m_{3,3}|\left(\frac{1}{\sqrt{3.3}}\right) + |m_{3,4}|\left(\frac{1}{\sqrt{3.4}}\right)$$

$$= 1\left(\frac{1}{\sqrt{1}}\right) + 4\left(\frac{1}{\sqrt{2}}\right) + 3\left(\frac{1}{\sqrt{3}}\right) + 1\left(\frac{1}{2}\right) + 6\left(\frac{1}{2}\right) + 11\left(\frac{1}{\sqrt{6}}\right) + 5\left(\frac{1}{\sqrt{8}}\right) + 1\left(\frac{1}{3}\right) + 2\left(\frac{1}{\sqrt{2}}\right)$$

$\therefore \chi(C_{27}H_{38}N_2O_4) = 16.2296596.$

Theorem 2.3 The Sum connectivity index of Verapamil is 18.1297311.

Proof: Thesum connectivity index of Verapamil $S(C_{27}H_{38}N_2O_4)$

$$= \sum_{uv\in E(G)} \frac{1}{\sqrt{d_u+d_v}}$$

$$= |m_{1,1}|\left(\frac{1}{\sqrt{1+1}}\right) + |m_{1,2}|\left(\frac{1}{\sqrt{1+2}}\right) + |m_{1,3}|\left(\frac{1}{\sqrt{1+3}}\right) + |m_{1,4}|\left(\frac{1}{\sqrt{1+4}}\right) + |m_{2,2}|\left(\frac{1}{\sqrt{2+2}}\right)$$

$$+ |m_{2,3}|\left(\frac{1}{\sqrt{2+3}}\right) + |m_{2,4}|\left(\frac{1}{\sqrt{2+4}}\right) + |m_{3,3}|\left(\frac{1}{\sqrt{3+3}}\right) + |m_{3,4}|\left(\frac{1}{\sqrt{3+4}}\right)$$

$$= 1\left(\frac{1}{\sqrt{2}}\right) + 4\left(\frac{1}{\sqrt{3}}\right) + 3\left(\frac{1}{\sqrt{4}}\right) + 1\left(\frac{1}{\sqrt{5}}\right) + 6\left(\frac{1}{2}\right) + 11\left(\frac{1}{\sqrt{5}}\right) + 5\left(\frac{1}{\sqrt{6}}\right) + 1\left(\frac{1}{\sqrt{6}}\right) + 2\left(\frac{1}{\sqrt{7}}\right)$$

$\therefore S(C_{27}H_{38}N_2O_4) = 18.1297311.$

Theorem 2.4 The ''GA'' index of Verapamil is 30.754981.

Proof: The 'GA'' index of Verapamil $GA(C_{27}H_{38}N_2O_4)$

$$= \sum_{e=uv\in E(G)} \frac{2\sqrt{d_u d_v}}{d_u+d_v}$$

$$= |m_{1,1}|\left(\frac{2\sqrt{1.1}}{1+1}\right) + |m_{1,2}|\left(\frac{2\sqrt{1.2}}{1+2}\right) + |m_{1,3}|\left(\frac{2\sqrt{1.3}}{1+3}\right) + |m_{1,4}|\left(\frac{2\sqrt{1.4}}{1+4}\right) + |m_{2,2}|\left(\frac{2\sqrt{2.2}}{2+2}\right) +$$

$$|m_{2,3}|\left(\frac{2\sqrt{2.3}}{2+3}\right) + |m_{2,4}|\left(\frac{2\sqrt{2.4}}{2+4}\right) + |m_{3,3}|\left(\frac{2\sqrt{3.3}}{3+3}\right) + |m_{3,4}|\left(\frac{2\sqrt{3.4}}{3+4}\right)$$

$$= 1\left(\frac{2\sqrt{1}}{2}\right) + 4\left(\frac{2\sqrt{2}}{3}\right) + 3\left(\frac{2\sqrt{3}}{4}\right) + 1\left(\frac{2\sqrt{4}}{5}\right) + 6\left(\frac{2\sqrt{4}}{4}\right) + 11\left(\frac{2\sqrt{6}}{5}\right) + 5\left(\frac{2\sqrt{8}}{6}\right) + 1\left(\frac{2\sqrt{9}}{6}\right) + 2\left(\frac{2\sqrt{12}}{7}\right).$$

$\therefore GA(C_{27}H_{38}N_2O_4) = 30.754981.$

Theorem 2.5 The "First Zagreb index" of Verapamil is 160.

Proof: "First Zagreb index" of Verapamil $Z_1(C_{27}H_{38}N_2O_4)$

$$= \sum_{e=uv\in E(G)}(d_u + d_v)$$

$$= |\boldsymbol{m_{1,1}}|(1+1) + |\boldsymbol{m_{1,2}}|(1+2) + |\boldsymbol{m_{1,3}}|(1+3) + |\boldsymbol{m_{1,4}}|(1+4) + |\boldsymbol{m_{2,2}}|(2+2) + |\boldsymbol{m_{2,3}}|(2+3) + |\boldsymbol{m_{2,4}}|(2+4) + |\boldsymbol{m_{3,3}}|(3+3) + |\boldsymbol{m_{3,4}}|(3+4)$$

$$= 1(2) + 4(3) + 3(4) + 1(5) + 6(4) + 11(5) + 5(6) + 1(6) + 2(7).$$

$\therefore$ $Z_1(C_{27}H_{38}N_2O_4) = 160$.

Theorem 2.6 The "second Zagreb index" of Verapamil is 185.

Proof: The "Second Zagreb index" of Verapamil $Z_2(C_{27}H_{38}N_2O_4)$

$$= \sum_{e=uv\in E(G)}(d_u . d_v)$$

$$= |\boldsymbol{m_{1,1}}|(1\times 1) + |\boldsymbol{m_{1,2}}|(1\times 2) + |\boldsymbol{m_{1,3}}|(1\times 3) + |\boldsymbol{m_{1,4}}|(1\times 4) + |\boldsymbol{m_{2,2}}|(2\times 2) + |\boldsymbol{m_{2,3}}|(2\times 3) + |\boldsymbol{m_{2,4}}|(2\times 4) + |\boldsymbol{m_{3,3}}|(3\times 3) + |\boldsymbol{m_{3,4}}|(3\times 4)$$

$$= 1(1) + 4(2) + 3(3) + 1(4) + 6(4) + 11(6) + 5(8) + 1(9) + 2(12).$$

$\therefore$ $Z_2(C_{27}H_{38}N_2O_4) = 185$.

Theorem.2.7. The "first multiple Zagreb index" of Verapamil is 2.370×10^{22}.

Proof: The "first multiple Zagreb index" of Verapamil $PM_1(C_{27}H_{38}N_2O_4)$

$$= \prod_{e=uv\in E(G)}(d_u + d_v)$$

$$= \prod_{e=uv\in 1,1}(d_{.u} + d_v) \prod_{e=u.v\in 1,2}(d_u + d_v) \prod_{e=uv\in 1,3}(d_u + d_v) \prod_{e=uv\in 2,2}(d_u + d_v) \prod_{e=uv\in 2,3}(d_u + d_v)$$

$\prod_{e=uv\in 2,4}(d_u + d_v) \prod_{e=uv\in 3,3}(d_u + d_v) \prod_{e=uv\in 3,4}(d_u + d_v)$.

$$= 2^1 \times 3^4 \times 4^3 \times 5^1 \times 4^6 \times 5^{11} \times 6^5 \times 6^1 \times 7^2.$$

$\therefore$ $PM_1(C_{27}H_{38}N_2O_4) = 2.370 \times 10^{22}$.

Theorem.2.8 The "second multiple Zagreb index" of Verapamil is 1.090×10^{23}.

Proof: The "second multiple Zagreb index" of Verapamil $PM_1(C_{27}H_{38}N_2O_4)$

$$= \prod_{e=uv\in E(G)}(d_u d_v)$$

$$= \prod_{e=uv\in 1,1}(d_u d_v). \prod_{e=uv\in 1,2}(d_u d_v). \prod_{e=uv\in 1,3}(d_u d_v). \prod_{e=uv\in 2,2}(d_u d_v). \prod_{e=uv\in 2,3}(d_u d_v). \prod_{e=uv\in 2,4}(d_u d_v). \prod_{e=uv\in 3,3}(d_u d_v). \prod_{e=uv\in 3,4}(d_u d_v).$$

$$= 1^1 \times 2^4 \times 3^3 \times 4^1 \times 4^6 \times 6^{11} \times 8^5 \times 9^1 \times 12^2.$$

$\therefore$ $PM_1(C_{27}H_{38}N_2O_4) = 1.090 \times 10^{23}$.

Theorem 2.9 The Augmented Zagreb index of Verapamil is 259.533.

Proof: The "Augmented Zagreb index" of Verapamil AZI(G) ($C_{27}H_{38}N_2O_4$)

$$= \sum_{uv\in E}\left[\frac{d_u d_v}{d_u+d_v-2}\right]^3$$

$$= |\boldsymbol{m_{1,1}}|\left[\frac{1.1}{1+1-2}\right]^3 + |\boldsymbol{m_{1,2}}|\left[\frac{1.2}{1+2-2}\right]^3 + |\boldsymbol{m_{1,3}}|\left[\frac{1.3}{1+3-2}\right]^3 + |\boldsymbol{m_{1,4}}|\left[\frac{1.4}{1+4-2}\right]^3$$

$$+ |\boldsymbol{m_{2,2}}|\left[\frac{2.2}{2+2-2}\right]^3 + |\boldsymbol{m_{2,3}}|\left[\frac{2.3}{2+3-2}\right]^3 + |\boldsymbol{m_{2,4}}|\left[\frac{2.4}{2+4-2}\right]^3$$

$$+ |\boldsymbol{m_{3,3}}|\left[\frac{3.3}{3+3-2}\right]^3 + |\boldsymbol{m_{3,4}}|\left[\frac{3.4}{3+4-2}\right]^3$$

$$= 1\left(\frac{1}{0}\right)^3 + 4\left(\frac{2}{1}\right)^3 + 3\left(\frac{3}{2}\right)^3 + 1\left(\frac{4}{3}\right)^3 + 6\left(\frac{4}{2}\right)^3 + 11\left(\frac{6}{3}\right)^3 + 5\left(\frac{8}{4}\right)^3 + 1\left(\frac{9}{4}\right)^3 + 2\left(\frac{12}{5}\right)^3.$$

$\therefore$ AZI(G) ($C_{27}H_{38}N_2O_4$) = 259.533.

Theorem 2.10 The "harmonic index" of Verapamil is 15. 5380.

Proof: The " harmonic index " of Verapamil H($C_{27}H_{38}N_2O_4$)

$$= \sum_{e=uv\in E(G)}\left(\frac{2}{d_u+d_v}\right)$$

$$= |\boldsymbol{m_{1,1}}|\left(\frac{2}{1+1}\right) + |\boldsymbol{m_{1,2}}|\left(\frac{2}{1+2}\right) + |\boldsymbol{m_{1,3}}|\left(\frac{2}{1+3}\right) + |\boldsymbol{m_{1,4}}|\left(\frac{2}{1+4}\right) + |\boldsymbol{m_{2,2}}|\left(\frac{2}{2+2}\right)$$

$$+ |\boldsymbol{m_{2,3}}|\left(\frac{2}{2+3}\right) + |\boldsymbol{m_{2,4}}|\left(\frac{2}{2+4}\right) + |\boldsymbol{m_{3,3}}|\left(\frac{2}{3+3}\right) + |\boldsymbol{m_{3,4}}|\left(\frac{2}{3+4}\right)$$

$$= 1\left(\frac{2}{2}\right) + 4\left(\frac{2}{3}\right) + 3\left(\frac{2}{4}\right) + 1\left(\frac{2}{5}\right) + 6\left(\frac{2}{4}\right) + 11\left(\frac{2}{5}\right) + 5\left(\frac{2}{6}\right) + 1\left(\frac{2}{6}\right) + 2\left(\frac{2}{7}\right)$$

$\therefore$ H($C_{27}H_{38}N_2O_4$)= 15.5380.

Theorem 2.11 The "hyper Zagreb index" of Verapamil is 798.

Proof: The "hyper Zagreb index" of Verapamil HZ($C_{27}H_{38}N_2O_4$)

$$= \sum_{e=uv\in E(G)}(d_u + d_v)^2$$

$$= |\boldsymbol{m_{1,1}}|.(1+1)^2 + |\boldsymbol{m_{1,2}}|(1+2)^2 + |\boldsymbol{m_{1,3}}|(1+3)^2 + |\boldsymbol{m_{1,4}}|(1+4)^2 + |\boldsymbol{m_{2,2}}|(2+2)^2$$

$$+ |\boldsymbol{m_{2,3}}|(2+3)^2 + |\boldsymbol{m_{2,4}}|(2+4)^2 + |\boldsymbol{m_{3,3}}|(3+3)^2 + |\boldsymbol{m_{3,4}}|(3+4)^2$$

$$= 1(2)^2 + 4(3)^2 + 3(4)^2 + 1(5)^2 + 6(4)^2 + 11(5)^2 + 5(6)^2 + 1(6)^2 + 2(7)^2.$$

$\therefore$ HZ($C_{27}H_{38}N_2O_4$)= 798.

Theorem 2.12 The first Zagreb polynomial of Verapamil is $2x^7 + 6x^6 + 12x^5 + 9x^4 + 4x^3 + x^2$.

Proof: First Zagreb polynomials of Verapamil ZG$_1$($C_{27}H_{38}N_2O_4$, x)

$$= \sum_{e=uv\in E(G)} x^{d_u+d_v}$$

$$= |\boldsymbol{m_{1,1}}|\, X^{(1+1)} + |\boldsymbol{m_{1,2}}|\, X^{(1+2)} + |\boldsymbol{m_{1,3}}|\, X^{(1+3)} + |\boldsymbol{m_{1,4}}|\, X^{(1+4)} + |\boldsymbol{m_{2,2}}|\, X^{(2+2)}$$

$$+ \ |\boldsymbol{m_{2,3}}| \, X^{(2+3)} + |\boldsymbol{m_{2,4}}| \, X^{(2+4)} + |\boldsymbol{m_{3,3}}| \, X^{(3+3)} + |\boldsymbol{m_{3,4}}| \, X^{(3+4)}$$

$$= 1x^2 + 4x^3 + 3x^4 + 1x^5 + 6x^4 + 11x^5 + 5x^6 + 1x^6 + 2x^7$$

∴ $ZG_1(C_{27}H_{38}N_2O_4, x) = 2x^7 + 6x^6 + 12x^5 + 9x^4 + 4x^3 + x^2.$

Theorem 2.13. The second Zagreb polynomials of Verapamil is $2x^{12} + x^9 + 5x^8 + x^6 + 7x^4 + 3x^3 + 4x^2 + x$.

Proof: Second Zagreb polynomials of Verapamil $ZG_2(C_{27}H_{38}N_2O_4, , x)$

$$= \sum_{e=uv \in E(G)} x^{d_u d_v}$$

$$= |\boldsymbol{m_{1,1}}| \, X^{(1.1)} + |\boldsymbol{m_{1,2}}| \, X^{(1.2)} + |\boldsymbol{m_{1,3}}| \, X^{(1.3)} + |\boldsymbol{m_{1,4}}| \, X^{(1.4)} + |\boldsymbol{m_{2,2}}| \, X^{(2.2)} + \ |\boldsymbol{m_{2,3}}| \, X^{(2.3)} + |\boldsymbol{m_{2,4}}| \, X^{(2.4)} + |\boldsymbol{m_{3,3}}| \, X^{(3.3)} + |\boldsymbol{m_{3,4}}| \, X^{(3.4)}$$

$$= 1x + 4x^2 + 3x^3 + 1x^4 + 6x^4 + 11x^6 + 5x^8 + 1x^9 + 2x^{12}$$

∴ $ZG_2(C_{27}H_{38}N_2O_4, x) = 2x^{12} + x^9 + 5x^8 + x^6 + 7x^4 + 3x^3 + 4x^2 + x.$

Theorem 2.14 The third Zagreb polynomials of Verapamil is $x^3 + 8x^2 + 17x + 8$.

Proof: Third Zagreb polynomials of Verapamil $ZG_3(C_{27}H_{38}N_2O_4, x)$

$$= \sum_{e=uv \in E(G)} x^{|d_u - d_v|}$$

$$= |m_{1,1}| \, x^{|1-1|} + |m_{1,2}| \, x^{|1-2|} + |m_{1,3}| \, x^{|1-3|} + |m_{1,4}| \, x^{|1-4|} + |m_{2,2}| \, x^{|2-2|} + \ |m_{2,3}| \, x^{|2-3|} + \ |m_{2,4}| \, x^{|2-4|} + |m_{3,3}| \, x^{|3-3|} + |m_{3,4}| x^{|3-4|}$$

$$= 1x^0 + 4x^1 + 3x^2 + 1x^3 + 6x^0 + 11x^1 + 5x^2 + 1x^0 + 2x^1$$

∴ $ZG_3(C_{27}H_{38}N_2O_4, x) = x^3 + 8x^2 + 17x + 8.$

Theorem.2.15. The forgotten topological index of Verapamil is 446.

Proof: Consider Forgotten topological index of Verapamil $F(C_{27}H_{38}N_2O_4)$

$$= \sum_{e=uv \in E(G)} [(d_u)^2 + (d_v)^2]$$

$$= |m_{1,1}|(1^2 + 1^2) + |m_{1,2}|(1^2 + 2^2) + |m_{1,3}| \, (1^2 + 3^2) + |m_{1,4}|(1^2 + 4^2) + |m_{2,2}| \, (2^2 + 2^2) + \ |m_{2,3}| \, (2^2 + 3^2) + \ |m_{2,4}| \, (2^2 + 4^2) + |m_{3,3}|(3^2 + 3^2) + |m_{3,4}|(3^2 + 4^2)$$

$$= 1(2) + 4(5) + 3(10) + 1(17) + 6(8) + 11(13) + 5(20) + 1(18) + 2(25)$$

∴ $F(C_{27}H_{38}N_2O_4) = 446.$

Theorem.2.16. The forgotten polynomials of Verapamil is $2x^{25} + 5x^{20} + x^{18} + x^{17} + 11x^{13} + 3x^{10} + 6x^8 + 4x^5 + x^2$.

Proof: Consider forgotten polynomials of Verapamil $FP(C_{27}H_{38}N_2O_4, x)$

$$= \sum_{e=uv \in E(G)} x^{[(d_u)^2 + (d_v)^2]}$$

$$= |m_{1,1}|\, x^{(1^2+1^2)} + |m_{1,2}|\, x^{(1^2+2^2)} + |m_{1,3}|\, x^{(1^2+3^2)} + |m_{1,4}|\, x^{(1^2+4^2)} + |m_{2,2}|\, x^{(2^2+2^2)} +$$
$$|m_{2,3}|\, x^{(2^2+3^2)} + |m_{2,4}|\, x^{(2^2+4^2)} + |m_{3,3}|\, x^{(3^2+3^2)} + |m_{3,4}|\, x^{(3^2+4^2)}$$
$$= 1x^2 + 4x^5 + 3x^{10} + 1x^{17} + 6x^8 + 11x^{13} + 5x^{20} + 1x^{18} + 2x^{25}$$

∴ FP($C_{27}H_{38}N_2O_4$, x) = $2x^{25} + 5x^{20} + x^{18} + x^{17} + 11x^{13} + 3x^{10} + 6x^8 + 4x^5 + x^2$.

Theorem 2.17 The "symmetric division index" of Verapamil is 80.75.

Proof: "Symmetric division index" of Verapamil SDI($C_{27}H_{38}N_2O_4$)

$$= \sum_{e=uv\in E(G)} \left\{\frac{min(d_u,d_v)}{max(d_u,d_v)} + \frac{max(d_u,d_v)}{min(d_u,d_v)}\right\}$$
$$= |m_{1,1}|\left\{\frac{min(1.1)}{max(1.1)} + \frac{max(1.1)}{min(1.1)}\right\} + |m_{1,2}|\left\{\frac{min(1.2)}{max(1.2)} + \frac{max(1.2)}{min(1.2)}\right\} + |m_{1,3}|\left\{\frac{min(1.3)}{max(1.3)} + \frac{max(1.3)}{min(1.3)}\right\} +$$
$$|m_{1,4}|\left\{\frac{min(1.4)}{max(1.4)} + \frac{max(1.4)}{min(1.4)}\right\} + |m_{2,2}|\left\{\frac{min(2.2)}{max(2.2)} + \frac{max(2.2)}{min(2.2)}\right\} + |m_{2,3}|\left\{\frac{min(2.3)}{max(2.3)} + \frac{max(2.3)}{min(2.3)}\right\} +$$
$$|m_{2,4}|\left\{\frac{min(2.4)}{max(2.4)} + \frac{max(2.4)}{min(2.4)}\right\} + |m_{3,3}|\left\{\frac{min(3.3)}{max(3.3)} + \frac{max(3.3)}{min(3.3)}\right\} + |m_{3,4}|\left\{\frac{min(3.4)}{max(3.4)} + \frac{max(3.4)}{min(3.4)}\right\}$$
$$= 2 + 4\times\frac{5}{2} + 3\times\frac{10}{3} + 1\times\frac{17}{4} + 6(2) + 11\times\frac{13}{6} + 5\times\frac{5}{2} + 1\times 2 + 2\times\frac{25}{12}.$$

∴ SDI($C_{27}H_{38}N_2O_4$) = 80.75.

Theorem.2.18. The Sombor in index of Verapamil is 117.2033

Proof: The Sombor index of Verapamil ($C_{27}H_{38}N_2O_4$)

$$= \sum_{e=uv\epsilon E}\left(\sqrt{{d_u}^2 + {d_v}^2}\right)$$
$$= |\boldsymbol{m_{1,1}}|\left(\sqrt{1^2+1^2}\right) + |\boldsymbol{m_{1,2}}|\left(\sqrt{1^2+2^2}\right) + |\boldsymbol{m_{1,3}}|\left(\sqrt{1^2+3^2}\right) + |\boldsymbol{m_{1,4}}|\left(\sqrt{1^2+4^2}\right)$$
$$+ |\boldsymbol{m_{2,2}}|\left(\sqrt{2^2+2^2}\right) + |\boldsymbol{m_{2,3}}|\left(\sqrt{2^2+3^2}\right) + |\boldsymbol{m_{2,4}}|\left(\sqrt{2^2+4^2}\right) + |\boldsymbol{m_{3,3}}|\left(\sqrt{3^2+3^2}\right)$$
$$+ |\boldsymbol{m_{3,4}}|\left(\sqrt{3^2+4^2}\right)$$

∴ SO($C_{27}H_{38}N_2O_4$) = 117.2033

Theorem.2.19. The Reduced Sombor in index of Verapamil is 49.5726

Proof: The Reduced Sombor index of Verapamil ($C_{27}H_{38}N_2O_4$)

$$SO_{red}(C_{27}H_{38}N_20_4) = \sum_{e=uv\epsilon E}\left(\sqrt{(d_u-1)^2 + (d_v-1)^2}\right)$$
$$= |\boldsymbol{m_{1,1}}|\left(\sqrt{0^2+0^2}\right) + |\boldsymbol{m_{1,2}}|\left(\sqrt{0^2+1^2}\right) + |\boldsymbol{m_{1,3}}|\left(\sqrt{0^2+2^2}\right) + |\boldsymbol{m_{1,4}}|\left(\sqrt{0^2+3^2}\right)$$
$$+ |\boldsymbol{m_{2,2}}|\left(\sqrt{1^2+1^2}\right) + |\boldsymbol{m_{2,3}}|\left(\sqrt{1^2+2^2}\right) + |\boldsymbol{m_{2,4}}|\left(\sqrt{1^2+3^2}\right) + |\boldsymbol{m_{3,3}}|\left(\sqrt{2^2+2^2}\right)$$

$$+|\boldsymbol{m_{3,4}}|\left(\sqrt{2^2+3^2}\right)$$

∴ SO($C_{27}H_{38}N_2O_4$) = 49.5726

Theorem.2.20. The Reduced Sombor index of Verapamil is 49.5726.

Proof: The Reduced Sombor index of Verapamil ($C_{27}H_{38}N_2O_4$)

$$SO_{red}(C_{27}H_{38}N_20_4) = \sum_{e=uv\epsilon E}\left(\sqrt{(d_u-1)^2+(d_v-1)^2}\right)$$

$$= |\boldsymbol{m_{1,1}}|\left(\sqrt{0^2+0^2}\right)+|\boldsymbol{m_{1,2}}|\left(\sqrt{0^2+1^2}\right)+|\boldsymbol{m_{1,3}}|\left(\sqrt{0^2+2^2}\right)+|\boldsymbol{m_{1,4}}|\left(\sqrt{0^2+3^2}\right)$$

$$+|\boldsymbol{m_{2,2}}|\left(\sqrt{1^2+1^2}\right)+|\boldsymbol{m_{2,3}}|\left(\sqrt{1^2+2^2}\right)+|\boldsymbol{m_{2,4}}|\left(\sqrt{1^2+3^2}\right)+|\boldsymbol{m_{3,3}}|\left(\sqrt{2^2+2^2}\right)$$

$$+|\boldsymbol{m_{3,4}}|\left(\sqrt{2^2+3^2}\right)$$

∴ SO($C_{27}H_{38}N_2O_4$) = 49.5726

Theorem.2.21. The Banhatti Sombor index of Verapamil is 25.0320.

Proof: The Banhatti Reduced Sombor index of Verapamil

$$BSO(C_{27}H_{38}N_20_4) = \sum_{e=uv\epsilon E(G)}\left(\sqrt{\frac{1}{d_u{}^2}+\frac{1}{d_v{}^2}}\right)$$

$$= |\boldsymbol{m_{1,1}}|\left(\sqrt{\frac{1}{1^2}+\frac{1}{1^2}}\right)+|\boldsymbol{m_{1,2}}|\left(\sqrt{\frac{1}{1^2}+\frac{1}{2}}\right)+|\boldsymbol{m_{1,3}}|\left(\sqrt{\frac{1}{1^2}+\frac{1}{3^2}}\right)+|\boldsymbol{m_{1,4}}|\left(\sqrt{\frac{1}{1^2}+\frac{1}{4^2}}\right)$$

$$+|\boldsymbol{m_{2,2}}|\left(\sqrt{\frac{1}{2^2}+\frac{1}{2^2}}\right)+|\boldsymbol{m_{2,3}}|\left(\sqrt{\frac{1}{2^2}+\frac{1}{3^2}}\right)+|\boldsymbol{m_{2,4}}|\left(\sqrt{\frac{1}{2^2}+\frac{1}{4^2}}\right)+|\boldsymbol{m_{3,3}}|\left(\sqrt{\frac{1}{3^2}+\frac{1}{3^2}}\right)$$

$$+|\boldsymbol{m_{3,4}}|\left(\sqrt{\frac{1}{3^2}+\frac{1}{4^2}}\right)$$

∴ SO($C_{27}H_{38}N_2O_4$) = 25.0320.

III. Conclusion

In this article we have calculated topological indices of Verapamil without using computer.

IV. REFERENCES

1. D. Vukicevic-B. Furtula, Topological index based on the ratios of geometrical and arithmetical means of end-vertex degrees of edges, J. Math. Chem., 46, (2009) 1369-1376.

2. Ali Astanesh- Asl and G. H Fath – Tabar, Computing the first and third Zagreb polynomials of curtained product of graphs, Irsnisn Journal of Mathematical Chemistry. 2-2(2011), 73-78.
3. B. Furtula and Gutman I, A forgotton topological index, J. Math. Chem.53.(2015)213-22.
4. B. Furtula, A. Graovac, D. Vuki_cevi_c, Augmented Zagreb index, J. Math. Chem. 48(2010) 370-380.
5. E. Estrada, L. Torres, L. Rodriguez, I. Gutman, An atom-bond connectivity index: Modelling the enthalpy of formation of alkanes, Indian J. Chem. 37A (1998), 849-855.
6. Ghorbani M, Azimi N. Note on multiple Zagreb indices. Iranian Journal of Mathematical Chemistry. 2012; 3(2): 137-143.
7. Gutman I. Geometric approach to degree-based topological indices Sombor indices. MATCH Commun. Math. Comput. Chem. 2021,86, 11-16.
8. Shirdel, G.H., RezaPour H., Sayadi. A.M.The Hyper-Zagreb Index of Graph Operations. Iranian Journal of Mathematical Chemistry, 4(2), (2013), 213-220.
9. Graovac, M. Ghorbani, M. A. Hosseinzadeh, computing fifth Geometric – Arithmetic index for nanostar dendrimers, J. Math. Nanosci. , 1, (2011)33-42.
10. V.R. Kulli. On Banhatti- Sombor indices. International Journal of Applied Chemistry, 8(1)(2021), 21-25.

****

Paper 58

Study of Chemically Deposited Nickel Sulfide Thin Films

V.B. Sanap[1*], M.S. Patil[1], A.D. Suryawanshi[2], B.H. Pawar

[1]Department of Physics, Yeshwantrao Chavan College, Sillod, Dist. Aurangabad (M.S.), India.

[2] Department of Physics, B. J. College, Ale, Dist. Pune (M.S.), India.

Abstract: Nickel Sulfide (NiS) thin films have been deposited on commercial glass substrate by a simple and inexpensive chemical bath deposition technique. The films have been prepared by various the deposition parameters such as concentration of solution, deposition time, pH of solution, temperature, etc. Nickel sulfate, thiourea and ammonia solution was used for synthesis. The structural, morphological and optical properties were characterized using X-ray diffraction (XRD), scanning electron microscopy (SEM), UV-visible spectroscopy (UV-VIS). The XRD study confirms the cubic structure of as-deposited NiS thin film with good crystallinity. The grain size obtained is in the range of 38nm to 53nm. The optical study reveals the good quality nanocrystalline films with energy band gap ranging from 1.31eV to 1.43eV. Overall study indicates the prepared NiS thin film has a good crystallinity with uniform morphology which is useful for optoelectronic applications.

Keywords: NiS, Nickel sulfide, chemical bath deposition, thin films.

1. INTRODUCTION

Nickel sulfide (NiS) is one of the most attractive materials due to its high reflection in the infrared range, electron mobility and low toxicity. It belongs to VIII–VI compound semiconductor materials. Nickel sulfide films have a number of applications in various devices such as solar selective coatings, solar cells, photoconductors, sensors, IR detectors, as an electrode in photoelectrochemical storage device etc. [1-3]

A variety of methods, including electrodeposition, SILAR [4], pulsed laser ablation [5], metal-organic chemical vapour deposition [6] thermal and photochemical chemical vapour deposition [7] can be used for the preparation of nickel sulphide thin films. Out of this chemical bath deposition technique has become more popular in recent decades, especially for thin film deposition, due to its numerous advantages. It is easy, inexpensive and convenient method for large area preparation of thin films, at close to room temperature. Also films can be deposited on different kinds, shapes and sizes of substrates [8-11].

In this study, the influence of various deposition parameters, such as deposition time, temperature, pH and concentration of solution on the properties of thin films were studied. This reported data was analyzed by using X-ray diffractometer, scanning electron microscopy and UV-Visible Spectrophotometer techniques. The obtained results are very useful for many

scientific, technological and industrial applications in the field of optoelectronic devices, especially solar cells.

2. EXPERIMENTAL DETAILS

Highest purity grade chemicals have been used for the deposition of NiS thin film. Solutions of various concentration of nickel sulfate and thiourea prepared in double distilled water is used for deposition of nickel sulfide films. The pH of solution was adjusted by adding ammonia solution slowly in it. The solution was stirred and transferred to another container containing substrate. The resulting solution was kept at 70±2ºC for different deposition time. Commercial soda lime glass slides were used as substrate for the deposition. Cleaning of substrate is important in deposition of thin films, cleaning steps and growth procedure is reported elsewhere [12-14].

The crystallographic structure of films was analyzed with a diffractometer (EXPERT-PRO) by using Cu-Kα lines (λ= 1.542Å).The average grain size in the deposited films was obtained from a Debye-Scherrer's formula. Surface morphology was examined by JEOL model JSM-6400 scanning electron microscope (SEM). Optical properties were measured at room temperature by using Perklin-Elmer UV-VIS lambda-35 spectrometer, at normal incidence of light in the wavelength range 200-1000nm.

3. RESULTS AND DISCUSSION

3.1 STRUCTURAL AND MORPHOLOGICAL PROPERTIES

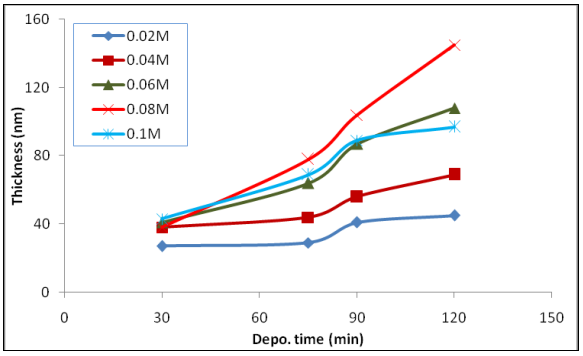

Fig. 1 *Variation of film thickness with deposition time for different concentration*.

Fig. 1 shows the variation of film thickness with deposition time for different concentration of deposition solution. It is observed that the film thickness increases with deposition time. It is observed that the film thickness increases linearly with uniform deposition and good

crystallization for the concentration 0.08M. Where as for lower concentration it is nearly saturated for higher deposition time.

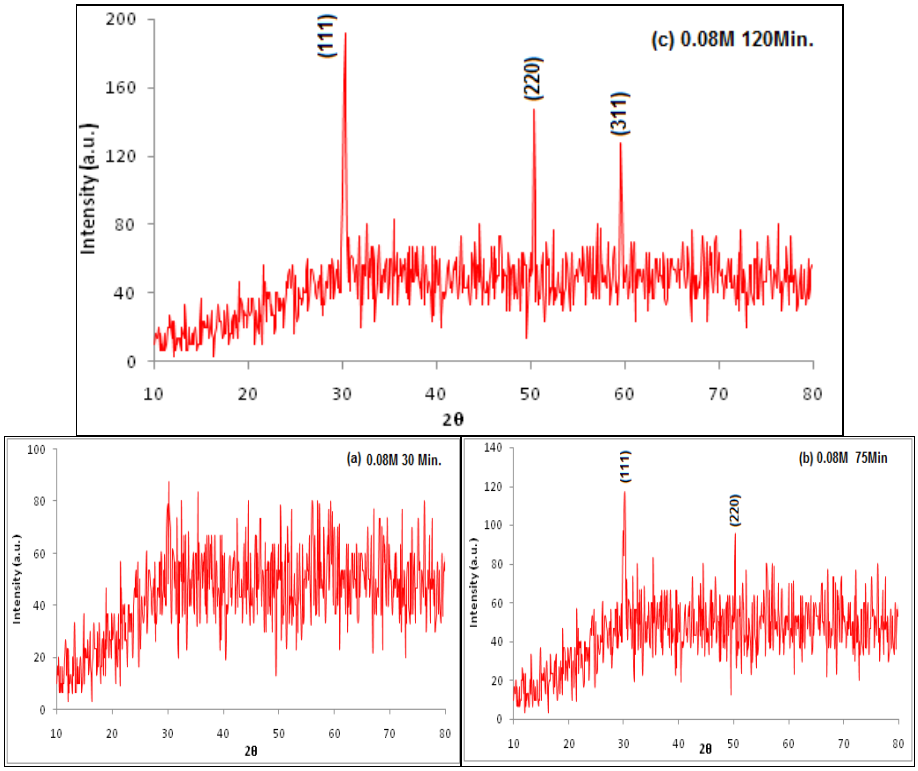

Fig. 2 *XRD pattern of nickel sulfide films for various deposition time (a) 30 Min. (b) 75 Min. (c) 120 Min.*

Fig. 2 shows the XRD pattern of nickel sulfide thin film for various deposition time. The nickel sulfide film shows dominant crystalline peaks at 2θ = 30.2°, 50.3° and 59.5° positions correspond to the (111), (220) and (311) planes for higher deposition time. A comparison of peak position with the standard data (JCPDS Reference code: 00-052-1027) confirms the cubic structure of nickel sulphide films [15].

XRD graph shows highest intensity diffraction peak along (111) plane indicating smooth surface with small grain size and high degree of homogeneity. It is also observed that the intensity of peaks increases with deposition time. Diffraction peak along (311) plane is observed for higher deposition time.

The average grain size (g) has been obtained from the XRD patterns using Debye-Scherrer's formula [13-15],

$$g = K\lambda / \beta \cos\theta$$

Where, K = constant taken to be 0.94

λ = wavelength of x-ray used (1.542Å)

β = FWHM of the peak and

θ = Bragg's angle

The morphological study shows smoother and more uniform films for 0.08M concentration. The grain size obtained is in the range of 38nm to 53nm. The grain size evaluated from SEM matches with the grain size obtained by XRD.

3.2 OPTICAL PROPERTIES

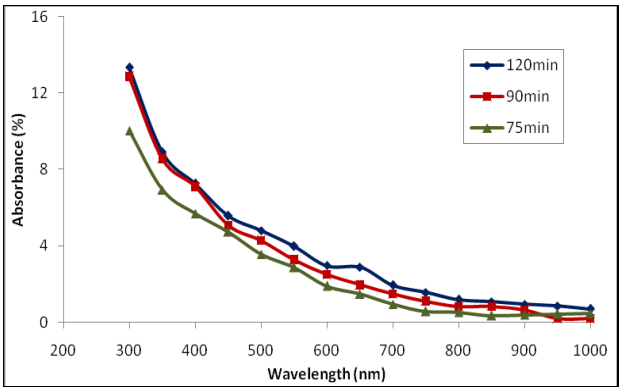

Fig. 3 *Optical absorbance of nickel sulfide thin films for different concentration.*

Fig. 3 shows the optical absorbance spectra of nickel sulfide thin film deposited for various deposition time. The as-deposited film shows gradual decrease in absorbance with the increase in wavelength of radiation. The absorbance spectra clearly indicates the higher absorbance for thicker films. This may be due to more deposition of film on the surface of substrate providing better absorption properties.

From the absorbance data, the absorption co-efficient α was calculated using Lamberts law [16-17],

$$\ln (I_0/I_t) = 2.303\ A = \alpha\ d$$

Where, I_0 and I_t are the intensity of incident and transmitted light respectively. A is absorbance and d is the film thickness.

The absorption co-efficient α was found to follow the relation, [18-19]

$$\alpha h\nu = A\ (h\nu - Eg)^{½}$$

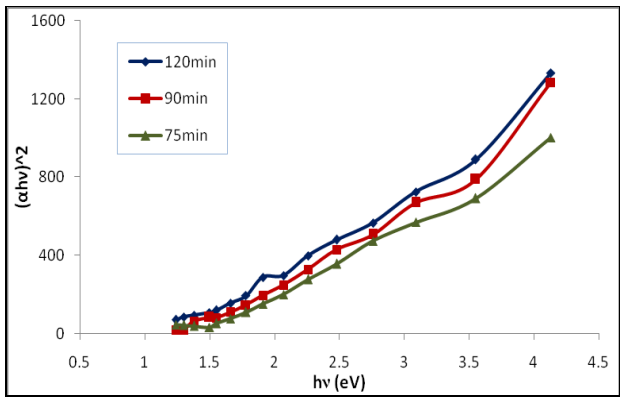

Fig. 4 *Plot of* $(\propto h\nu)^2$ *versus* $h\nu$ *for nickel sulfide thin films.*

The band gap Eg was determined from each film by plotting $(\alpha h\nu)^2$ versus $h\nu$ and then extrapolating the straight line portion to the energy axis at $\alpha = 0$. The band gap energy Eg obtained is in between 1.31eV and 1.43eV for various deposition time. (Fig. 4).

4. CONCLUSIONS

Nanostructured nickel sulfide thin films have been successfully synthesized using low cost, simple CBD technique. The XRD patterns showed the films were polycrystalline in nature with cubic structure. The influences of deposition parameters on different properties of as-deposited thin films have been noticed. The films have been characterized using optical measurements as absorbance spectra, optical band gap energy as well as thickness, structure, surface morphology. Results obtained from characterization shows obtained films are of good quality and suitable for optoelectronic applications.

ACKNOWLEDGEMENTS

The authors are grateful to Head, DME, VNIT Nagpur for providing XRD and SEM facilities. We would also like to acknowledge Head of Instrumentation Cell, SGBAMU for UV-VIS-Near IR facilities.

REFERENCES

[1] A. Gahtar et. Al. (2020) Advances in Materials Science, Vol. 20, No. 3(65).

[2] Pramanik P and Biswas S (1986) *J. Solid State Chem.* **65** 145

[3] Anuar K., Zulkarnain Z., Saravanan N., Zuriyatina A., Sharin R., (2004) Materials Science (Medziagotyra), 10, p. 157-161.

[4] Sartale S.D., Lokhande C.D. (2001) Materials Chemistry and Physics, 72, p. 101-104.

[5] Lee H.Y., Kanai M., Kawai T., Kawai S. (1993) Japan Journal of Applied Physics, 32, p. 2100-2101.
[6] Nomura R., Hayata H. (2001) Transactions of the Materials Research Society of Japan, 26, p. 1283-1286.
[7] Cheon J.W., Talaga D.S., Zink J.I. (1997) Chemistry of Materials, 9, p. 1208-1212.
[8] S.H.Pawar, C.H. Bhosale (1986) Bull. Matter Sci., Vol.**8**, No.3, 419-422.
[9] Y.A.Salazar et al. (2006) Brazilian Journal of Physics, vol.**36**, No.3B.
[10] Myeong-Hee Ko, Bonggeun Shong et.al (2018) Ceram. Int., 041.
[11] J.G.Vazquez Luna et al. (1999) Cryst. Res. Technol. Vol.**34**, No.8, 949-958.
[12] P.K.Nair, M.T.S. Nair et al (1989) J. Phys, D**22**, 829.
[13] G.Kitaev, S.Mokrushin, A. Uritskaya, (1965) Kolloidn.Z.**27**,51.
[14] I. Oladeji, I.Chow, (1997) J.Electrochem. Soc. **144**,2342.
[15] Kitakaze A., Sugaki A. (2001) Neues Jahrbuch Mineralogie Monatshefte, 41-48,
[16] M.Maleki, M. Sasani Ghamsari, sh Mirdamadi, R. Ghasemzadeh (2007) Semi-conductor Physics-Quantum Electronics and Optoelectronics **10**, 30.
[17] M.S. Sonawane, M.S. Shinde and R.S. Patil (2015) Indian Journal of Pure & Applied Physics, Vol. 53, 686-690.
[18] T.Nakanishi, K, Ito, (1994) Sol. Energy Mater. Sol.Cells **35,** 171.
[19] A.Adachi, A.Kudo and T.Sakata (1995) Bull.Chem. Soc.Jpn **68**, 3283.

Paper 59

"Biosynthesis, characterization, and antibacterial activity of silver nanoparticles from an endophytic fungus *Alanphillipsia aloeigena*"

Commented [AMD7R6]:

Sayyad Shahim K[1], Gachande B D[1] and Shaikh N F[2]

[1]Post Graduate Department of Botany, N.E.S. Science College, Nanded.

[2]Government College of Arts and Science, Aurangabad.

Abstract:-

Recently the attentions of many researchers increased towards biosynthesis of nanoparticles due to their wide applications in industries, agriculture and medicine etc. Several biosynthesized metal nanoparticles have been found to be more effective against the growth of many infectious pathogenic microorganisms. The present study emphasizes on the biosynthesis of extracellular silver nanoparticles (AgNPs) from an endophytic fungus *Alanphillipsia aloeigena* isolated and identified by using 18s rRNA ITS region from different parts of *Maytenus emarginata*(Willd.) Ding Hou. Biosynthesized AgNPs characterized for UV-Visible Spectroscopy, FTIR, TEM and XRD. UV-Visible Spectroscopy absorption shows peak at 445 nm, TEM analysis shows nanoparticles were spherical and 20-70nm in size, FTIR confirms the presence of different biomolecules and XRD confirms silver nanoparticles are crystalline in nature. Antibacterial activity of biosynthesized silver nanoparticles analysed the zone of inhibition around the wells were measured. Result revealed that biosynthesized AgNPs of *Alanphillipsia aloeigena* were effective against *Klebsiella pneumoniae, Eischerchia coli, Styphalococcus aureus, Salmonella typhi* and no zone of inhibition against *Shigella Sp.*Thus, the present study concludes with the eco-friendly & biogenic method for synthesis of AgNPs with effective antibacterial activity against clinically important human pathogens.

Keywords: - Endophyte, *Maytenus emarginata*, *A.aloeigena*, AgNPs & antibacterial.

1. Introduction:-

Myconanotechnology is an emerging field of modern science, where fungi are being exploited for the green synthesis of nanoparticles with desirable shape and size. Fungi have a more advantage over bacteria as well as actinomycetes, because fungi are excellent secretors of proteins leads to a higher yield of green nanoparticles which are highly stable, eco-friendly, cost-effective, and non-toxic.

Recently, a wide range of potential fungal species are being screened to produce different green nanoparticles, such as silver, gold, silica, selenium, platinum, zirconium, titanium, zinc oxide, copper, chitosan and magnetite reported by various researchers.

In traditional method fungi have been identified and classified on the basis of morphological and microscopic observation of different characters, later by ultra-structural and biochemical studies, which however did not always differentiate between analogies and homologies (Weber, 2009). However, the frequent absence of distinctive morphological character for identification reinforces the need for alternate DNA based identification of enormous microscopic species and socioeconomic relevance of fungi (Seifert, *et al.*, 2007). Amongst fungi, not much work has been done on mycosynthesis of green silver nanoparticles production from endophytic fungi of different plants. A very few report such as *Penicillium* spp isolated from the medicinal plant *Centella asiatica* and *Curcuma longa* (Devi, 2012; Dattu *et al.* 2013). Mycosynthesis of silver nanoparticles from endophytic fungi, *Penicillium* species of *Glycosmis mauritiana*, (Govindappa *et al.* 2016). Endophytic fungi namely, *Pencillium* sp., *Alternaria* sp., *Aspergillus* sp and *Cladosporium* sp from different parts of *Calotropis procera* (Debjani *et al.*, 2016).

In recent years the development of resistant pathogenic strains of pathogen and emergence of new disease causing agents has been increased, so that pathogenic resistance is one of the world's most emerging problems in public healthcare leads to increasing the demand for novel effective bioactive compounds in healthcare, agriculture, environment and industry. Therefore, it is necessary to develop and design a novel strategy to overcome such type of new limitations raised in different areas of society.

Since plants endophytes have been a major source of bioactive compounds for drug discovery. Plant endophytic fungi are novel and important for production of natural bioactive compounds with their potential use in medicine, agriculture and food industry. The various important bioactive compounds from endophytic fungi isolated which shows insecticidal, antimicrobial, radical scavenging, plant growth promoting, antidiabetic and anticancer activities.

Extracellular silver nanoparticles (AgNPs) of *Aspergillus flavus* shows highest zone of inhibition against *S. flexneri and P. mirabilis* at the concentration of 100µg/ml (Wilson *et al.*, 2016). Silver nanoparticles of *Fusarium oxysporum* show antibacterial activity against pathogenic bacteria (Gholami *et. al.*, 2013). Extracellular biosynthesized silver nanoparticles of Endophytic fungi *Penicillium* result revealed that the maximum zone of inhibition 21 mm and 15mm showed against *Pseudomonas aeruginosa* and *Klbesella pneumonia,*where as

Eischerchia coli showed the least zone of inhibition of 13mm at 80 µl of concentration (Dattu *et al.*, 2013).

There is very little report on endophytic fungi from *Maytenus emarginata* (Willd.) The applications of endophytic fungi for production of green nanoparticles remain untouched. There is no report on biosynthesis of endophytic fungal silver nanoparticles from *Maytenus emarginata* (Willd.) Ding Hou and its antibacterial activity, therefore present research work were carried out.

2. Materials and methods:-

Collection of plant materials:

Plant parts like stem and leaf of *Maytenus emarginata* (Willd.) were collected from different areas of Marathwada region.These plant materials were collected in sterile polythene bags and brought to the laboratoryused for theinvestigation of endophytic fungi.

Isolation of Endophytic Fungi:

Endophytic fungi were isolated by following methods employed by Selvakumar*et al.* (2014) and Hallman *et al.* (2007). The collected plant samples were washed in running tap water to remove the debris and epiphytic microorganisms and soaked in 0.1 % mercury chloride subsequently surface sterilized by using ethanol. Followed by 2% Sodium hypochlorite solution for 2-4 minutes then dipped in sterile distilled water. The Sterile segments were then chopped into 3-4 mm x 0.1 cm lengths and inoculated in Petri dishes containing Czapadox agar and potato dextrose agar (PDA) medium supplemented with streptomycin.The Petri disheswere sealed and incubated at room temperature (28±2˚C) for 15 days. Fungal growth growing out of the pieces was subcultured on separate Czapadox agar medium plates and slants before use for the identification.

Molecular Identification of Isolated fungal organisms-

The identification of endophytic fungi was done using 18s rRNA ITS universal primers at Saibiosystems Pvt. Ltd. Nagpur. The pure culture of isolated fungal strains was maintained in Czapadox agar slants at 28^0C during the study.

Biosynthesis of Silver Nanoparticles:-

For screening of biosynthesis of extracellular silver nanoparticles (AgNPs) the isolated fungi were grown in the Czapadox broth supplemented with streptomycin at 28^0C with shaking at120rpm for incubation period of 72 hrs. After incubation period biomass of fungi was harvested, filtered using Whatman filter paper number 1 and washed several times with

sterile distilled water to remove any medium component. Harvested biomass was transferred into100 ml of sterile distilled water and incubated for 48 hours. The cell-free filtrate was used in experiments. SNP was prepared by mixing AgNO3 (1 mM of final concentration) with cell-free extract. The above flask was then incubated at room temperature under dark conditions, and observed for color development. Control was also prepared, containing only the cell filtrate without silver nitrate solution.The formation of silver nanoparticle is usually confirmed by visual observation of color change from pale white to reddish brown. This appearance of color change from pale white to brown is a clear indication of the formation of silver nanoparticles by reduction of silver in the filtrate extracellularly.SNP synthesis was carried out by the method of (Prabavathy *et al.,* 2015 and Kiran, 2017).

Characterization of biosynthesized AgNPs

The preliminarily formation of AgNps was confirmed by visual observation of change in color from pale white to reddish brown, further by UV-visible spectrum analysis measuring the absorbance of solution at wavelengths between 300 and 600 nm.the size and shape of nanoparticles was done by TEM (Hitachi-H-7500). FTIR analysis was carried in the range of 500 to 4000 cm−1. (Priyom and Uma, 2017).crystallinity size and phase purity of biosynthesized AgNps were performed by X-ray diffractometerwith Philips PW 1830 X-Ray Generator operated at a voltage of 40kv and current of 30mA with cu kal radiation. (Vanmathi and Sivakumar, 2014).

Antibacterial activity of AgNPs

The antibacterial activity of biosynthesized silver nanoparticles tested using the well diffusion method against human pathogenic organisms such as *Klebsiella pneumoniae, Eischerchia coli, Styphalococcus aureus, Shigella Sp.,* and *Salmonella typhi.* Each well was loaded with different concentration of AgNps like 25, 50 and 100 µl.Streptomycin, a standard antibiotic of concentration 10 µg/ml, was used as the positive control (PC), all nutrient agar plates were incubated at 37°C for 24 hrs and 27ºC for 3 days respectively. After that analysed the zone of inhibition around the wells were measured (Devi *et al.,* 2014).

Results & Discussion:-

In present research work *Alanphillipsia aloeigena,* isolated from the stem, leaf and flower in the laboratory. Similarly various researcher isolated endophytic fungi from different plant parts of medicinal plant but there is very few report on endophytic fungi from *Maytenus emarginata* (Willd.) Ding Hou. Endophytic fungi *Xylaria* isolated by(Meenavalli *et al.,*

2013), *Phyllosticta capitalensis* isolated by (Naveen *et al.,* 2014), *Pestalotiopsis* sp. from *Maytenus ilicifolia* a medicinal plant from Brazil (Deeksha *et al.,* 2016). Correct Identification of endophytic fungal isolates on the basis of morphological characters is a major problem, because many of them are exhibit pleomorphism. Hence, we used molecular identification through ITS sequencing of 18S rRNA region universal primers gene. After molecular identification authentication were carried out by comparing the result sequence to those available in National centre for biotechnology information (NCBI) data. Endophyte *Rhizophora mucronata* identified at molecular level using the nuclear ribosomal DNA internal transcribe spacer (ITS) sequences and compared with high similarity matches to known sequences in the NCBI GenBank (Tuan *et al.,* 2018).

After addition of 1mM colorless Silver nitrate to cell free filtrate of endophytic fungus visually changes seen from colorless to brown cell free filtrate. It confirms the biosynthesis of AgNPs.Several enzymes, NADPH-dependent reductases, nitrate-dependent reductases and an extracellular shuttle quinone, were involved in silver nanoparticles (AgNP) biosynthesis for *Fusarium oxysporum* (Jain *et al.,* 2011). Protein free amine groups and cystein stabilizes the silver nanoparticles by forming a capping agent (Soni and Prakash, 2011). A number of researchers supported that nitrate reductase play significant role for extracellular biosynthesis of silver nanoparticles (Vigneshwaran, 2006).

The silver nanoparticles was subjected to determine their absorption at 0 (zero) and 24 hours. Absorption peak of λ max at a range of 415 nm to 450 nm, absorption peak noted at 445 nm for *Alanphillipsia aloeigena*. Silver nanoparticle of *A.conicus, Penicillium janthinellum* and *Phomosis was* subjected to UV-Vis spectra which was recorded at 420nm after 24, 48 and 72 and 96 hours incubation with a strong peak was observed between 400-200nm (Bharathidasan and Panneerselvam, 2012).UV-Visible Spectroscopy for spectrum confirms silver nanoparticle at the absorption range between 400 and 450 nm (Dattu *et al.,* 2014).

TEM analysis showed that the size of SNPs were between 20 and 70 nm with roughly spherical in shape. Transmission electron microscopy analysis revealed that the AgNPs were spherical in shape with 3–40 nm in size (Vasudeva*et al.*,2016). Biosynthesized AgNPs of *Penicillium brevicompactum* are spherical with 30–50 nm in size (Shahenaz*et al.*,2016). XRD analysis confirmed the crystalline nature of AgNPs. Fourier Transform Infrared Spectroscopy (FTIR) confirms the presence of different biomolecules. Biosynthesized AgNPs Fourier transform infrared analysis of *Penicillium brevicompactum* showed amides and amines that are responsible for the stabilization of AgNPs (Shahenaz*et al.*,2016). The FTIR results

suggested that both carbonyl and hydroxyl functional groups in curvularin are responsible for the reduction of the Ag + ions and stabilizing AgNPs (Sobhy*et al.*2017).

The results showed that AgNPs of *Alanphillipsia aloeigena* were effective against *Klebsiella pneumoniae, Eischerchia coli, Styphalococcus aureus,* and *Salmonella typhi*. As increase in concentration increases the zone of inhibition, at 100µl maximum zone of inhibition recorded. AgNPs at 25µl, 50µl and 100µl shows zone of inhibition 19±0.30 mm, 20±1.0 mm and 20±1.2 mm respectively against *Klebsiella pneumoniae*. 17±0.40 mm, 18±0.6 mm and 19±0.8 mm respectively against *Eischerchia coli*. 00 mm, 14±0.6 mm and 15±1.3mm respectively against *Styphalococcus aureus*. 14±0.8 mm, 14±0.4 mm and 15±0.5 mm respectively against *Salmonella typhi*. No zone of inhibition against *Shigella Sp* (Table 1 and Fig.1).The silver nanoparticles show potent antimicrobial property due to their extremely large surface area, which provides better adherence with microbes (Arias, 2009). Antibacterial activity due to penetration of AgNPs into bacterial cell which interact to components such as DNA, RNA, peptidoglycan and protein (Chaloupka*et. al.,* 2010). Similar effects on *Eischerchia coli* and *Styphalococcus aureus* pathogenic strains were observed (Jun sung *et al.,* 2007). Good antibacterial activity against *Eischerchia coli* using AgNps synthesized by *Aspergillus flavus* (Ninganagouda*et al.,* 2013).

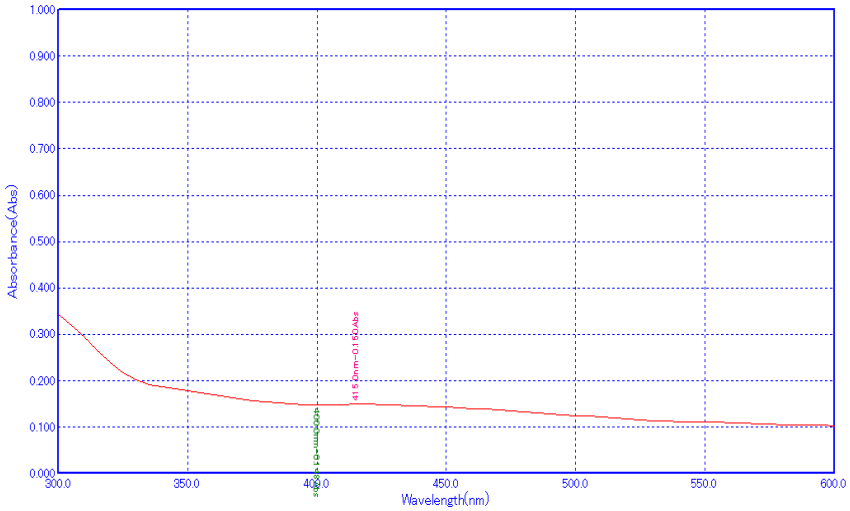

Spectra.1. UV-Visible spectrum analysis of silver nanoparticles synthesized from *Alanphillipsia aloeigena* (Zero hour spectra).

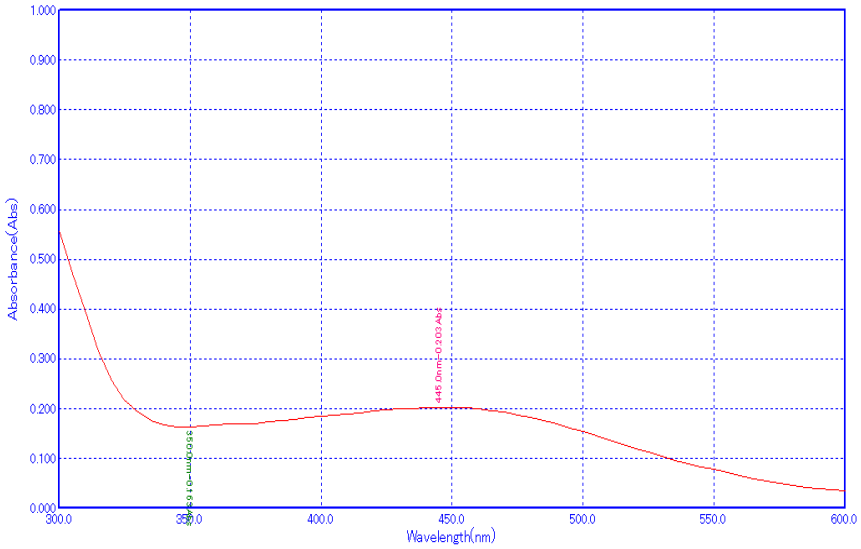

Spectra.2. UV-Visible spectrum analysis of silver nanoparticles synthesized from *Alanphillipsia aloeigena* (24 hour spectra).

Table. 1. Antibacterial activity of biosynthesized silver nanoparticles from *Alanphillipsia aloeigena* against clinical pathogenic bacteria.

Bacterial strains	AgNPs Zone of inhibition			Streptomycin
	25µl	50µl	100µl	10µl
Klebsiella pneumoniae	19±0.30	20±1.0	20±1.2	22 ± 0.6
Escherichia coli	17±0.40	18±0.6	19±0.8	22.5 ± 0.7
Styphalococcus aureus	-	14±0.6	15±1.3	23.4 ± 0.5
Shigella Sp.	-	-	-	19 ± 0.5
Salmonella typhi	14±0.8	14±0.4	15±0.5	20 ± 0.8

Fig.1. Antibacterial activity of biosynthesized silver nanoparticles from *Alanphillipsia aloeigena* against clinical pathogenic bacteria.

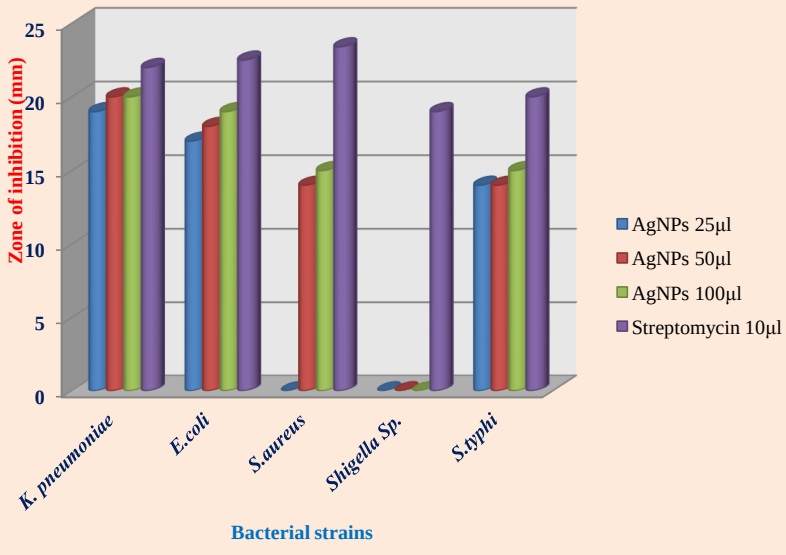

A) Plate containing pure culture of endophytic fungi

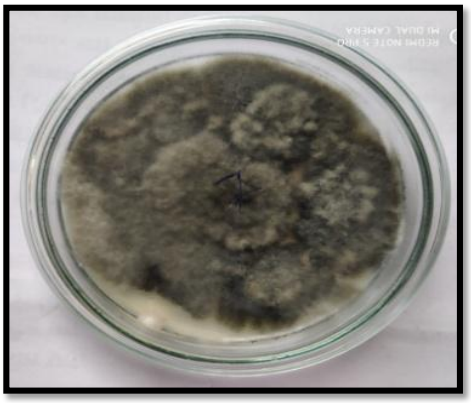

c) Fungal extracellular filtrate

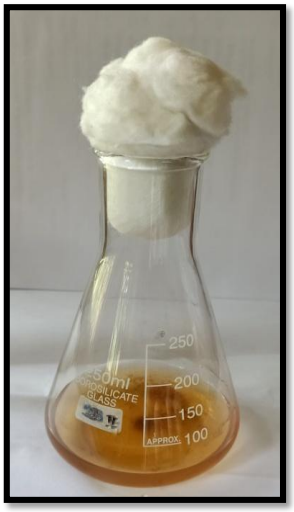

d) Filtrate with silver nitrate

Antibacterial activity of biosynthesized AgNPs on *Escherichia coli*

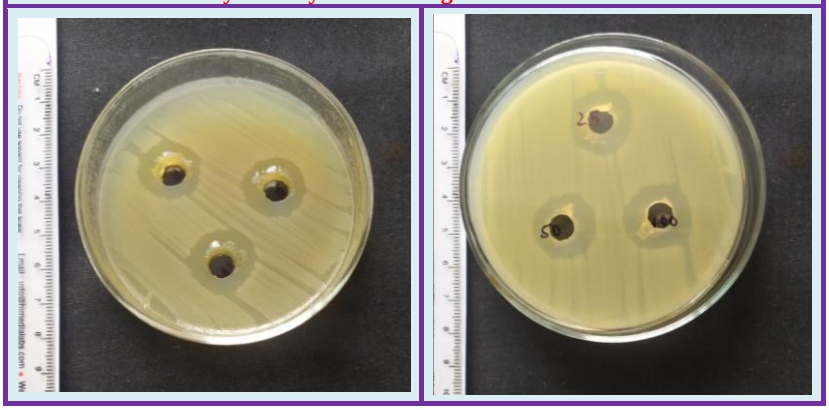

Antibacterial activity of biosynthesized AgNPs on *Shigella Sp.*

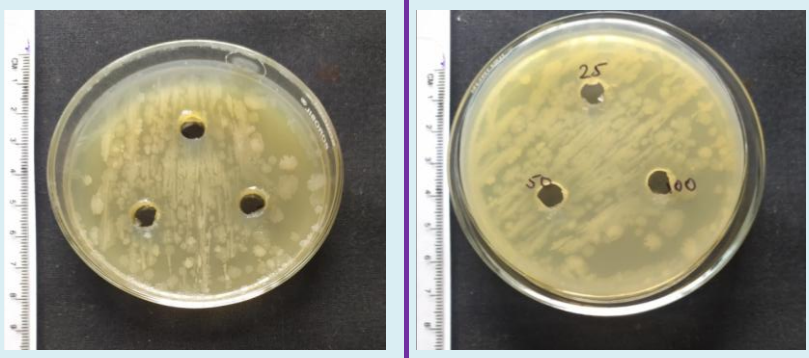

Antibacterial activity of biosynthesized AgNPs on *Styphalococcus aureus*

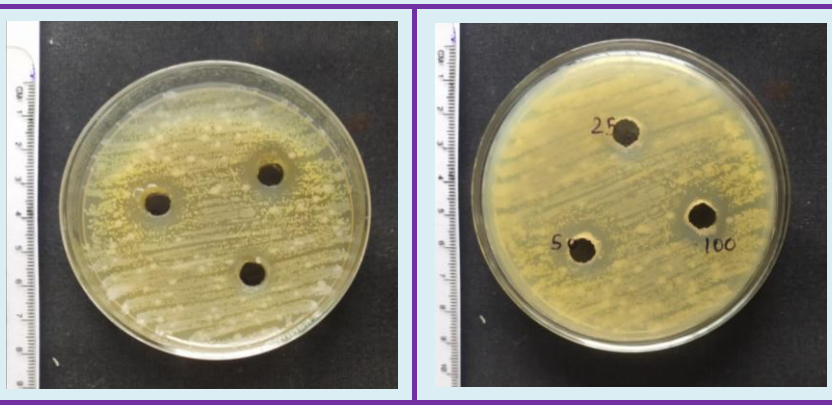

Antibacterial activity of biosynthesized AgNPs on*Salmonella typhi*

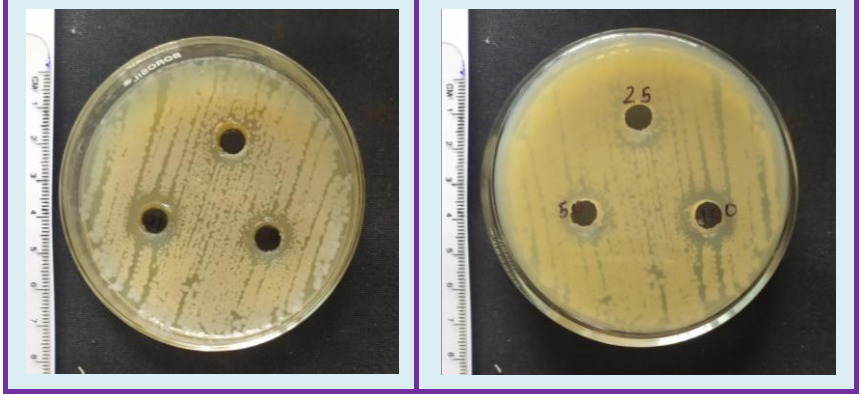

Antibacterial activity of biosynthesized AgNPs on *Klebsiella pneumoniae*

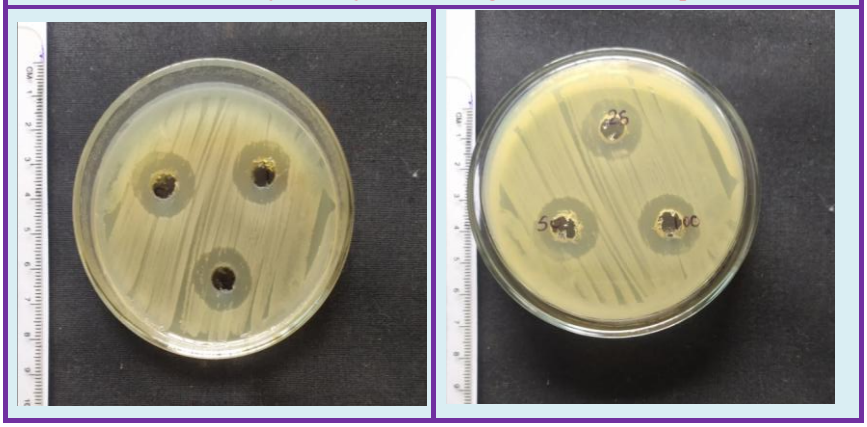

Conclusion:-

Present research finding shows the *Alanphillipsia aloeigena* endophyte of *Maytenus emarginata* (Willd.) is good producer of silver nanoparticles. Biosynthesized Extracellular silver nanoparticles show much potent antibacterial inhibition activity against different human pathogenic bacteria. It indicates great therapeutic agents in pharmaceutical and biomedical importance. The present research reports serve as a simple, cheap and ecofriendly approach of biosynthesis of silver nanoparticles

Acknowledgement:-

The acknowledgements are due to the Principal of NES Science College, Nanded for providing necessary facilities for carried out present investigation. The author Sayyad Shahim is grateful to the Maulana Azad National Fellowship, New Delhi for their financial assistanceto conduct this research work.

References:-

Bharathidasan R and Panneerselvam A (2012). Biosynthesis and Characterization of Silver Nanoparticles Using Endophytic Fungi *Aspergillus*, *Penicillium janthinellum* and *Phomosis* sp. *International Journal of Pharmaceutical Sciences and Research*,3(9):3163-3169.

Chaloupka K, Malam Y, Seifalian AM (2010). Nanosilver as a new generation of nano product in biomedical applications.*Trends Biotechnol*, 28:580–8.

Dattu Singh, Vandana Rathod, Shivraj Ninganagounda, Jyoti Herimat, Prema Kulkarni (2013). Biosyntheis of Silver Nanoparticles by Endophytic Fungi *Penicillium* sp. Isolated from *Curcuma longa* (Turmeric) and its antibacterial activity against pathogenic gram negative bacteria. *Journal of Pharmacy Research*, 7:448-453.

Debjani Roy Chowdhury., Swapan Kumar Chatterjee and Subhash Kanti Roy (2016). Studies on Endophytic Fungi of *Calotropis Procera*(L.) R.Br. with A View to Their Antimicrobial and Antioxidant Actvities Mediated by Extracellular Synthesised Silver Nanoparticles. *Journal of Pharmacy and Biological Sciences*, 11 (**5**):113-121.

Deeksha Sharma, Avijit Pramanik and Pavan Kumar Agrawal (2016). Evaluation of bioactive secondary metabolites from endophytic fungus *Pestalotiopsis neglecta* BAB-5510 isolated from leaves of *Cupressustorulosa*D.Don, *Springer*, *3 Biotech* 6:210.

Devi Nameirakpam Nirjanta, Dheeban Shankar P and Sutha S (2012). Biosynthetic Synthesis of Silver Nanoparticles from an Endophytic *Fungus* and their Antimicrobial Efficacy.*International Journal of Biochemical and Advance Research*, 3(5).

Devi SL, Donalad AB, Joshi SR (2014). Studies on biosynthesis of antimicrobial silver nanoparticles using endophytic fungi isolated from the ethno-medicinal plant *Gloriosa superb* L. *P Natl A Sci India B,* 84:1091–1099.

Gholami-Shabani M H, Azim Akbarzadeh, Mehri Mortazavi, Mohammad-Karim Emadzadeh (2013). Evaluation of The Antibacterial Properties of Silver Nanoparticles Synthesized With *Fusarium oxysporum* And *Escherichia Coli*. *International Journal of Life Sciences Biotechnology and Pharma Research*, 2(1):2250-3137.

Govindappa M, Farheen H, Chandrappa C P, Channabasava, Ravishankar V Rai and Vinay B Raghavendra (2016). Mycosynthesis of silver nanoparticles using extract of endophytic fungi, *Penicillium* species of *Glycosmis mauritiana*, and its antioxidant, antimicrobial, anti-inflammatory and tyrokinase inhibitory activity. *Advances in Natural Sciences: Nanoscience and Nanotechnology*, 7 035014.
http://dx.doi.org/10.1088/2043-6262/7/3/035014

Hallmann, J.B.G. and Schulz, B. (2007). Isolation procedures for endophytic microorganisms, Springer, Berlin Heildberg, p. 299 Khare C.P. 2004. Encyclopedia of Indian Medicinal Plants. Springer- Verlag Berlin Heidelberg, New York ISBN 3-540-20033-9:464-465.

Jain N, Bhargava A, Majumdar S, Tarafdar J and Panwar J (2011). Extracellular biosynthesis and characterization of silver nanoparticles using *Aspergillus flavus* NJP08: a mechanism perspective. *Nanoscale*, 3(2): 635-641.

Jun Sung Kim , Eunye Kuk, Kyeong Nam Yu, Jong-Ho Kim, Sung Jin Park, Hu Jang Lee, So Hyun Kim, Young Kyung Park, Yong Ho Park, Cheol-Yong Hwang, Yong-Kwon Kim, Yoon-Sik Lee, Dae Hong Jeong, Myung-Haing Cho (2007). Antimicrobial effects of silver nanoparticles. *Nanomedicine*, 3(1):95–101.

Kiran Rahul Halkai, Jayashree A. Mudda, Vasundhara Shivanna, Vandana Rathod, and Rahul S. Halkai (2017). Evaluation of antibacterial efficacy of biosynthesized silver nanoparticles derived from fungi against endo-perio pathogens *Porphyromonas gingivalis*, *Bacillus pumilus*, and *Enterococcus faecalis. Journal of Conservative Dentistry*, 20(6):398-404.

Meenavalli B. Govinda Rajulua, Nagamani Thirunavukkarasub , A. Giridhar Babuc , Ashish Aggarwalc , Trichur S. Suryanarayanana and M. Sudhakara Reddy. Endophytic Xylariaceae from the forests of Western Ghats, southern India: distribution and biological activities, *Mycology*, 2013, 4 (**1**): 29–37.

Naveen Kumar Kaushik, Thokur Sreepathy Murali, Dinkar Sahal and T. S. Suryanarayanan (2014).A search for antiplasmodial metabolites among fungal endophytes of terrestrial and marine plants of southern India, *Acta Parasitologica*, 59(**4**):745–757.

Ninganagouda, S., Rathod, V., Jyoti, H., Singh, D., Prema, K., and Manzoor-Ul-Haq (2013). Extracellular biosynthesis of silver nanoparticles using *Aspergillus flavus* and their antimicrobial activity against gram negative MDR strains.*International Journal of Pharma and Bio Sciences*, 4(2):222–229.

Prabavathy D, Niveditha R. and Vaishnavie R (2015). Antimicrobial activity of silver nanoparticles synthesized by endophytic *Aspergillus sp* isolated from *Justicia beddomei. Journal of Chemical and Pharmaceutical Research*, 7(3):784-788.

Priyom Bose and Uma Gowrie (2017). Mycosynthesis, Optimisation and Characterization of Silver Nanoparticles by Endophytic Fungus Isolated from the Root of *Casuarinajunghuhniana* Miq. *International Journal of Pharmaceutical Sciences Review and Research*, 43(1):107-115.

Seifert KA, Samson RA, Houbraken J, Levesque CA, Moncalvo JM, Louis Seize G and Hebert PD (2007). Prospects for fungus identification using CO1 DNA barcodes, with *Penicillium* as a test case. *Proceedings of the NationalAcademy of Sciences*, 104: 3901-3906.

Selvakumar, V., Panneerselvam, A., Vijayakumar, N., Mohan, A. and Thajuddin, N. (2014). Diversity of Endophytic and Rhizosphere Soil Fungi of *Avicennia marina* in Maravakadu Mangrove Forest.*IOSR Journal of Pharmacy and Biological Sciences.*9 (2):24-28.

Shahenaz Majeed, Shafiq bin Abdullah, Anima Nanda and Mohammad Tahir Ansari (2016). In vitro study of the antibacterial and anticancer activities of silver nanoparticles synthesized from *Penicillium brevicompactum* (MTCC-1999). *Journal of Taibah University for science*, 10(4):614-620.

Sobhy I. I. Abdel-Hafez , Nivien A. Nafady , Ismail R. Abdel-Rahim, Abeer M. Shaltout, Jose-Antonio Daros and Mohamed A. Mohamed (2017). Biosynthesis of Silver Nanoparticles Using the Compound Curvularin isolated from the Endophytic Fungus *Epicoccum nigrum*: Characterization and Antifungal activity. *Journal of Pharmaceutical and Applied Chemistry*, 3(2):135-146.

Soni N and Prakash S (2011). Factors affecting the geometry of silver nanoparticles synthesis in *Chrysosporium tropicum* and *Fusarium oxysporum*. *Am J Nanotechnol*, 2 (1):112-121.

Tuan Noraida Tuan Hamzah, ShiouYih Lee, Asep Hidayat, Razak Terhem, Ibrahim Faridah-Hanum and Rozi Mohamed (2018). Diversity and Characterization of Endophytic Fungi Isolated From the Tropical Mangrove Species, *Rhizophora mucronata*, and Identification of Potential Antagonists Against the Soil-Borne Fungus, *Fusarium solani*. *Frontiers in Microbiology*, 9:1707.

Vanmathi Selvi and Sivakumar T. (2014). Antihelminthic, Anticancer, Antioxidant Activity of Silver Nanoparticles isolated from *Fusarium oxysporum*. *International Journal of Current Research in Chemistry and Pharmaceutical Sciences*, 1(1):105-111.

Vasudeva Reddy Netala, Murali Satyanarayana Bethu, Bobbu Pushpalatha,Vijaya Bhaskar Baki, Sani Aishwarya, J Venkateswara Rao and Vijaya Tartte (2016). Biogenesis of silver nanoparticles using endophytic fungus *Pestalotiopsis microspora* and evaluation of their antioxidant and anticancer activities. *International Journal of Nanomedicine*, 11:5683–5696.

Vigneshwaran N, Ashtaputre NM, Varadarajan PV, Nachane RP, Paralikar KM and Balasubramanya RH (2006). Biological synthesis of silver nanoparticles using the fungus *Aspergillus flavus.Mater Lett*, 61:1413-1418.

Weber RW (2009). Recent developments in the molecular taxonomy of Fungi. In: Anke T, Weber D (Eds.) *Physiology and Genetics*. Springer, Berlin, Heidelberg.

Wilson A, Prabukumar S, Sathishkumar G, Sivaramakrishnan S (2016).*Aspergillus flavus* mediated silver nanoparticles synthesis and evaluation of its antimicrobial activity against different human pathogen. *International Journal of Applied Pharmaceutic*, 8(4):13930.

Paper 60

Dielectric studies of Glycine doped Zinc (Tris) Thiourea Sulfate Single Crystal

Commented [AMD8R7]:

Dhumane N. R.

Department of Physics, Shri Anand College, Pathardi, Ahmednagar, MS, India

Abstract:

Zinc (tris) Thiourea Sulfate (ZTS) is a promising semi-organic NLO material for second harmonic generation from metal complexes of thiourea. In present investigation Glycine was added in molar percent in saturated ZTS solution and studied effect of dopant on dielectric constant over a range from 100 Hz to 18.5 M Hz. The SHG efficiency was measured by Kurtz and Perry powder test. The Glycine doped ZTS single crystals were grown from aqueous solution by slow evaporation technique. The grown crystals were subjected to various characterization viz. FTIR studies, single crystal X-ray diffraction, UV-visible study and Dielectric constant measurement.

Keywords: Dielectric constant, Glycine, ZTS, etc.

Introduction:

Data retrieval, processing, and transmission require the search for new NLO materials with unique physical properties in this modern era of information and technology with fast and high data storage capacity. As a result, there is a high demand for the novel NLO materials. NLO material plays a major role in applications such as telecommunications, optical data storage and optical information processing [1-4]. Second order nonlinear optical materials are used in optical switching, frequency conversion and electro-optical applications especially in Electro Optical modulators [5, 6]. The NLO materials with large optical nonlinearity, low dielectric constant and wide range of transparency have great importance for high speed telecommunication, optical information processing and high optical data storage, etc. [7]. The organic NLO material have large nonlinearity compared to inorganic material but low optical transparency, poor mechanical and thermal strength and low laser damage threshold [8]. Inorganic NLO materials have large mechanical strength, thermal stability and good transmittance, but modest optical nonlinearity due to the lack of extended π-electron dislocation [9, 10]. Thus the research is focused on semi organic NLO material crystal in order to obtain superior NLO crystal by combining the

advantages of organic and inorganic materials. The semi organic materials include two systems, organic-simple structure and inorganic salts and metal-organic coordination complexes. These materials have been attracting much attention due to high nonlinearity, chemical flexibility, high mechanical and thermal stability and good transmittance [11]. Among organic NLO materials, thiourea molecule coordinates with several metal complexes to produce NLO materials. Thiourea possesses large dipole moment and it forms number of coordination compounds.

Zinc (tris) Thiourea Sulfate (ZTS) is a promising semi-organic NLO material for second harmonic generation from metal complexes of thiourea. ZTS is 1.2 times more nonlinear than KDP [12, 13]. ZTS possesses orthorhombic structure with space group $Pca2_1$ [14, 15]. Most of the amino acids individually exhibit the NLO property. Amino acids in solution at natural pH are predominantly zwitterions rather than unionized molecules. The tetrahedral array of four different groups about α-carbon atom confers optical activity on amino acid [16]. Thus, amino acid may be used as dopant in order to enhance the material properties such as nonlinear optical (NLO). The glycine is simplest and natural amino acid having just a hydrogen atom as its side chain. The pK value of the carboxyl group of glycine is 2.3 and that of amino group is 9.6 [17]. The effect of several dopant on structural and physical properties of metal complexes of thiourea have been reported [13, 18].

Experimental

Synthesis and Crystal Growth

The ZTS salt was synthesized by dissolving high purity AR grade zinc sulfate and thiourea in molar ratio 1:3 in de-ionized water. The solution was stirred by magnetic stirrer. White crystalline ZTS salt was obtained immediately. The salt was purified by repeated re-crystallization. Then the saturated solution of ZTS was prepared at room temperature in three different beakers. 1, 2 and 3 mole% of glycine was added in these beakers respectively. The obtained salt was tested for SHG by Kurtz and Perry powder test. We observed higher enhancement of SHG efficiency for 1 mole% Glycine doped ZTS as compared to pure ZTS and other doping concentrations. Thus, 1 mole% Glycine doped ZTS single crystal was grown. The growth of Glycine doped ZTS crystals was carried out by slow evaporation in constant temperature bath with an accuracy ±0.01°C. The photograph of 1 mole% Glycine doped ZTS single crystals is shown in Fig. 1.

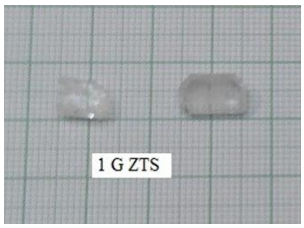

Fig. 1. Photograph of 1 mole% Glycine doped ZTS crystal

Result and Discussion

1. SHG Measurement

The initial testing of materials for second harmonic generation is tested by classical Kurtz and Perry powder SHG test [19]. The fundamental beam of 1064 nm from Q switched Nd: YAG laser was used to test the Second Harmonic Generation (SHG) property of 1, 2 and 3mole% Glycine doped ZTS and ZTS. Pulse energy 4.5 mJ/pulse and pulse width 8ns and repetition rate 10 Hz was used. The photo multiplier tube (Hamahatsu R2059) was used as detector and 90 degree geometry was employed. The SHG signal generated in the sample was confirmed from emission of green radiation from the sample. The optical signal was converted into electrical signal by means of photomultiplier tube, the output measured for pure ZTS and 1, 2, 3mole% Glycine doped ZTS were measured. It is confirmed that SHG conversion efficiency of 1mole% Glycine doped ZTS is greater than pure ZTS and other molar concentrations of Glycine in ZTS. The measured SHG of 1mole% Glycine doped ZTS is **4** times that of pure ZTS. This increase in SHG of ZTS with addition of glycine is due to the fact that the glycine has zwitter ion i.e. NH_3^+ and COO^- group. The glycine has more dipole moment because of the presence of polar amino group [2]. ZTS reacts with glycine, optically active amino group may get added in the structure and increases its non-Centro symmetry and hence increasing its SHG efficiency.

2. Single crystal X-ray Diffraction

To determine lattice cell parameter, Single crystal X-ray diffraction analysis of grown crystal was carried by Brukers axs (Kappa Apex) diffractometer. The collected data of lattice cell parameters are a = 11.17 Å, b = 7.78 Å, c = 15.50 Å and cell volume = 1346.99 Å3 and $\alpha = \beta = \gamma = 90^{\circ}$. The crystal belongs to orthorhombic system with space group Pca21. There is slight increase in unit cell volume. This increase in volume may be due to the change in pH of the solution due to addition of glycine.

3. Fourier Transform Infrared Spectroscopy (FTIR) Analysis

The FTIR spectroscopy studies were used to analyze qualitatively the presence of functional groups in synthesized compound. The FTIR analysis was carried out by Perkin Elmer Spectrum FTIR spectrometer by KBr pallet technique in the range 400-4000cm^{-1}. Fig. 2 and Fig. 3 shows FTIR spectra for pure ZTS and 1 mole% Glycine doped ZTS respectively. Comparison of IR spectra of ZTS and 1mole% Glycine doped ZTS shows slight shift in absorption bands. This shift in absorption bands may be due to addition of Glycine in ZTS. The high frequency absorption bands in region 3100-3400 cm-1 in spectrum of thiourea were not shifted to lower frequencies on formation of metal thiourea complex indicating that nitrogen to zinc bands are absent and bonding must be between sulfur and zinc. In FTIR spectra of 1mole% Glycine doped ZTS broad envelop lying in between 2750 to 3500 cm^{-1} shows symmetric and asymmetric modes of NH_2 group of zinc coordinated thiourea. The absorption band at 1624 cm^{-1} in the spectra of 1mole% Glycine doped ZTS corresponds to NH_2 bending vibrations. The absorption observed at 1512 cm^{-1} corresponds to that of N-C-N stretching vibration. The absorption band at 1400 cm^{-1} assigned to the C═S asymmetric stretching vibration. The presence of sulfate ion in the coordination sphere is evident from peaks at about 500 and 1000 cm^{-1}.

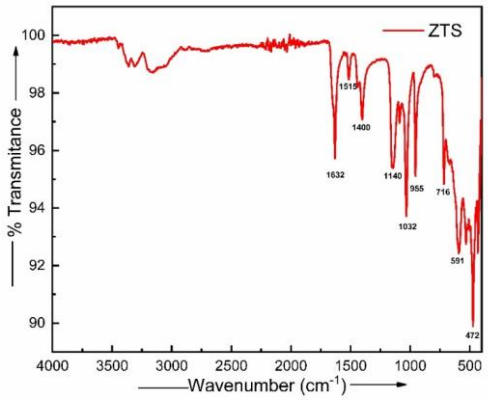

Fig. 2. FT-IR spectra of pure ZTS

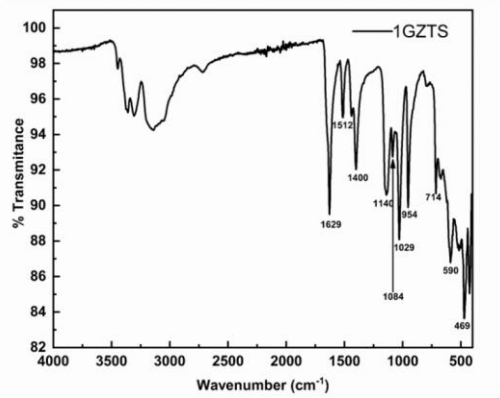

Fig. 3. FT-IR spectra of 1 mole% Glycine doped ZTS

4. UV-visible Study

The UV-visible studies of grown crystal was carried out by Shimadzu UV 1600 UV-vis. spectrometer in a range 200 nm to 1100 nm. The absorption spectra of 1mole% Glycine doped ZTS is shown in Fig. 4. The window shown in Fig. 4 shows UV spectra of pure ZTS for comparison. The absorption spectra reveal that the crystal has lower cutoff wavelength at around 290 nm. From spectra it has also been observed that the lower cutoff wavelength is almost the same for Glycine added ZTS and pure ZTS crystals. The doping of amino acid does not affect the transparency of the grown crystal. The absorption near UV region is associated with electron transition within thiourea units of ZTS. The wide range of the transparency in the entire visible region shows that this material is a potential candidate for optoelectronic applications.

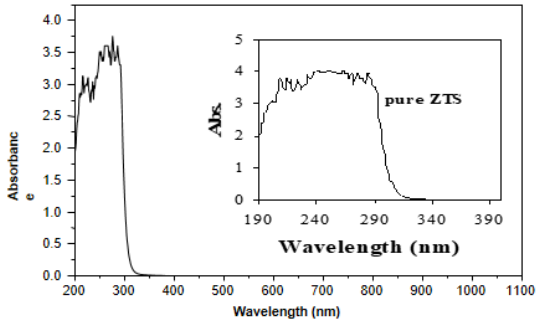

Fig. 4. UV-visible absorption spectra of 1mol% Glycine doped ZTS

5. Dielectric Study

The dielectric behavior of the doped and pure ZTS crystal were carried at room temperature using the PSM 1735 (Newtons 4th Ltd. UK) from 100Hz to 18.5 MHz frequency. The dielectric constant is calculated using the relation, $\varepsilon = Cd/\varepsilon_0 A$ where, C is the capacitance, d is the thickness; A is the area of the sample. The frequency response of dielectric constant for pure and doped ZTS crystal is shown in Fig. 5. The dielectric constant has high values in the lower frequency region and decreases with increase in frequency. The high value of dielectric constant at lower frequencies may be due to the presence of polarizations mechanism namely space charge, orientation, electronic and ionic polarization. The low values of dielectric constant at high frequencies indicate high crystal perfection and low space charge polarization. The lower dielectric constant indicate the grown crystal is efficient for NLO, optoelectronic, laser and SHG device applications.

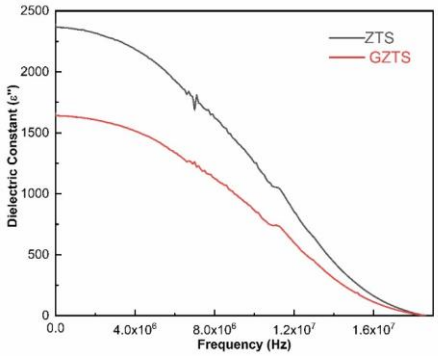

Fig. 5. Dielectric constant Vs. Frequency

Conclusion

Optical quality single crystal of Glycine doped ZTS was grown by slow evaporation technique. The Kurtz and Perry powder SHG test shows that 1mole% Glycine doped ZTS has SHG efficiency **4** times that of pure ZTS. Single crystal X-ray diffraction confirms that there is no change in basic structure of ZTS. The comparison FTIR spectra confirmed the incorporation of glycine in the material of grown crystal. The optical study shows that the Glycine doped crystal has wide optical window with lower cut off wavelength around 290 nm. The decreased dielectric constant of doped ZTS crystal revealed low polarization mechanism and high crystal purity. The

optical and dielectric study of Glycine doped crystal potential candidate for UV tunable lasers, high speed optical communication and optoelectronics device fabrication.

References:

1. K Meera, R Muralidharan, R Dhanasekaran, Prapun Manyum, P Ramasamy. "Growth of nonlinear optical material: L-arginine hydrochloride and its characterization", J Cryst Growth 263 (2004) 510.
2. R Mohan Kumar, D RajanBabu, D Jayaraman, R Jayaval, K Kitmura. "Studies on the growth aspects of semi-organic L-alanine acetate: a promising NLO crystal", J Cryst Growth 275 (2005) e1935.
3. A Pricilla Jeyakumari, J Ramajothi, S Dhanuskodi. "Structural and microhardness studies of a NLO material – bisthiourea cadmium chloride", J Cryst Growth 269 (2004) 558.
4. A S Haga Hameed, C W Lan. "Nucleation, growth and characterization of L-tartaric acid – nocotinamide NLO crystals", J Cryst Growth 270 (2004) 475.
5. K Selvaraju, R Valluvan, K Kirubavathi, S Kumararaman. "L-Cystine hydrochloride: A novel semi-organic nonlinear optical material for optical devices", Opt Commu **269** (2007) 230.
6. Shaokang Gao Weijun Chen, Guimei Wang, Jianzhong Chen. "Synthesis, crystal growth and characterization of organic NLO material: N-(4-nitrophenyl)-N-methyl-2-aminoacetonitrile (NPAN)", J Cryst Growth **297** (2006) 361.

7. Mohd Shkir, Haider Abbas, Spectrochimica Acta Part A: Molecular and Biomolecular Spectroscopy 118 (2014) 172.
8. Min-hua Jiang and Qi Fang. “Organic and Semiorganic Nonlinear Optical Materials”, Adv Mater **11** (1999) 1147.
9. H Q Sun, D R Yuan, X Q Wang, X F Cheng, C R Gong, M Zhou, H Y Xu, X C Wei, C N Luan, D Y Pan, Z F Li and X Z Shi. “A novel metal-organic coordination complex: tri-allylthiourea zinc chloride (ATZC)”, Cryst Res Technol **40** (2005) 882.
10. J Ramajothi, S Dhanuskodi, K Nagarajan. “Crystal growth, thermal, optical and microhardness studies of tris (thiourea) zinc sulfate – a semiorganic NLO material”, Cryst Res Technol **39** (2004) 414.
11. Min-hua Jiang and Qi Fang. “Organic and Semiorganic Nonlinear Optical Materials”, Adv Mater **11** (1999) 1147.
12. P M Ushasree, R Jayaval, C Subramanian, P Ramasamy. “Growth of zinc thiourea sulfate (ZTS) single crystals: a potential semiorganic NLO material”, J Cryst Growth **197** (1999) 216.
13. P M Ushasree, R Jayaval, P Ramasamy. “Growth and characterization of phosphate mixed ZTS single crystals”, Mater Sci Eng **B 65** (1999) 153.
14. P M Ushasree, R Jayaval, P Ramasamy. “Influence of pH on the characteristics of zinc tris (thiourea) sulfate (ZTS) single crystals”, Mater Chem Phys **61** (2006) 270.
15. G E Arunmozhi, de M Gomes, S Ganesamoorthy. “Growth kinetics of zinc (tris) thiourea sulphate (STZ) crystals”, Cryst Res Technol **39** (2004) 408.
16. Lubert Stryer, “Biochemistry” W. H. Freeman and Company, New York (1995) Forth Edition.
17. R Sankar, C M Ragahvan, R Mohan Kumar, R Jayavel. “Growth and characterization of bis-glycine sodium nitrate (BGSN), a novel semi-organic nonlinear optical crystal”, J Cryst Growth **309** (2007) 30.
18. S Selvakumar, J Packiam Julius, S A Rajasekar, A Ramanand and P Sagayaraj. “Microhardness, FTIR and transmission spectral studies of Mg2+ and Zn2+ doped nonlinear optical BTCC single crystals”, Mater Chem Phys **89** (2005) 244.
19. S K Kurtz and T T Perry. “A powder technique for the evaluation of nonlinear optical materials”, J ApplPhys**39** (1968) 3798.